Two-Dimensional Vortices and Accretion Disks

CIP-GEGEVENS KONINKLIJKE BIBLIOTHEEK, DEN HAAG

Nauta, Michiel Doede

Two-dimensional vortices and accretion disks / Michiel Doede Nauta.
Utrecht : Universiteit Utrecht, Faculteit Natuur- en Sterrenkunde
Proefschrift Universiteit Utrecht, - Met lit. opg. - Met samenvatting
in het Nederlands.
ISBN 90-393-2300-3
Trefw.: geofysische stromingsleer / astrofysica.

Front cover illustration: part of the surface density and potential vorticity of one of the simulations of chapter 5.

Two-Dimensional Vortices and Accretion Disks

Twee-dimensionale wervels en accretieschijven
(met een samenvatting in het Nederlands)

PROEFSCHRIFT

ter verkrijging van de graad van doctor aan de
Universiteit Utrecht op gezag van de Rector Magnificus,
Prof. Dr. H.O. Voorma, ingevolge het besluit van het
College voor Promoties in het openbaar te verdedigen
op maandag 10 januari 2000 des middags te 2.30 uur

DOOR

Michiel Doede Nauta

geboren op 19 maart 1970, te Woudenberg

Promotoren: Prof. Dr. J. Kuijpers
Faculteit der Natuurwetenschappen, Wiskunde
en Informatica, Katholieke Universiteit Nijmegen
Prof. Dr. J.T.F. Zimmerman
Faculteit Natuur- en Sterrenkunde,
Universiteit Utrecht

Contents

Chapter 1

Introduction

1.1 Introduction

This thesis deals with fluid dynamical aspects of accretion disks. Disks appeared on the astronomical stage with the discovery of the ring system of Saturn by Galileo in 1610 and Huygens in 1659 which was one of the earliest discoveries made by telescope. Saturn's disk is different from the kind discussed in this thesis, in that it consists of particles (dust/ice) interacting gravitationally and by collisions. These disks lacking a real gas pressure (to which also disk galaxies belong) are not discussed in this thesis, although vortices do also occur in them (e.g. Fridman and Khoruzhii, 1999). The first disk in which gas pressure plays a role was brought to light by Kant and Laplace in the second half of the 18th century and is what we now call the protoplanetary or protostellar disk. Their contention, that our solar system formed out of a disk, is nowadays confirmed by many observations (e.g. Chandler and Richer, 1999). Since the invention of photographic film and later CCD cameras and space borne X-ray detectors, disks have also been discovered in double star systems and in active galactic nuclei (AGN). The presence of a disk is easiest to sketch for disks in binaries, see Fig. 1.1.

In a binary system one of the stars (the secondary) swells up in the course of its evolution, fills its Roche lobe (largest effective gravitational equipotential surface surrounding a single star) and transfers matter to the accompanying star. This primary star is often a compact object (white dwarf, neutron star or black hole) so that it is deep within its Roche lobe. Since the material that flows from the secondary to the primary has angular momentum with respect to the primary, it doesn't flow in radially but forms a ring around the primary that is centrifugally supported. Under viscous processes this ring spreads and forms a disk. The disk is fed from the outside by the secondary while it looses matter on the inside to the primary: it accretes. Mass transfer from the secondary can continue if the evolutionary driven increase in radius of the secondary is fast enough or if the binary looses angular momentum so that the separation between the stars and thus the Roche lobes decrease.

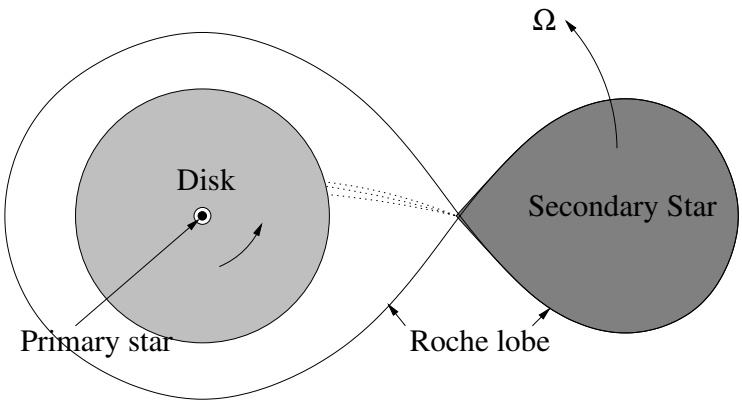

Figure 1.1: A schematic picture of an accretion disk in a binary.

In case of a protostellar disk, where there is no secondary to provide the mass, the disk forms out of the rotating molecular cloud that also gave birth to the star. Disk and star can now be of comparable mass so that self-gravity of disk material can be important, a situation not found in binary disks. In AGN the gas is supplied to a disk around a massive black hole by tidal disruption of stars, stellar collisions or gas star interactions.

In all cases the disk is made up of gas or plasma. Estimates of the characteristic mean free path indicate that a fluid or magnetohydrodynamic (MHD) description is applicable and a Boltzmann (kinetic) description is rarely needed (Frank *et al.*, 1992).

1.2 Observations

1.2.1 Evidence for accretion disks

For a long time observational evidence for the existence of accretion disks was infallible but indirect as the spatial resolution of the telescopes was too low to actually observe them. Since a couple of years protostellar disks can be seen directly (e.g. Chandler and Richer, 1999). These sources are not too distant and their disks are huge compared with accretion disks in binaries. Still, observing fine structure within the disk is beyond present day capabilities.

The strongest evidence for disks in binaries is from double peaked emission line profiles which can be explained by Doppler shifts from parts of the accretion disk moving towards and away from the observer. Based on these Doppler shifted line profiles, tomographic techniques were developed (Marsh and Horne, 1988). A recent success along this line is the detection of spiral shaped structure in a disk (Steeghs *et al.*, 1997). The disadvantage of this technique is that the formation of emission lines is not well understood and it gives no information on the overall energetics. In case the spatial orientation of the system is such that the primary star and the disk

are occulted by the secondary star, eclipse mapping methods (Horne, 1985) allow, for example, the verification of the predicted temperature dependence on radius in some systems ($T \propto r^{-3/4}$ because the viscously produced heat is locally radiated away as black body radiation) (e.g. Rutten *et al.*, 1992). (Not all systems obey this law which is perhaps attributable to occultation of the primary star and inner parts of the disk by the disk edge.)

The evidence for disks in AGN is also of spectral (maser lines (Miyoshi *et al.*, 1995) for example) and spatial origin.

1.2.2 Typical parameters of disks

With the existence of accretion disks established, the next question is what do we know about their typical parameters? The numbers quoted here come from recent reviews as Lin and Papaloizou (1996) and Sellwood and Goodman (1999) and are rough order of magnitude estimates, just to get a feeling for the different systems.

Closest by are the protostellar disks at tens of parsecs. Many of their parameter values are comparable to those of our own solar system such as the typical size (100 AU), the mass of the central star (1 $M_\odot$) and the Keplerian speed ($v_{\rm kep} = \sqrt{GM/R}$ =tens km/s). The observed temperatures are of order 100 K which makes it possible to estimate the thickness of the disk. In a thin disk the gas is supported in the radial direction by the centrifugal force and in the vertical direction by gas pressure so that hydrostatic equilibrium is assumed:

$$0 = -\frac{1}{\rho}\frac{\partial P}{\partial z} - \frac{GMz}{(R^2+z^2)^{3/2}}, \tag{1.1}$$

where ρ is density, P pressure, z is distance in the direction perpendicular to the disk plane, G the gravitational constant, M the mass of the central star and R the radial distance from the central star. Since the disk is thin, an order of magnitude estimate of this equation is:

$$\frac{c_{\rm s_{iso}}^2}{H} = \frac{GMH}{R^3},$$

in which H is the pressure scale height and $c_{\rm s}$ the (isothermal) speed of sound (determined by the temperature). It follows that:

$$H/R = c_{\rm s_{iso}}/v_{\rm kep}, \tag{1.2}$$

which is of order 0.1 for a protostellar disk. The mass in the disk varies in time. Initially it is comparable to that of the central star and at the end of the accretion process it is negligible, as in our solar system. The accretion rate in quiescence is some 10^{-8} $M_\odot$ per year but can be much higher (10^{-4} $M_\odot$/yr) during outbursts.

Further away at hundreds of parsecs are the disks in binaries. Cataclysmic Variables (CVs: binaries with a white dwarf as the primary) are taken as the standard here because most is known about these kind of disks. The size of the disk is a fair

fraction of the Roche lobe (a bit less than 1 $R_\odot$) while the mass of the central star is of the order 1 $M_\odot$ giving Kepler speeds of thousands km/s. The mass in the disk is negligible compared to that of the central star. Observed temperatures are typically 10 000 K giving a height to radius ratio of 0.02. Disks in X-ray binaries could be a factor 10 thicker (Verbunt, 1999). The accretion rate is of order 10^{-8} $M_\odot$ per year or a factor 100 lower in dwarf novae in quiescence.

At the largest distances are AGN (cosmological distance). The observed disk size is tens of parsec, while at the center there is a massive black hole (up to a few 10^9 $M_\odot$). Keplerian speeds run from hundreds km/s at the outside to thousands km/s at the inside. With a temperature of 10^4 K the ratio height over radius becomes 10^{-2}. The accretion rate is of order 1 $M_\odot$ per year.

What is apparent in all cases is that the Keplerian velocity is highly supersonic and this translates together with hydrostatic equilibrium into thin disk geometries (except at the inner most parts of the disks where different physical processes play a role). Another notable feature is the high accretion rate. Angular momentum loss is necessary for matter to spiral inward from the outer edge of the disk towards the central compact object. Angular momentum should therefore be transported from the inside to the outer edge of the disk (or be lost in a wind or jet emanating from the disk). Here it can be converted into orbital angular momentum in a binary. Ordinary viscosity does transport angular momentum but it is much too small to explain the accretion rate. Reynolds numbers based on molecular viscosity are typically of order 10^{14} or larger (Frank *et al.*, 1992). This constitutes the transport problem in accretion disks: which physical mechanism explains the observed accretion rates?

1.3 Theories

The high molecular Reynolds number suggests that the flow might be turbulent. Turbulence is known to be able to increase transport properties of fluids enormously. While molecular transport is determined by the mean free path and velocity of the particles, these quantities are commonly replaced by the dimensions of the largest eddies and speeds within these eddies in turbulent transport. The resulting effective viscosity (ν_t) is much higher and is usually parameterized by (Shakura and Sunyaev, 1973):

$$\nu_t = \alpha c_s H, \tag{1.3}$$

where α is the non-dimensional viscosity and varies from 10^{-3} in protostellar disks to 1 in CVs during outburst.

This parameterization together with an equation of state, an opacity law and the conservation equations of mass, momentum and energy constitute a closed set of equations if simplifying assumptions are made. If the disk is steady, thin, axisymmetric, non-magnetic and non-self-gravitating then a solution can be constructed as was shown by Shakura and Sunyaev (1973). This is the famous α-disk model which is the standard model for observations and theory. It predicts, among others, the following relations in the outer regions of the disk dominated by gas pressure (equation

of state) and free-free absorption (opacity):

$$T \propto \alpha^{1/5}\dot{M}^{3/10}M^{1/4}R^{-3/4},$$
$$\Sigma \propto \alpha^{-4/5}\dot{M}^{7/10}M^{1/4}R^{-3/4},$$

where Σ is the surface density (the height integrated density) and $\dot{M}$ the accretion rate. The α-parameterization is not only used for steady states but also in time dependent calculations and it is at the basis of most work done on accretion disks. This is perhaps the more surprising as the physical justification of Eq. (1.3) is weak. The argument that the flow is likely to be turbulent because the Reynolds number is high is based on laboratory experiments with Couette and Poisseuille flow. Here an instability, linear or nonlinear, drives the turbulence. However, this argument by itself cuts no ice as for example shear flow experiments in a stratified fluid show. Just adding the extra physics of buoyancy can stabilize a flow regardless of the Reynolds number as long as the Richardson number (Ri$= -(g/\rho)(d\rho/dz)/(dU/dz)^2$) is smaller than one quarter. For an accretion disk it is very well possible that the extra physics that makes it distinct from plane Couette flow quenches any nonlinear instabilities. Three-dimensional numerical experiments indeed indicate that this happens (Balbus *et al.*, 1996) and the extra physics appears to be the Coriolis force which gives rise to epicyclic (inertial) oscillations. These authors also construct kinetic energy equations for the components of the velocity fluctuations from which it was concluded that outward transport of angular momentum is accompanied by a decrease in azimuthal kinetic energy fluctuations: the mean flow does not feed the angular momentum fluctuations. (Inward transport is not an option because now the total kinetic energy of the fluctuations dies out.) The door is still ajar for hydrodynamic instabilities in that pressure fluctuations might perhaps circumvent the above mentioned problems. So still not everybody is convinced of the hydrodynamic stability of accretion disks (e.g. Lovelace *et al.*, 1999).

However, since several years it is known that inclusion of a magnetic field does lead to linear instability (Balbus and Hawley, 1991) and makes the disk turbulent. The physical reason for the instability is that a radial perturbation of the frozen-in magnetic field forces the outer fluid parcels to rotate too fast and the inner parcels too slow for gravito-centrifugal equilibrium. As a result the outer parcels move further outward and the inner further inward. Angular momentum is transfered from the inner to the outer parcels by the magnetic field. Not only does this drive turbulence but the turbulence strengthens the magnetic field by dynamo action (e.g. Brandenburg *et al.*, 1995). So even if there is initially only a small seed field present, this mechanism works because it generates its own magnetic field. It should be emphasized that even though the fluid is turbulent, transport is mainly determined by the magnetic stress, see e.g. Geertsema and Achterberg (1992). The Poynting flux is the main effect, aerodynamic friction between magnetic flux tubes and the Keplerian flow can only contribute a small amount to the viscosity (Schramkowski and Torkelsson, 1996). The observed range of α values can be explained with this (10^{-3} to 1) and it is by far the most popular explanation for the efficient transport in accretion disks. Another possibility is that the magnetic field is not embedded in the disk

but forms coronal loops which can transport angular momentum efficiently (Burm and Kuperus, 1988; Kuijpers, 1995). The weak points of these theories are that the degree of ionization should be large enough and that the Ohmic resistivity should be low enough to couple the magnetic field to the gas which is not always the case in protostellar disks.

A purely hydrodynamic explanation that is still viable and recently got some observational support (Steeghs *et al.*, 1997) is that of spiral shaped density waves and shocks. A likely source of waves is the non-axisymmetric perturbation in the gravitational field owing to the secondary star. This can severely distort the gas in the disk, especially at those radii where the orbital frequency is a multiple of the oscillation frequency of the perturbation (Lindblad resonance). This excites a compressible wave that travels inward toward the compact object. The wave develops a trailing spiral shape because of the differential Keplerian rotation. Matter moves faster than the wave so that the wave contains (pseudo) negative angular momentum. While propagating inward, wave action is conserved. This increases the amplitude of the wave and turns it into a discontinuity: a shock. The dissipation in the shock leads effectively to transport of angular momentum outward which goes into orbital angular momentum of the binary. The transport coefficients of this process are small ($\alpha \approx 10^{-3}$) because if the disk is to stay thin, the shocks have to be weak (Spruit, 1987). At the outer edge of the disk there can also be a gravitational torque due to the secondary star on the density enhancement behind the shock. This mechanism of angular momentum transport is based on a height integrated (so two-dimensional (2D)) description and was verified by several numerical simulations (Sawada *et al.*, 1986; Różyczka and Spruit, 1993). If the disk is thermally stratified in the vertical direction, then radial propagation of the waves can be inefficient because they can get deflected in the vertical direction (Lin *et al.*, 1990). Also, if the disk is cool so that Keplerian velocities are highly supersonic, the excitation of waves is inefficient (Savonije *et al.*, 1994). Viscosity has the tendency to prevent waves from reaching far into the disk and in that way also limits the efficiency. All this implies that spiral shocks are mainly of interest in protostellar disks.

Convection has been another hydrodynamic candidate for driving turbulence and transport. However, a linear analysis of convection in a local Cartesian approximation of the disk (shearing sheet) showed that angular momentum is transported inward instead of outward (Ryu and Goodman, 1992). The suggested physical reason was that at the location of interaction of two convective rolls, the outer roll has higher angular momentum and angular speed than the inner roll, thus transferring angular momentum inward. This conclusion, based on a linear analysis, was later corroborated by nonlinear 3D hydrodynamical simulations again in the shearing box approximation (Stone and Balbus, 1996).

Other mechanisms that could be relevant, notably for protostellar disks, but outside the scope of the physics discussed in this thesis, are angular momentum loss by a wind emanating from the surface of the disk and self-gravity of disk material. Recent reviews on accretion disk theory are Papaloizou and Lin (1995) and Balbus and Hawley (1998).

1.4 Planetary fluid dynamics

An accretion disk is not unique in that the transport processes might be hard to understand. Transport in other fluid dynamical systems (not necessarily in terms of angular momentum) can also be complicated. One such a system which shares some characteristics with an accretion disk is the earth's atmosphere (and oceans). Both systems are thin, almost two-dimensional and rotating. The basic driving force behind transport in the atmosphere is the latitudinal dependence of solar irradiation: the tropics are heated more than the poles. Part of this heat is locally radiated away (to space) but another part is transported by the atmosphere (and oceans) to the poles were it is lost to space as radiation. If the earth were non-rotating, this transport would probably take the form of huge Hadley cells: air rising at the equator, moving at large height towards the poles where it would descend to the earth's surface and flow back to the equator. Earth's rotation makes the process much more complicated as, for example, weather maps show. Jet streams and vortices develop and they interact giving the atmosphere a very chaotic appearance. Similar turbulent behavior is observed in the oceans that also provide for part of the (heat) transport.

This form of turbulence, flow intertwined with large scale, long-lived structures, is thought to be similar to two-dimensional turbulence but modified by rotation and a spherical surface. Usually in studies of 2D-turbulence, the velocity field is strictly two-dimensional and incompressible and an easy way to investigate it is by numerical simulations (e.g. McWilliams, 1984). 2D-turbulence is characterized by an inverse energy cascade: energy piles up at the smallest wave numbers. In physical space this manifests itself as the formation of persistent vortices that grow out of small-scale random fluctuations. These vortices interact with each other and vortices of like sign can merge. In the end only two vortices of opposite sign are left. On the earth's surface the inverse cascade can not proceed that far. There are waves present on the longest length scales that transport energy to small (latitudinal) scales. These waves own their presence to the curvature of the earth's surface which makes the local vertical rotation vector and thus the Coriolis acceleration dependent on latitude and they are called Rossby waves. Because of the anisotropic nature of these waves the inverse cascade is halted in the latitudinal direction but still proceeds in the longitudinal direction. The result of this so called Rhines effect is the growth of longitudinally elongated structures that eventually form zonal flows (Williams, 1978). These ideas on two-dimensional fluid dynamics offer some qualitative insight not only into the behavior of the earth's atmosphere and oceans on large scales but also of the atmospheres of other planets. Perhaps the most famous planetary vortex of all is the Great Red Spot (GRS) on Jupiter.

The reason why the atmosphere behaves similar to 2D-flows is threefold. Firstly, the dynamics of the terrestrial atmosphere is mainly in a thin layer some 10 to 15 km high while the horizontal structures that develop are typically hundreds of km wide. The flow is restricted to be almost two-dimensional. Secondly, the atmosphere is often in hydrostatic equilibrium. This implies that the flow mainly takes place on horizontal planes. Thirdly, the Rossby number is often small. The Rossby number measures the relative importance of the nonlinear (inertial) term with respect to the

Coriolis term in the momentum equation. If the Rossby number is small fluid motion is forced to move as columns parallel to the rotation axis; this is the Taylor-Proudman theorem. It makes fluid motion also essentially two-dimensional.

The smallness of the Rossby number has another consequence, not only is flow usually in hydrostatic balance but also in geostrophic balance. This means that horizontal pressure gradients are balanced by the Coriolis force. The equivalence of a small Rossby number and a velocity field in geostrophic balance can be seen from an expansion of the fluid equations in the small Rossby number (e.g. Pedlosky, 1987). The flow is only approximately in balance, it is actually in so-called quasi-geostrophic balance. The single equation that follows from the expansion is the quasi-geostrophic vorticity equation. It describes the evolution of the geostrophic velocity field under non-geostrophic sources and sinks and expresses conservation of potential vorticity (see Sect. 1.5.1). It is very successful in describing atmospheric flows.

Similar phenomena are not just restricted to the atmosphere but can also occur in tokamak plasmas in the layer at the edge. Here it is the strong magnetic field that restricts motion to quasi two-dimensions. Electrostatic vortices are seen and they take care of part of the (particle) transport (Naulin and Spatschek, 1997). An equation similar to the quasi-geostrophic vorticity equation can be derived and it is known as the Hasegawa-Mima equation.

The goal of the present work is to investigate if similar phenomena might occur in an accretion disk. The similarity with the atmosphere was already mentioned: an accretion disk is thin, possibly in hydrostatic equilibrium and rotating. Can vortices like the GRS occur in an accretion disk? And if they do, could they be responsible for (part of) the angular momentum and mass transport?

1.5 Mathematical description

Fundamental relations which all fluids have to obey are conservation of mass, momentum and energy which can be expressed mathematically. The exact form of these equations depends on the system that is studied and the approximations that are made. For an accretion disk, the equations contain the usual time derivatives, the advection terms, the pressure gradient and gravity due to the central object. Extra physics that could be important include: self-gravity of the gas, dust, magnetic field, radiative transfer and relativistic effects. Here the choice is made to leave all of these out, and concentrate on the dynamics in its most simple form as this turns out to be complicated enough. The 3D gas equations are:

$$\begin{aligned} \frac{\partial \rho}{\partial t} + \nabla \cdot (\rho \vec{v}) &= 0, \\ \frac{\partial \vec{v}}{\partial t} + (\vec{v} \cdot \nabla)\vec{v} &= -\frac{1}{\rho}\nabla p - \nabla \Phi_{\mathrm{G}}, \\ \frac{\partial e}{\partial t} + \nabla \cdot [\vec{v}(e+p)] &= 0, \end{aligned} \tag{1.4}$$

where ρ is the density, $\vec{v}$ the velocity, p the pressure, Φ_G the gravitational potential, $e = \rho v^2/2 + p/(\gamma - 1) + \rho\Phi_G$ the energy density and γ the adiabatic index. It should be realized that these equations only describe adiabatic processes so that accretion leads to an increase in temperature as matter falls into the (negative) gravitational potential and a specific radiation process that cools the disk and gives rise to the radiation that we observe is not included in the last equation.

Because the disk is thin and possibly in hydrostatic equilibrium a further approximation is made by integrating the equations over the thickness of the disk. This gives the 2D gas equations:

$$\begin{aligned} \frac{\partial \Sigma}{\partial t} + \nabla \cdot (\Sigma \vec{v}) &= 0, \\ \frac{\partial \vec{v}}{\partial t} + (\vec{v} \cdot \nabla)\vec{v} &= -\frac{1}{\Sigma}\nabla P - \nabla \Phi_G, \\ \frac{\partial P}{\partial t} + \nabla \cdot (P\vec{v}) &= (1-\gamma) P \nabla \cdot \vec{v}, \end{aligned} \tag{1.5}$$

where Σ is the height integrated density or surface density and P and Φ_G are to be interpreted as height integrated quantities. The energy equation has been rewritten with the help of the continuity and momentum equations into an equation for the pressure. The physical justification for the approximation of two-dimensionality is weak (Chapter 3). The main reason to use it is that two-dimensional hydrodynamic simulations can easily be done on a workstation while 3D simulations place much higher demands on the computational resources. Add to it that the results of 3D simulations are often hard to interpret and it can be an enormous help to understand a comparable 2D situation. So it is generally believed that much can be learned about accretion disks by making this approximation, although I admit that 3D simulations of the phenomena presented in this thesis would improve the astrophysical relevance of this work.

A further approximation that is useful for a first approach is to use a polytropic relation between pressure and surface density ($P = K\Sigma^\gamma$). In this way there is no production of vorticity by baroclinic effects because surfaces of equal pressure and (surface) density coincide. Another consequence is that the entropy of the system is constant (no tricks are applied, $\gamma = \Gamma$ and K is just a constant). The 2D-polytropic gas equations in an inertial frame in cylindrical coordinates are:

$$\begin{aligned} \frac{\partial \Sigma}{\partial t} + \frac{1}{r}\frac{\partial r\Sigma v_r}{\partial r} + \frac{1}{r}\frac{\partial \Sigma v_\phi}{\partial \phi} &= 0, \\ \frac{\partial v_r}{\partial t} + v_r\frac{\partial v_r}{\partial r} + \frac{v_\phi}{r}\frac{\partial v_r}{\partial \phi} - \frac{v_\phi^2}{r} &= -\frac{1}{\Sigma}\frac{\partial P}{\partial r} - \frac{\partial}{\partial r}\left(\frac{-GM}{r}\right), \\ \frac{\partial v_\phi}{\partial t} + v_r\frac{v_\phi}{\partial r} + \frac{v_\phi}{r}\frac{\partial v_\phi}{\partial \phi} + \frac{v_r v_\phi}{r} &= -\frac{1}{\Sigma r}\frac{\partial P}{\partial \phi}, \\ P &= K\Sigma^\gamma, \end{aligned} \tag{1.6}$$

where the momentum equation is written in component form. The zeroth order

solution is just Keplerian rotation: $\Sigma = \Sigma_0, v_r = 0$ and

$$v_\phi = v_{\phi 0} = v_{\rm kep} = \sqrt{GM/r} = r\Omega(r). \tag{1.7}$$

Often a fixed point in the disk is chosen and the equations are written in a coordinate system co-rotating with the Keplerian speed at this point. This introduces the Coriolis acceleration $2\Omega\hat{z} \times \vec{v}$ on the left hand side of the momentum equation ($\hat{z}$ is the unit vector perpendicular to the disk) and the centrifugal force in the effective gravitational potential: $\Phi_{\rm G} = -GM/r - \Omega^2 r^2/2$ on the right hand side. Note that in these expressions Ω is now a constant.

Different interpretations can be given to these equations. They can describe a 2D polytropic gas, so an experiment in which the gas is in between two plates preventing any vertical motion (rigid lid boundary conditions on top and bottom of the gas). Alternatively, if the gas has a free surface, than a local increase of the pressure also implies a local increase in the thickness of the gas layer. Recently an extended set of equations was derived (Stehle and Spruit, 1999) which describes this case better. A third interpretation is if the fluid is incompressible. Then a local pressure increase is entirely due to an increase in thickness of the fluid layer. This corresponds with the shallow water equations ($\gamma = 2$).

1.5.1 Potential vorticity

Potential vorticity is a quantity of prime importance in geophysical fluid dynamics because it generalizes the concept of vorticity for the case of 2D compressible flow. Here only its shallow water form will be used which is a special form of Ertel's potential vorticity namely for the shallow water or 2D polytropic gas model. The derivation starts from the ideal 2D polytropic gas equations Eq. (1.6) which express conservation of mass and momentum. Taking the curl of the momentum equation and combining it with the continuity equation gives:

$$\left(\frac{\partial}{\partial t} + \vec{v}\cdot\nabla\right)\frac{\nabla\times\vec{v}}{\Sigma} = 0, \tag{1.8}$$

where $\nabla \times \vec{v}$ is the absolute vorticity which may include the vorticity of a rotating coordinate frame or planetary vorticity (2Ω). The term on which the differential operator works is the potential vorticity. Its attractiveness lies in the fact that it is just advected with the flow; its difficulty is that the advective velocity $\vec{v}$ is implicitly determined by the potential vorticity. The equation shows that motion of potential vorticity structures such as vortices often involve nonlinear effects and this explains why analytical results are hard to get. For example, a vortex (the perturbation) in a uniform shear flow (the basic state) is only able to withstand the stretching effect of the shear due to the nonlinear contributions in Eq. (1.8).

Comparison with incompressible flow, which is described by the vorticity equation:

$$\left(\frac{\partial}{\partial t} + \vec{v}\cdot\nabla\right)\nabla\times\vec{v} = 0, \tag{1.9}$$

shows that Eq. (1.8) is considerably more complicated because there is no unambiguous manner to invert potential vorticity to get the velocity field. This is possible for Eq. (1.9) with the introduction of the stream function ψ: $\vec{v} = \nabla \times \psi\hat{z}$ so that $\nabla^2\psi = \nabla \times \vec{v}$. To invert potential vorticity extra physical insight is needed. Observations of the earth's atmosphere and oceans show that large scale motion is often approximately in geostrophic equilibrium: the Rossby number is small. If the velocities in Eq. (1.8) are taken to be the geostrophic velocities ($2\Omega\hat{z} \times \vec{v} = -(\nabla P)/\Sigma$) then we are able to determine from the potential vorticity at a given time step the associated velocity field and thus propagate the solution in time. The resulting equation is known as the quasi-geostrophic potential vorticity equation. This line of work is an example of the wider class of balance models in which certain properties of the velocity field are assumed that allow the inversion of the potential vorticity equation. All of these models filter out the fast waves (Sect. 1.5.2) and only retain the slow advective component of the flow.

In astronomy this form of potential vorticity Eq. (1.8) is also known as vortensity. However, I prefer the term potential vorticity because that more accurately describes what it is: the vorticity of the gas if it is allowed to adjust (under conservation of angular momentum) to a surface density (pressure) of unity. This allows comparison of the vorticity of fluid parcels at different densities, which is important in for example stability analyses (Dowling, 1995).

1.5.2 Waves

It is always useful to start a dynamical study with small perturbations so that the equations Eq. (1.6) can be linearized and the fundamental waves determined. Linearization of the momentum equations around Keplerian rotation gives:

$$\begin{aligned}
\left(\frac{\partial}{\partial t} + \Omega(r)\frac{\partial}{\partial \phi}\right) v_{r1} - \xi(r) v_{\phi 1} &= -\frac{c_s^2}{\Sigma_0}\frac{\partial \Sigma_1}{\partial r}, \\
\left(\frac{\partial}{\partial t} + \Omega(r)\frac{\partial}{\partial \phi}\right) v_{\phi 1} + \eta(r) v_{r1} &= -\frac{c_s^2}{\Sigma_0 r}\frac{\partial \Sigma_1}{\partial \phi},
\end{aligned}$$

where $\xi(r) = 2\Omega(r)$ is the modified Coriolis parameter and $\eta(r) = \Omega(r)/2$ the vorticity of the basic state flow $v_{\phi 0}$. The product of ξ and η is equal to the epicycle frequency squared $\xi(r)\eta(r) = \kappa^2(r) = \Omega^2(r)$. From now on index 1 will be dropped. Assume that all variables behave as $\exp(i(m\phi - \omega t))$:

$$\begin{aligned}
-i(\omega - m\Omega(r)) v_r &= \xi(r) v_\phi - \frac{c_s^2}{\Sigma_0}\frac{\partial \Sigma}{\partial r}, \\
-i(\omega - m\Omega(r)) v_\phi &= -\eta(r) v_r - \frac{imc_s^2\Sigma}{\Sigma_0 r}.
\end{aligned}$$

Introduce the Doppler shifted frequency $\omega'(r) = \omega - m\Omega(r)$ which is a function of r and solve for the velocity components:

$$\left[\xi(r)\eta(r) - \omega'^2(r)\right] v_r = -i\frac{c_s^2}{\Sigma_0}\left(\frac{m\xi(r)}{r}\Sigma - \omega'(r)\frac{\partial \Sigma}{\partial r}\right),$$

$$\left[\xi(r)\eta(r) - \omega'^2(r)\right] v_\phi \quad = \quad \frac{c_s^2}{\Sigma_0}\left(\eta(r)\frac{\partial\Sigma}{\partial r} - \frac{\omega'(r)m}{r}\Sigma\right).$$

Proceed by substituting these expressions into the continuity equation:

$$i\omega'(r)\frac{\Sigma}{\Sigma_0} = \nabla\cdot\vec{v},$$

and simplify:

$$\frac{\xi(r)\eta(r) - \omega'^2(r)}{c_s^2}\Sigma = \frac{\partial^2\Sigma}{\partial r^2} + \frac{1}{r}\frac{\partial\Sigma}{\partial r} - \frac{m^2}{r^2}\Sigma + \frac{1}{\xi(r)\eta(r) - \omega'^2(r)}\times$$
$$\left\{2\frac{\eta(r)-\xi(r)}{r}\left[\frac{m}{r}(m\xi(r)+\omega'(r))\Sigma - (m\omega'(r)+\eta(r))\frac{\partial\Sigma}{\partial r}\right] + \right.$$
$$\left.\left[\frac{m}{r}\frac{\xi(r)}{\omega'(r)}\Sigma - \frac{\partial\Sigma}{\partial r}\right]\xi(r)\frac{d\eta}{dr}\right\}.$$

To get the dispersion relation we make a WKB approximation (introducing a radial wave number k and assuming all quantities to vary slowly in r) where only the gradient in background vorticity is retained ($d\eta/dr = \beta \neq 0$) because this is known to drive Rossby waves:

$$\frac{\xi\eta - \omega'^2}{c_s^2} = -k^2 + i\frac{k}{r} - \frac{m^2}{r^2} + \frac{1}{\xi\eta - \omega'^2}\times$$
$$\left\{2\frac{\eta-\xi}{r}\left[\frac{m}{r}(m\xi+\omega') - ik(m\omega'+\eta)\right] + \left[\frac{m}{r}\frac{\xi}{\omega'} - ik\right]\xi\frac{d\eta}{dr}\right\}. \qquad (1.10)$$

This dispersion relation can be simplified in the limit of large frequency $\omega' \gg \Omega, \xi, \eta$:

$$(\omega - m\Omega)^2 = \Omega^2 + \left(k^2 + \frac{m^2}{r^2}\right)c_s^2, \qquad (1.11)$$

and in the limit of small frequency $\omega' \ll \Omega, \xi, \eta$:

$$\omega - m\Omega = \frac{\xi}{\eta}\frac{\frac{m}{r}\frac{d\eta}{dr}}{k^2 + \frac{m^2}{r^2} + \frac{\Omega^2}{c_s^2}}. \qquad (1.12)$$

We recognize in the fast waves Eq. (1.11) sound waves (e.g. Binney and Tremaine, 1987) or inertia gravity waves (e.g. Pedlosky, 1987) and in the slow waves Eq. (1.12) Rossby waves (e.g. Montgomery and Kallenbach, 1997).

Here the Rossby waves are found to depend on the basic state vorticity gradient $(1/\eta)(d\eta/dr)$ but this is an artifact from the assumption that the basic state surface density is uniform. Rossby waves actually live on potential vorticity gradients so if the basic state surface density would depend on radius then this would contribute to the potential vorticity gradient. So η should be interpreted as the potential vorticity. The dispersion diagram is shown in Fig. 1.2.

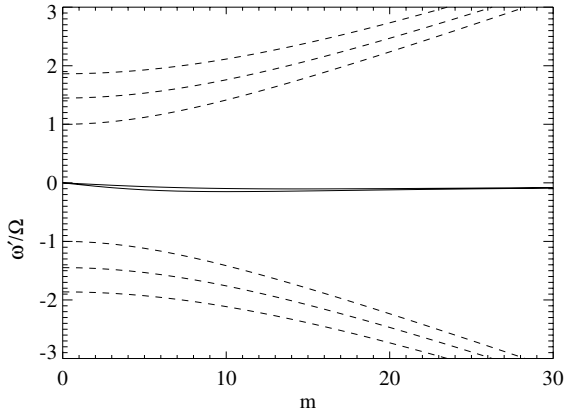

Figure 1.2: The dispersion diagram with the Doppler shifted frequency as a function of azimuthal wave number. For the sound waves (dashed lines) the modes with $k = 0$, $k = \pi/3H$ and $k = \pi/2H$ are given, while for the Rossby waves (solid lines) only $k = 0$ and $k = \pi/3H$. The aspect ratio of the disk is $H/R = 0.085$.

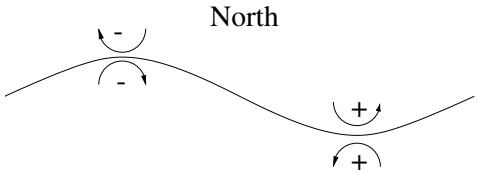

Figure 1.3: Sketch of a Rossby wave. High background potential vorticity is in the north, low in the south. A latitudinal potential vorticity contour is perturbed and positive and negative potential vorticity anomalies are indicated with plus and minus signs. The corresponding circulation makes the undulation move to the west.

The physical mechanism behind sound waves is fluid compressibility and change of pressure while that of Rossby waves is explained with the help of Fig. 1.3. An undulatory perturbation of a potential vorticity line implies that there are potential vorticity anomalies indicated by plus and minus signs. The circulation around these anomalies transports the wave in westward direction (where the north is defined as the direction of increasing background potential vorticity). The range of influence of the anomalies and thus the propagation speed is determined by the Rossby deformation radius:

$$L_{\rm D} = c_{\rm s}/\Omega, \tag{1.13}$$

which is an intrinsic horizontal length scale of the system. It makes the velocity fall off like a Yukawa potential (faster than $1/r$). Note that $L_{\rm D}$ happens to be similar to the thickness of the disk (the last uses the isothermal speed of sound).

1.6 Numerical simulations

1.6.1 Sound waves

As an illustration of sound waves in an accretion disk (which are analogous to shallow water Poincaré waves) a one dimensional (1.5D actually) simulation of an adjustment problem is done with the numerical code VAC (Tóth and Odstrčil, 1996; Tóth, 1997). The independence of the ϕ-coordinate guarantees that there are no Rossby waves ($m = 0$). The parameters of the accretion disk are the same as used in chapter 4 on a single vortex in an accretion disk ($\Omega = 1$, $R = 20$ and $H/R = 0.085$). Initially we place a high pressure and density region in the middle of the disk ($\Sigma = 1$ except for $19.6 < r < 20.4$ where $\Sigma = 1.1$). The subsequent evolution of the surface density is shown in Fig. 1.4. We observe two pulses running away from the region with the initial perturbation. The speed of propagation is approximately the speed of sound. We also see that a low density region develops behind the pulses. This is a signature of the dispersive nature of sound waves in accretion disks. The physical reason for the dispersion is that not only pressure is involved in wave propagation but also the Coriolis force (see also Fig. 1.5). If the Coriolis force gets enough time to turn the radial velocity into azimuthal velocity, so for long wavelengths, then wave propagation is slowed down. Or, in other words, angular momentum is conserved during the radial displacement which gives an extra contribution to the repelling force. For small wavelengths the dominant repelling force is still pressure and only for long wavelengths this extra repelling force makes a significant contribution. This makes the dispersion curve flatter and thus the propagation speed of the wave smaller.

Apart from the pulses running away we see that a density (and pressure) enhancement stays at the location of the initial perturbation. This is also a result of the Coriolis force which balances this pressure gradient. Fig. 1.5 shows the radial and azimuthal velocities at the same time as the last picture of Fig. 1.4. While the radial velocity is confined to the pulses, the azimuthal velocity shows oppositely directed "jets" near where the initial perturbation was. The Coriolis force working on these

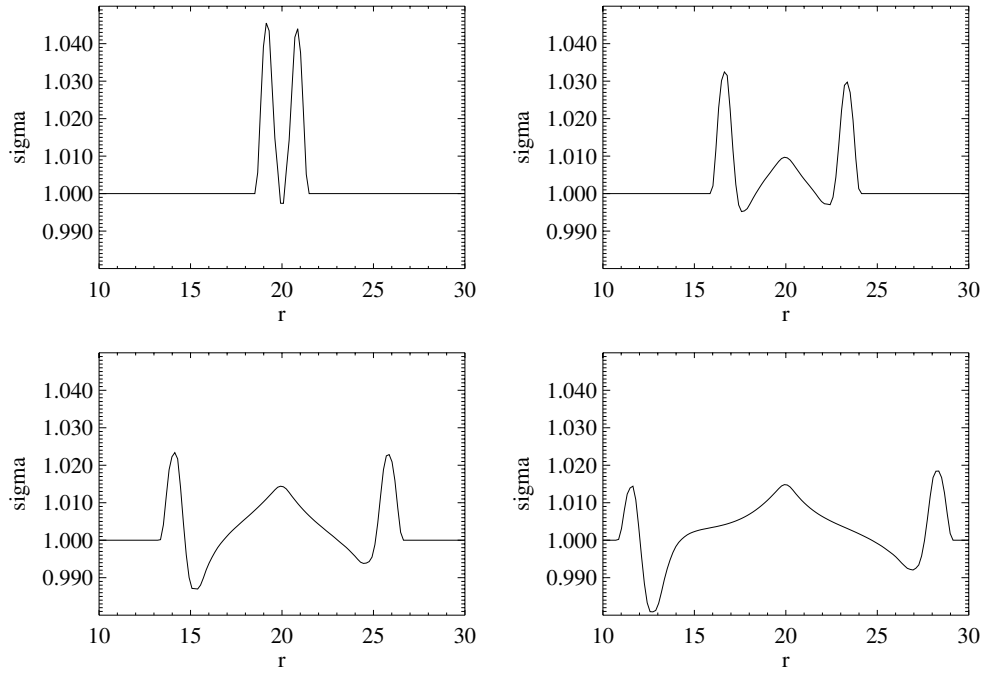

Figure 1.4: The surface density of a simulation showing sound waves after 0.064, 0.25, 0.45 and 0.64 $P_{\rm orb}$. Time is expressed in the Keplerian rotation time at $r = 20$.

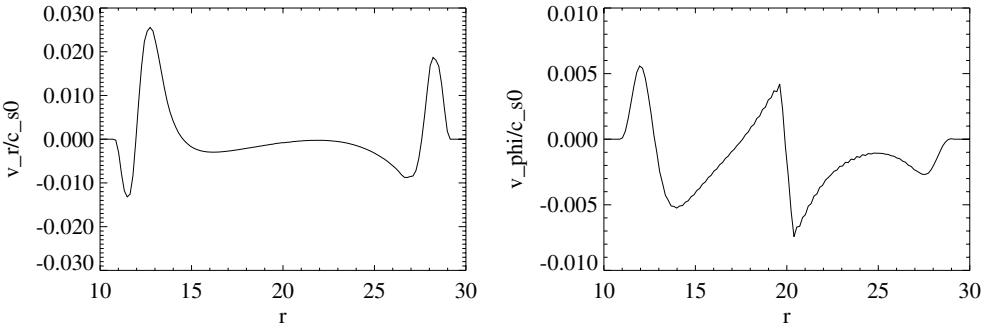

Figure 1.5: The radial velocity and the azimuthal minus the Keplerian velocity of the sound-wave simulation at 0.64 $P_{\rm orb}$.

"jets" is in geostrophic equilibrium with the pressure gradient from the density enhancement and this type of experiment is known as geostrophic adjustment in the literature. The typical width of the density enhancement is two Rossby deformation radii which has the value $L_D = 2$ for this experiment.

The formation of these azimuthal jets is also immediately clear from the point of view of potential vorticity advection. Initially ($t = 0$) there is low potential vorticity around $r = 20$. Since there is no significant radial velocity, this potential vorticity must stay localized at $r \approx 20$ and the formation of azimuthal flows is inescapable.

1.6.2 Rossby waves

Rossby waves are much harder to visualize than sound waves. Part of the reason is that a shallow water code always contains both families. A solution can be found in the work of Montgomery and Kallenbach (1997) on Rossby waves in hurricanes. Their work seems also to apply to accretion disks and the following discussion is mainly based on their article. It is noteworthy to remark that hurricanes, just like accretion disks, have a velocity profile that varies as $1/\sqrt{r}$ over a substantial range in radius.

The presence of sound waves is prevented by using a balance model (Sect. 1.5.1) in which these waves are absent. The specific model that is used is the Asymmetric Balance (AB) model (Shapiro and Montgomery, 1993) which has a wider range of applicability than for example quasi-geostrophic theory: it is also valid if the divergence (of velocity) is of comparable magnitude to the vorticity perturbations. The central approximation is that the square of the local Rossby number (the ratio of orbital frequency squared to the epicycle frequency squared) is small:

$$\frac{\left(\frac{\partial}{\partial t} + \frac{v_{\rm kep}}{r}\frac{\partial}{\partial \phi}\right)^2}{\eta(r)\xi(r)} = \frac{\left(\omega - m\frac{v_{\rm kep}}{r}\right)^2}{\Omega^2(r)} \ll 1,$$

although it even performs well if this is only marginally satisfied (Möller and Montgomery, 1999). If this approximation is applied to the 2D polytropic gas equations than a single, first order, differential equation in time can be constructed for the surface density (Montgomery and Kallenbach, 1997). All other quantities such as the velocities can be determined from the surface density and its tendency (time derivative). The nonlinear version of this model (Möller and Montgomery, 1999) was used for the following calculations. My implementation deviates from theirs in that I calculate the nonlinear terms not by convolutions but in real space at the expense of some extra Fourier transforms. Another difference is that I use the pseudo-momenta (the geostrophic approximation of the momenta) also for the nonlinear terms in the continuity equation. These changes facilitate the implementation considerably.

The dispersion relation for Rossby waves Eq. (1.12) indicates that if we want to see some waves propagating at all we should make sure that the denominator is not too large. This means in the first place that we should look at a hot disk were H is of comparable magnitude as R otherwise the last term is too large ($H/R = 0.71$ in the simulation below). Secondly, the radial wave number should be small. That is

why simulations are done on a disk that extends further inward ($3 < r < 37$) than in the simulation on sound waves. Thirdly, the azimuthal wave number should be small. We initialize the disk with an $m = 2$ perturbation in surface density centered at $r = 20$ such that the disturbance potential vorticity falls of as a Gaussian in radius ($\exp(-(r/4-5)^2)$). The subsequent evolution of the disturbance potential vorticity is shown in Fig. 1.6 as a 2D grayscale distribution. Since the main component still posses the $m = 2$ symmetry, more details can be observed in the cross-section plots of the disturbance potential vorticity in Fig. 1.7.

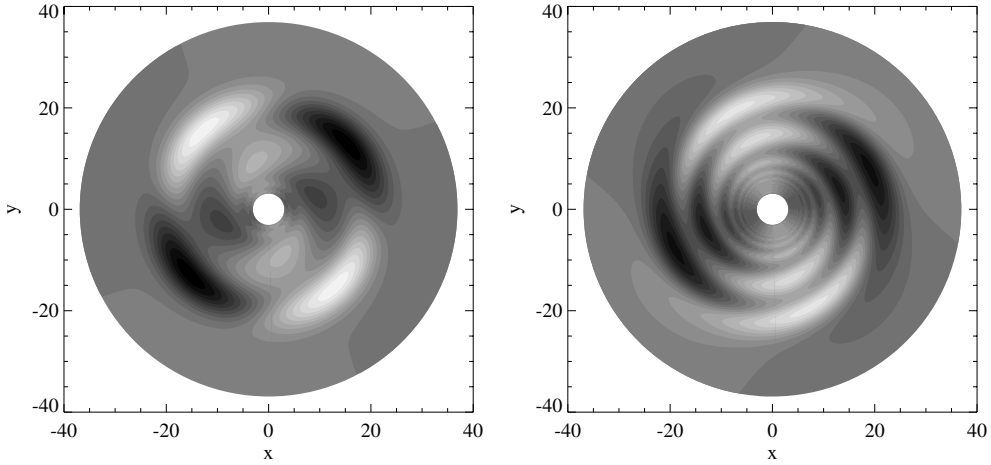

Figure 1.6: The 2D distribution of the linearized perturbation potential vorticity of a simulation on Rossby waves after t=0.095 and 0.334 $P_{\rm orb}$ as a grayscale plot.

We see that the initial perturbation at $r = 20$ gets sheared by the differential Keplerian rotation. This increases the radial wavenumber as is perhaps better observable in the cross section plots of the amplitude of the $m = 2$ perturbation than in the grayscale plots. Apart from the decrease in width of the peak at $r = 20$ we see a small shift to larger radius from $r = 20$ to $r = 20.65$ in 0.334 orbits around the compact object. This is in reasonable agreement with a displacement given by the group velocity:

$$c_{\rm gr} = -2k\frac{\xi}{\eta}\frac{\frac{m}{r}\frac{d\eta}{dr}}{\left(k^2 + m^2/r^2 + \Omega^2/c_{\rm s}^2\right)^2}, \tag{1.14}$$

where k is determined from the FWHM value of the initial peak ($\Delta r = c_{\rm gr}\Delta t = 0.54$).

The $m = 2$ perturbation at $r = 20$ drives flows at smaller and larger radii. Because of the steep Keplerian vorticity gradient at small radius, these radial flows lead to relative vorticity perturbations that show up as a series of wave packets in Fig. 1.7. They originate at the location of steepest Keplerian vorticity, so at the inner boundary, and travel outward with the local group velocity. The best example

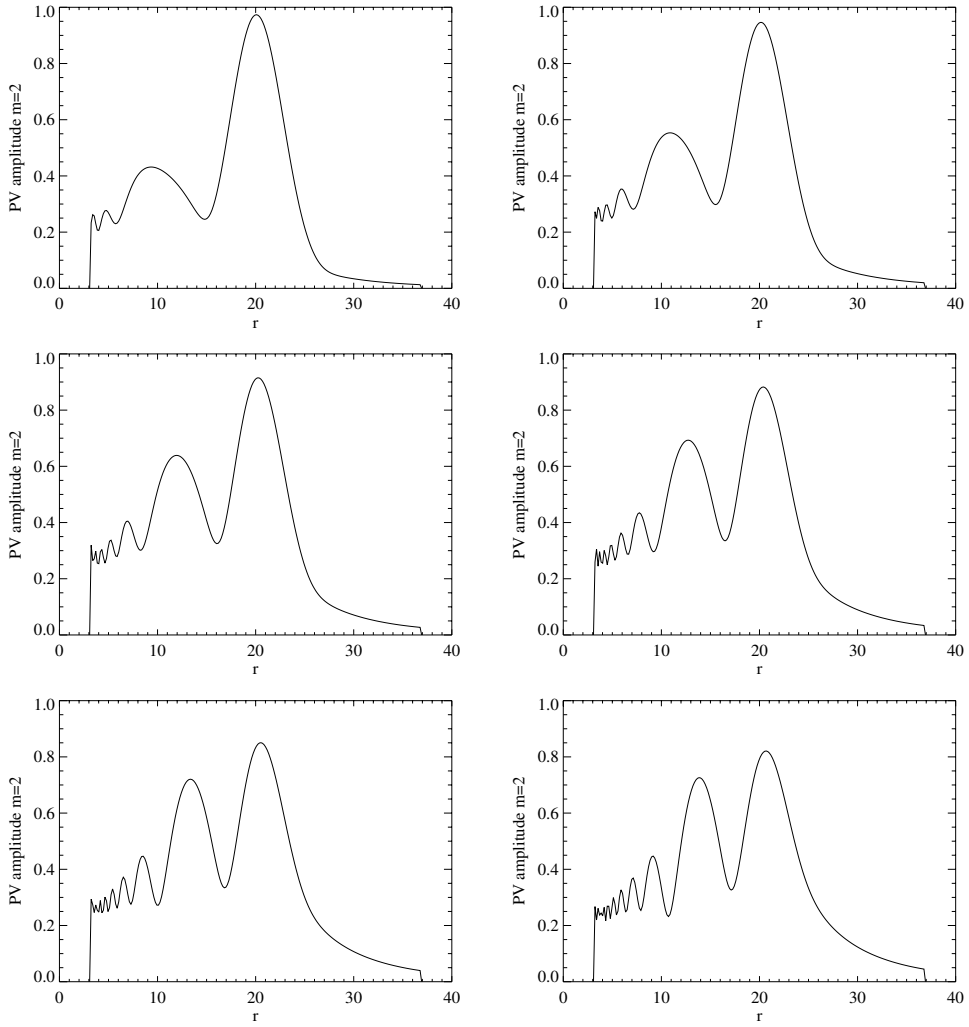

Figure 1.7: The linearized perturbation potential vorticity of the Rossby-wave simulation after t=0.095, 0.143, 0.191, 0.239, 0.286 and 0.334 $P_{\rm orb}$. The normalized amplitude of the $m = 2$ perturbation is shown.

is the packet at $r = 9.3$ (at $t = 0.095\ P_{\rm orb}$) that moves to $r = 13.9$ (at $t = 0.334\ P_{\rm orb}$). The shear-induced decrease of the radial wavelength of this packet is also clearly visible. Both this increase in wavenumber and the increase in radius lead to a decrease in the radial group velocity and eventually a stagnation radius is reached. This is very different from sound waves that can travel all the way to infinity. At the stagnation radius the shearing by Keplerian flow continues which resembles Rossby wave breaking, and energy and angular momentum are fed into the uniform flow ($m = 0$ component), see Fig. 1.8. Because of a correlation between radial velocity

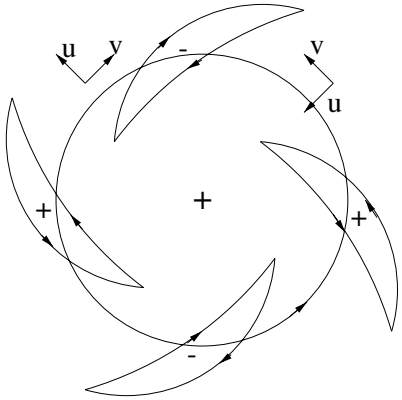

Figure 1.8: Sheared vorticity disturbances transport positive angular momentum towards and negative angular momentum out of the center because there is a positive correlation between radially inward perturbation velocity and positive azimuthal perturbation velocity.

and perturbed azimuthal velocity, excess angular momentum is transported inward and deficient angular momentum outward. Fig. 1.9 shows the change in the $m = 0$ component of the azimuthal velocity. If there were no Rossby wave propagation, the positive velocity "jet" would be at $r < 20$ and the negative "jet" at $r > 20$. With

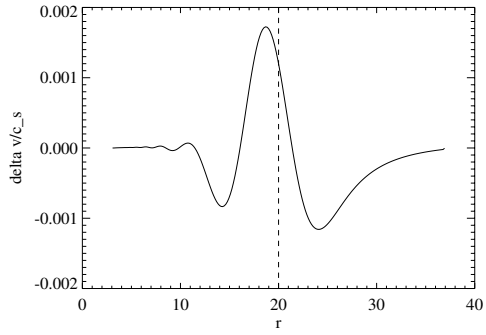

Figure 1.9: The non-Keplerian azimuthal velocity (m=0) at $t = 0.334\ P_{\rm orb}$. Rossby waves cause the peak to move to smaller radius.

Rossby wave transport the whole pattern is shifted to larger radius. In rectilinear shear flow the positive and negative jets would be of comparable magnitude but the circular geometry leads to asymmetry of the pattern whereby the positive jet is the stronger of the two. What is also visible from Fig. 1.9 is that my implementation of AB-theory has a problem with angular momentum conservation because all that should happen is a redistribution of angular momentum while it is clear that negative angular momentum is created in the broad and fairly deep negative jet. In the original implementation this is compensated for by an increase in surface density Montgomery (private communication).

The processes described above are thought to be important in hurricane intensification. For an accretion disk their relevance is less certain and often they are neglected, for example in the shearing sheet approximation (where the Keplerian velocity is approximated by a linear velocity profile). Above, the properties of Rossby waves in accretion disks were demonstrated for a very hot disk and with very large wavelength perturbations. With normal disk parameters ($H/R = 0.1$ or less) and wavelengths that are restricted to the thickness of the disk (e.g. $\lambda = 2H$) hardly any propagation can be seen because the denominator of the group velocity Eq. (1.14) is large. The net displacement can be estimated from the group velocity and the time over which the radial wavenumber changes substantially ($\Delta t = k/(n(d\Omega/dr))$) which gives:

$$\Delta r \approx \frac{4k^2}{r(k^2 + 1/H^2)^2} \approx \frac{1}{3}\frac{H}{R}H,$$

assuming that the azimuthal wavenumber is smaller than the radial wave number (a more accurate estimate is given in Montgomery and Kallenbach (1997)). As an illustration Fig. 1.10 shows the amplitude of the $m = 2$ potential vorticity perturbation and the change in azimuthal velocity for the same disk as was used in the sound wave simulation and with a narrower Gaussian perturbation $\exp(-(r-20)^2)$. Both the shift in the disturbance potential vorticity amplitude and in the non-Keplerian azimuthal velocity are barely visible.

In all of the above calculations the potential vorticity gradient is only due to the gradient in the Keplerian vorticity. If variation in background surface density is allowed then larger frequencies and group velocities could be found. These waves should then be called topographic Rossby waves.

1.7 Thesis outline and summary

Having summarized the analysis of the linear waves, it is time to take a step further and look at nonlinear phenomena and especially vortices. For that a numerical tool is needed, the development of which took most of the time. Based on previous work on vortices among which was the GRS, a numerical algorithm was chosen from geophysical fluid dynamics. It is presently used in, for example, the UCLA general circulation model. The merits of this algorithm are discussed in Chapter 2 where its

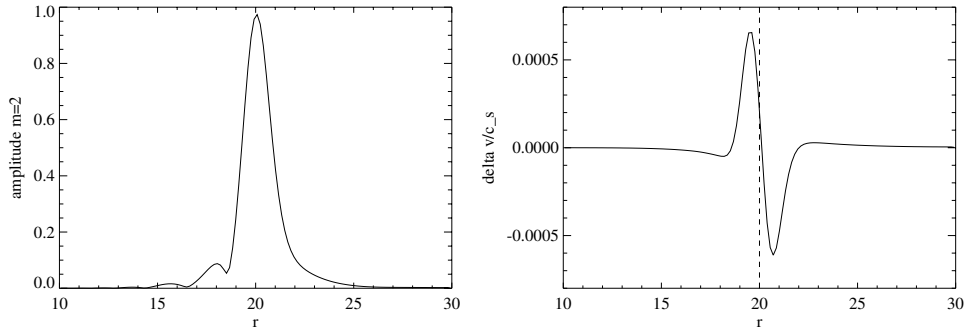

Figure 1.10: Rossby waves in the standard disk: it is cooler than that of Figs. 1.7 and 1.9 and the initial condition is narrower so that the wavelength of the perturbation is of the same order of magnitude as the disk thickness. On the left the disturbance potential vorticity of the m=2 mode, and on the right the non-Keplerian azimuthal velocity (m=0) at $t = 1.59\ P_{\rm orb}$.

performance is also compared with the VAC code. For the specific problem of vortices and their motion the code performs favorably in both accuracy and speed and it is used in all subsequent work.

In Chapter 3 we use the code to study two-dimensional turbulence. Traditionally this is done for homogeneous incompressible flow and this is first summarized. As these circumstances deviate strongly from those in an accretion disk, it seems worth to investigate the effect of rotation combined with compressibility and especially of a background shear flow. The latter is found to have a profound impact on the kind of vortices that can occur in an accretion disk. Only prograde vortices with a strength that is comparable to the Keplerian shear survive and then only if they are small enough. This implies that the conditions under which a two-dimensional description of the disk is justified (see Sect. 1.4), are not met. The Rossby number is not small and the horizontal size of the vortex is smaller than the vertical thickness of the disk. Ubiquitous vortices are therefore not expected in accretion disks.

With the correct parameters a vortex can survive in an accretion disk and the dynamical behavior of a single vortex is studied in Chapter 4. Here we look at the internal structure of a vortex and at its interaction with the surroundings. Internal force balance requires not only the Coriolis and pressure forces but also the centrifugal force (gradient wind balance). The vortex performs a nutation (wiggling motion) which can persist if the viscosity is low enough. Sound waves are excited and lead to two spiral shaped bores that extend over a large distance away from the vortex. The azimuthal drift of the vortex is small compared with the speed of sound and can be understood with β-gyres (a dipolar relative vorticity anomaly) which develop because the Keplerian flow bends around the vortex. The radial drift is an order of magnitude smaller than the azimuthal drift and might be related to the emission of sound waves that lead to the bore. Accretion rates that can be achieved with this radial drift are low also because only a small fraction of the disk is involved.

The previous study is extended in Chapter 5 with research on a single vortex but

now we also solve the energy equation, and on interactions of multiple vortices in a polytropic disk. Both effects have only a limited influence. The only influence of solving the energy equation is that shocks lead to heating of the disk. With two vortices, each one of them can interact with the bore of the other vortex. This leads to stronger losses of circulation than a single vortex experiences. With every passage nutation is started again. The radial drift of the vortex experiences stepwise changes during the interaction but the cumulative effect is an order of magnitude smaller than the ordinary drift. Vortex merger is accompanied by heavy losses of circulation that can make the merged vortex weaker than one of the individual vortices. During merger the positive vorticity envelope of the vortices is shed and replaced by a negative vorticity envelope. This influences the β-gyres that are excited and thus the azimuthal drift, but the order of magnitude estimate for the drift still holds. Merger delays the radial drift somewhat. When ten vortices are released in the disk, interactions are frequent and lead to considerable losses in circulation of individual vortices. The overall effect on the average radial drift is small so that it is concluded that vortex interactions are not able to increase the accretion rate, it is rather proportional to the number of vortices.

A Dutch summary is included at the end in Chapter 6.

Chapter 2

A High Reynolds Number Algorithm for Polytropic Accretion Disk Studies

Abstract. An algorithm is proposed to study two-dimensional vortices in thin, polytropic accretion disks. It is based on a method which has been used to study vortices in planetary atmospheres. It is special in that it conserves both energy and potential enstrophy in the absence of dissipation. This leads to desirable stability properties which permit calculations at relatively high Reynolds numbers. The algorithm is tested and compared to existing methods, in particular with a Total Variation Diminishing method.

M.D. Nauta and G. Tóth
Astronomy and Astrophysics **336**, 791-801, 1998

2.1 Introduction

To explain the "anomalous" large viscosity in a *thin* accretion disk different routes have been tried. Very successful is the approach using magnetic fields (Balbus and Hawley, 1991; Hawley and Balbus, 1991; Geertsema and Achterberg, 1992; Schramkowski, 1996). A magnetic field can link fluid parcels at different radii. Because of the differential motion, the magnetic field is stressed and transfers angular momentum from the innermost to the outermost parcel. The result is that an initial (small) radial separation of the fluid parcels increases. If this process occurs among neighboring parcels then this mechanism drives the Velikhov-Chandrasekhar magnetohydrodynamic (MHD) instability which amplifies the magnetic field and is responsible for MHD-turbulence (e.g. Brandenburg *et al.*, 1995). Another source of MHD-turbulence could be due to the buoyancy of magnetic flux tubes. This MHD-turbulence might explain the enhanced transport in an accretion disk. If the fluid parcels are connected by coronal magnetic field so that they can be further apart, then it was shown (Aly and Kuijpers, 1990) that transport of angular momentum is particularly effective and requires a non-local description (Kuijpers, 1995).

The hydrodynamic route faces more trouble. Pure hydrodynamic convection has been suggested but was found to transport angular momentum inwards in stead of outwards (e.g. Balbus *et al.*, 1996). Shear-driven instabilities have been proposed but pure Keplerian rotation is linearly stable so that a nonlinear instability is needed to drive the turbulence (Zahn, 1990). One example of such a nonlinear instability which might occur in an accretion disk is given as the last test case in this paper. It is known as the instability of sheared disturbances (Haynes, 1987). However, even though this quasi-Keplerian rotation does get unstable, the instability does not extract energy from the Keplerian shear, but merely from the disturbance superposed on the Keplerian profile. This is in agreement with the finding of Balbus *et al*. (1996) that it is impossible to transfer energy from the Keplerian flow into both the radial and the azimuthal fluctuating velocity components. One of these always returns its energy to the mean flow.

If the flow deviates from Keplerian, hydrodynamic instabilities can be expected. This can occur at the inner edge of the disk where it is in contact with the compact object or at the outer edge where matter impinges on the disk. Also throughout the disk the Keplerian flow can be distorted by magnetic fields. These instabilities might give rise to two-dimensional vortices or eddies and these are the topic of some recent hydrodynamic work (Abramowicz *et al.*, 1992; Kuijpers, 1995; Adams and Watkins, 1995). Large-scale 2-D vortices in disks had already been proposed by von Weizsäcker (1944). Also the work of Dubrulle was pointing in this direction (Dubrulle and Valdettaro, 1992). However, so far, numerical simulations of thin accretion disks have never given any hint for the existence of persistent vortices in disks [1].

Research of vortices and the related phenomenon of an inverse energy cascade in two dimensions relies heavily on direct numerical simulations. A breakthrough

[1] We learned about very recent simulations showing long-lived vortices (Bracco *et al.*, 1998) only after completion of this article

in this field was achieved when simulations could be done with a high Reynolds number (McWilliams, 1984). These simulations have put the ideas about inverse energy cascade and the associated emergence of coherent structures or vortices out of random initial conditions on a firm basis. Over the years this approach of using direct high-Reynolds number numerical simulations to study (quasi-) two-dimensional turbulence has developed from solving the 2-D incompressible Euler equations on a periodic Cartesian grid (McWilliams, 1984) into solving the shallow-water equations on the surface of a sphere (Cho and Polvani, 1996a). The latter simulation demonstrated the emergence of vortices and jets in decaying shallow-water turbulence on the surface of a fast spinning planet, and was specifically undertaken to model the flow on the four giant outer planets (Cho and Polvani, 1996b). Usually this kind of simulation is done with a pseudo-spectral code with very little dissipation. The small dissipation is often achieved by replacing the Laplacian with a higher order operator, e.g. biharmonic diffusion.

Because of the supersonic nature of the flow in thin accretion disks, simulations have been done with methods capable of representing shock waves (e.g. Różyczka and Spruit, 1993). Numerical oscillations generated at shock fronts are usually suppressed by introducing strong numerical diffusion. This can lead to unacceptably low Reynolds numbers that severely limit the ability to study turbulence. Here another choice is made. Initial conditions and parameters are chosen such that shocks don't occur and when they do and give trouble we terminate the calculation. This allows us to use techniques from geophysical fluid dynamics (GFD) that are more appropriate to the above mentioned high Reynolds numbers.

In this paper a simple numerical algorithm is proposed to solve the equations of a simplified model of an accretion disk. It can't handle shocks because of Gibbs oscillations but it does simulations at a high Reynolds number. The algorithm originates from GFD (Arakawa and Lamb, 1981) where it has been used very successfully to simulate parts of Jupiter (Williams and Wilson, 1988; Dowling and Ingersoll, 1989). If persistent vortices exist in accretion disks, this algorithm is a very likely candidate to find them. After discussing the equations and their approximations in Sect. 2.2 and the algorithm in Sect. 2.3, a number of numerical experiments demonstrate the performance of the algorithm (Sect. 2.4). Some of these test cases are used to compare the behavior of this algorithm with a shock capturing method as implemented in the freely available Versatile Advection Code (VAC) (Tóth and Odstrčil, 1996; Tóth, 1997). Actual simulations of vortices in an accretion disk will be presented in a following paper.

2.2 The equations

In this section it is shown that, under a number of assumptions, the equations describing the dynamics of a planetary atmosphere, which behaves as an incompressible fluid, are very similar to the compressible gas equations describing the dynamics in an accretion disk. The reason is that though the atmosphere is to a very good approximation incompressible ($\nabla \cdot \vec{v} = 0$), the two-dimensional divergence of the

horizontal velocity need not be zero as the atmosphere can increase in thickness. In this way a hydrostatic thin layer of incompressible fluid mimics a compressible two-dimensional gas. Because of this similarity, identical discretisations can be used for both systems. First, the equations of a planetary atmosphere are discussed, then those of an accretion disk.

We stress that not *all* aspects of the dynamics of a three dimensional *incompressible* flow can be represented by a *compressible* 2D gas, e.g. vortices in the vertical direction have no corresponding counterpart. For planetary atmospheric applications, however, the analogy works quite well.

2.2.1 The shallow-water equations

In the study of planetary atmospheres a number of different models are being used to describe the dynamics, the simplest of which is the shallow-water model. It describes the evolution of an ideal, thin, homogeneous layer of fluid under the simultaneous influence of the effective gravity and the Coriolis force. The corresponding equations are derived from the incompressible Euler equations under the assumption that the fluid layer is thin, homogeneous, and in hydrostatic equilibrium in the third dimension (Pedlosky, 1987, Sect. 3.3). The most important step in the derivation is the integration of the hydrostatic equation in the vertical direction, which allows the horizontal pressure gradient to be expressed as the gradient of the free surface height h:

$$\begin{aligned} \frac{\partial \vec{v}}{\partial t} + q(\hat{z} \times h\vec{v}) + \nabla(\frac{1}{2}v^2 + \Phi) &= 0, \\ \frac{\partial h}{\partial t} + \nabla \cdot (h\vec{v}) &= 0, \end{aligned} \tag{2.1}$$

$\vec{v}$ is the 2-D horizontal velocity, t is the time, q the potential vorticity $q = (f + \hat{z} \cdot \nabla \times \vec{v})/h$, f the planetary vorticity $f = 2\vec{\Omega} \cdot \hat{z}$, $\vec{\Omega}$ is the angular rotation frequency of the coordinate system (or the planet), $\hat{z}$ the unit vector in the local vertical direction, h the height of the free surface, and Φ the geopotential per unit mass $\Phi = gh$, with g the gravitational acceleration. These equations can be combined into one which describes the advection of potential vorticity:

$$\frac{\partial q}{\partial t} + \vec{v} \cdot \nabla q = 0. \tag{2.2}$$

Because the potential vorticity depends on the velocity, this equation describes advection of an active scalar, which is not easy to solve. A numerical scheme that solves the shallow-water equations should satisfy this advection property of potential vorticity in the best possible way.

Usually, discretisations of Eq. (2.1) require some form of viscosity to stabilize the small scales. However, the system exhibits an inverse cascade of kinetic energy in the rotational part of the velocity field and this could limit the unstable behavior on the small scales. The inverse cascade follows from the conservation of energy

and potential enstrophy (assuming that the net flux of these quantities through the boundaries of the domain remain zero). Firstly, conservation of energy implies:

$$\frac{\partial}{\partial t}\int\int\left(\frac{1}{2}hv^2+\frac{1}{2}gh^2\right)dA=0,$$

and secondly, conservation of potential enstrophy:

$$\frac{\partial}{\partial t}\int\int\left(\frac{1}{2}hq^2\right)dA=0.$$

Since the potential enstrophy is conserved, the ordinary enstrophy has a constant upper bound:

$$\int\int\left(\frac{1}{2}h^2q^2\right)dA\leq\int\int\left(\frac{1}{2}h_{\max}hq^2\right)dA.$$

From this point to arrive to the inverse energy cascade is very similar to the 2-D incompressible case (Pedlosky, 1987, Sect. 3.28). In Fourier space the relative enstrophy can be written as ($\vec{k}$ is the 2-D wave vector, the planetary vorticity is neglected here):

$$\begin{aligned}&\int_0^\infty\int_0^\infty\frac{1}{2}|\vec{k}\times\vec{v}|^2d^2\vec{k}\\&=\int_0^\infty\int_0^\infty\frac{1}{2}\left(k^2v^2-(\vec{k}\cdot\vec{v})^2\right)d^2\vec{k},\\&=\int_0^\infty\int_0^\infty k^2E_{\rm rot}(k)d^2\vec{k},\end{aligned}$$

$E_{\rm rot}(k)$ is the kinetic energy density in 2D $\vec{k}$-space per unit mass of the rotational component of the velocity. If the rotational part of the kinetic energy is conserved (which is a reasonable approximation because of conservation of total energy) and nonlinear interactions move part of that energy to higher wave numbers, then the upper bound on the enstrophy implies that the bulk of that energy moves to lower wave numbers. It cascades in the inverse direction, all very analogous to the inverse cascade in 2D-incompressible fluids.

If it is possible to write a numerical algorithm for the shallow-water equations such that the discretised equations conserve energy and potential enstrophy, then part of the instability problems of ordinary codes at large wave numbers will not occur because of the correct energy cascade. For this reason it may be expected that, with such an energy and potential enstrophy conserving code, stable simulations are possible at higher Reynolds numbers than with a code that does not enforce the correct energy cascade. Arakawa and Lamb (1981) wrote an algorithm which satisfies both conservation properties. For completeness the algorithm is given in Sect. 2.3.

As already hinted at, this code still requires some dissipation (Bennett and Haidvogel, 1983). This is because the enstrophy is cascading in the ordinary direction, towards large wave numbers. If there was no dissipation, enstrophy would pile up

at the largest wave number and would give rise to non-physical oscillations. This process is sometimes called enstrophy equipartitioning. In real space this would show up as sharp conspicuous peaks in the spatial distribution of potential vorticity. To suppress such peaks the dissipation process needs to be large enough.

Different forms of the dissipation operator are in use. This is, because for high Reynolds number flow, the grid resolution is insufficient to describe the phenomena taking place at the dissipation scale. Consequently, the dissipation operator should not describe molecular viscosity but the influence of sub-grid scale motions. Although a physically well funded representation of sub-grid scale motions is not known, it is common practice to use a Laplacian operator to some power. That is why the right hand side of Eq. (2.1) is replaced with (for all three equations):

$$-\nu(-\nabla^2)^\alpha \cdot$$

where the dot stands for the velocity component or the height respectively. A value for α of unity is appropriate for molecular viscosity (in an incompressible medium), while α larger than unity is called hyperviscosity. A special form of hyperviscosity is biharmonic diffusion: $\alpha = 2$. By increasing α the dissipation operator gets more selective. The same amount of dissipation (of potential enstrophy in 2D-simulations) can be achieved over a shorter range of wave numbers, allowing for a larger inertial range. So it is as if a higher Reynolds number flow is simulated if α is increased. A different way to achieve this effect is to use a larger grid which is not always possible because of limited computational resources. This explains the popularity of hyperviscosity in high Reynolds number research. The physical implications of its use are ill understood and the topic of many controversies. Some physical phenomena, such as the existence of an inverse energy cascade and the formation of coherent structures, are robust. Others, such as the slope of the spectrum in the inertial range, do depend on the form of viscosity (Cho and Polvani, 1996a). Since it has been used so widely it seems justified to apply it here (with care) as well.

2.2.2 The polytropic gas equations

The equations describing the dynamics in an accretion disk are not the shallow-water equations but the MHD equations with radiative transfer. However to explore possible similarities between flow in planetary atmospheres and in accretion disks, a number of simplifying assumptions can be made so that the resulting equations are similar to the shallow-water equations. Firstly, the effects of magnetic fields and radiative transfer are neglected. Secondly, the disk is assumed to be thin and in hydrostatic equilibrium so that the equations can be integrated over the height of the disk resulting in a two dimensional description. A further simplification is required because the resulting equations don't just advect potential vorticity but also produce it by the baroclinic term:

$$\frac{\nabla\Sigma \times \nabla P}{\Sigma^2},$$

where the pressure should be interpreted as the height integrated pressure and Σ stands for the height integrated density. To eliminate this production term and to

focus on the dynamics, keeping the energetics as simple as possible, a polytropic equation of state is assumed:

$$P = K\Sigma^{\gamma}.$$

This assumption simplifies the baroclinic model to a barotropic one. For a planetary atmosphere it is known from observations that a barotropic model (the shallow-water equations) already describes many interesting phenomena. Unfortunately such observations are missing for an accretion disk, but assuming a polytropic relation is quite common in theoretical studies (e.g. Goldreich *et al.*, 1986). The resulting equations are:

$$\begin{aligned} \frac{\partial \vec{v}}{\partial t} + q(\hat{z} \times \Sigma\vec{v}) + \nabla\left(\frac{1}{2}v^2 + \Phi\right) &= 0, \\ \frac{\partial \Sigma}{\partial t} + \nabla \cdot (\Sigma\vec{v}) &= 0, \end{aligned} \tag{2.3}$$

where q is the potential vorticity $q = (f + \hat{z} \cdot \nabla \times \vec{v})/\Sigma$ and $\Phi = \gamma P/((\gamma - 1)\Sigma) - GM/r - \Omega^2 r^2/2$ contains the enthalpy and the effective gravitational potential (due to the central compact object). The similarity with the shallow-water Eqs. (2.1) is obvious. The 2D polytropic gas equations, in the absence of a gravitating central object, even become identical to the shallow-water equations (replacing h with Σ) if $\gamma = 2$ (making Φ a linear function of Σ) and if $g = 2K$. It goes without saying that the waves of both sets of equations are basically the same, they just have different names, i.e. gravity waves in the shallow-water case versus sound waves in the polytropic case. Because of this similarity of the equations, an identical algorithm can be used both for the shallow-water equations and for the polytropic gas equations. As the conservative discretisation of Arakawa and Lamb has proven to be successful in the research of vortices on Jupiter (Williams and Wilson, 1988; Dowling and Ingersoll, 1989), it was decided to use this algorithm also to study vortices in accretion disks.

2.3 The algorithm

The Arakawa-Lamb scheme discretises the spatial part of the differential Eqs. (2.1) and (2.3) to second order. The time integration can be done with a standard method such as leap-frog or Runge-Kutta. The scheme uses a staggered grid known as the Arakawa C grid, see Fig. 2.1. The grid shows that the dependent variables are not calculated at every location. For example, to update the horizontal velocity component u at location $i, j + 1/2$, the velocity component v is needed at that same location $i, j + 1/2$ but according to Fig. 2.1 it is unknown here. By taking a linear combination of this velocity component in the surrounding grid points, i.e. at $i + 1/2, j$; $i + 1/2, j + 1$; $i - 1/2, j$ and $i - 1/2, j + 1$, some freedom is introduced in the discretisation. This degree of freedom is used to satisfy the constraints of conservation of both energy and potential enstrophy. These constraints determine which linear combinations have to be taken. The resulting algorithm (using the same notation as before) is given in Table 2.1. One of us (MDN) has implemented this algorithm together

Table 2.1: The algorithm

$$
\begin{aligned}
\frac{\partial}{\partial t}h_{i+1/2,j+1/2} &= -\frac{1}{\Delta}\left[u^*_{i+1,j+1/2} - u^*_{i,j+1/2} + v^*_{i+1/2,j+1} - v^*_{i+1/2,j}\right] \\
\frac{\partial}{\partial t}u_{i,j+1/2} &= \alpha_{i,j+1/2}v^*_{i+1/2,j+1} + \beta_{i,j+1/2}v^*_{i-1/2,j+1} + \gamma_{i,j+1/2}v^*_{i-1/2,j} + \\
&\quad \delta_{i,j+1/2}v^*_{i+1/2,j} - \epsilon_{i+1/2,j+1/2}u^*_{i+1,j+1/2} + \epsilon_{i-1/2,j+1/2}u^*_{i-1,j+1/2} - \\
&\quad \frac{1}{\Delta}\left[(K+\Phi)_{i+1/2,j+1/2} - (K+\Phi)_{i-1/2,j+1/2}\right] \\
\frac{\partial}{\partial t}v_{i+1/2,j} &= -\gamma_{i+1,j+1/2}u^*_{i+1,j+1/2} - \delta_{i,j+1/2}u^*_{i,j+1/2} - \alpha_{i,j-1/2}u^*_{i,j-1/2} - \\
&\quad \beta_{i+1,j-1/2}u^*_{i+1,j-1/2} - \phi_{i+1/2,j+1/2}v^*_{i+1/2,j+1} + \phi_{i+1/2,j-1/2}v^*_{i+1/2,j-1} - \\
&\quad \frac{1}{\Delta}\left[(K+\Phi)_{i+1/2,j+1/2} - (K+\Phi)_{i+1/2,j-1/2}\right]
\end{aligned}
$$

with

$$
\begin{aligned}
u^*_{i,j+1/2} &= \frac{1}{2}\left(h_{i+1/2,j+1/2} + h_{i-1/2,j+1/2}\right)u_{i,j+1/2} \\
v^*_{i+1/2,j} &= \frac{1}{2}\left(h_{i+1/2,j+1/2} + h_{i+1/2,j-1/2}\right)v_{i+1/2,j} \\
\alpha_{i,j+1/2} &= \frac{1}{24}\left[2q_{i+1,j+1} + q_{i,j+1} + 2q_{i,j} + q_{i+1,j}\right] \\
\beta_{i,j+1/2} &= \frac{1}{24}\left[q_{i,j+1} + 2q_{i-1,j+1} + q_{i-1,j} + 2q_{i,j}\right] \\
\gamma_{i,j+1/2} &= \frac{1}{24}\left[2q_{i,j+1} + q_{i-1,j+1} + 2q_{i-1,j} + q_{i,j}\right] \\
\delta_{i,j+1/2} &= \frac{1}{24}\left[q_{i+1,j+1} + 2q_{i,j+1} + q_{i.j} + 2q_{i+1,j}\right] \\
\epsilon_{i+1/2,j+1/2} &= \frac{1}{24}\left[q_{i+1,j+1} + q_{i,j+1} - q_{i,j} - q_{i+1,j}\right] \\
\phi_{i+1/2,j+1/2} &= \frac{1}{24}\left[-q_{i+1,j+1} + q_{i,j+1} + q_{i,j} - q_{i+1,j}\right] \\
q_{i,j} &= \frac{f + \frac{1}{\Delta}\left[v_{i+1/2,j} - v_{i-1/2,j} - u_{i,j+1/2} + u_{i,j-1/2}\right]}{\frac{1}{4}\left(h_{i+1/2,j+1/2} + h_{i+1/2,j-1/2} + h_{i-1/2,j+1/2} + h_{i-1/2,j-1/2}\right)} \\
K_{i+1/2,j+1/2} &= \frac{1}{4}\left[u^2_{i+1,j+1/2} + u^2_{i,j+1/2} + v^2_{i+1/2,j+1} + v^2_{i+1/2,j}\right]
\end{aligned}
$$

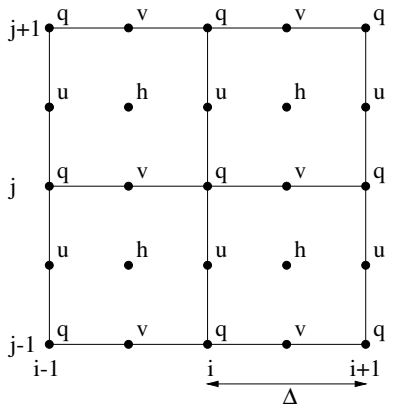

Figure 2.1: The staggered Arakawa C grid.

with the polytropic relation of Sect. 2.2.2 which is used to calculate Φ. Non-Cartesian grids are discretised by taking metric factors into account, so that the equations can also be used on the surface of a sphere or in a thin disk.

Boundary conditions are implemented with the help of ghost cells surrounding the computational domain. We use reflective and periodic boundary conditions in the test problems, since these allow us to check the conservation properties of the algorithms. Reflective boundaries are represented by updating the ghost cell values at every time step using the symmetry and anti-symmetry across the physical boundary, while periodic boundaries can also be implemented trivially. Other type of boundary conditions, like non-reflective, are perhaps possible with an appropriate extrapolation method.

2.4 Numerical experiments

In order to verify the performance of the code, it has been applied to a number of simple flow problems studied in the literature.

2.4.1 The shearing instability

In astrophysics this instability is better known as the Kelvin-Helmholtz instability. However in the geophysical context the latter term seems to be reserved for shearing instabilities in a stratified fluid. To avoid ambiguity, the term shearing instability is used here.

Probably the most wide-spread astrophysical explanation of this instability makes use of Bernoulli's law. Geophysics offers a complementary description using Rossby waves (potential vorticity waves) which is also very illuminating (e.g. Hoskins *et al.*, 1985, Sect. 6). The flow pattern used in this calculation consists of a piecewise linear profile indicated in Fig. 2.2. The associated potential vorticity is negative and uni-

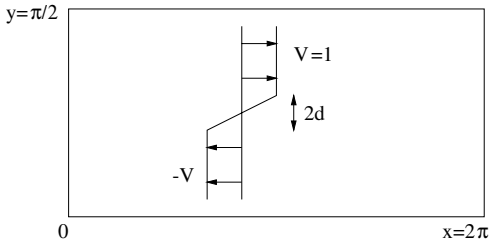

Figure 2.2: Flow geometry for shearing instability.

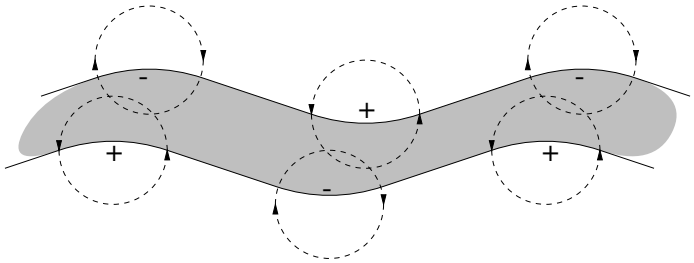

Figure 2.3: Part of the negative potential vorticity strip associated with the flow geometry of Fig. 2.2. A wavy perturbation has been applied to investigate the stability. The plus and minus signs indicate the position where an excess or deficit of potential vorticity exists compared with the unperturbed potential vorticity strip. The rotation directions associated with the anomalies are indicated with dashed circles. The instability can be explained by the influence of the velocity field (at the location of the arrowheads) on the perturbed potential vorticity strip as discussed in the text.

form in the shear layer. Suppose there is an infinitesimal sinusoidal displacement of the boundary of this strip as indicated in Fig. 2.3. The potential vorticity anomalies are marked with plus and minus signs. The velocities associated with these anomalies are indicated with dashed circles. The velocity field of the anomalies at the top of the potential vorticity strip propagate the top undulation to the left. The bottom wave moves to the right under the influence of its own velocity field. Both waves move in directions opposite to the local shear flow. These waves can be called Rossby waves and, depending on the phase velocity $v_{\rm ph} = -\beta/(k_x^2 + k_y^2 + F^2)$, they might be (almost) stationary. Here β is the gradient in potential vorticity, k_x and k_y are the components of the wave vector, and F is the ratio of planetary vorticity to the speed of sound. Considering the influence of one Rossby wave on the other exposes the instability mechanism. Firstly, the almost stationary Rossby wave becomes truly stationary because it is opposed or helped (depending on the phase difference) in its propagation against the shear flow by the Rossby wave on the other side of the potential vorticity strip. Secondly, the undulation of one Rossby wave is positively correlated with the velocity of the other Rossby wave. This leads to growth of the wave amplitude.

This mechanical description of the shearing instability leads to a very clear understanding of a sequence of stability criteria which started with Rayleigh's inflection point criterion (Rayleigh, 1880) and culminated in the work of Arnol'd (1969). (For a very readable review consult Dowling (1995, Sect. Stability)). Firstly, a 2D-flow is stable if the velocity and the potential vorticity gradient are of opposite sign everywhere. Secondly, a flow is stable if the velocity and the potential vorticity gradient are of the same sign and the flow speed is larger than the phase speed of the fastest Rossby wave. Both criteria describe conditions that prevent the occurrence of stationary Rossby waves that can lock in phase.

This well studied instability is used here as a test to compare the analytical growth rate to the numerically simulated one. For this comparison, a very simple flow pattern is used, but the shearing instability also finds applications in more complicated situations such as the instability in thick accretion tori (Goldreich *et al.*, 1986), where the principal branch can be associated with it. Here the simulation domain is rectangular, $2\pi \times \pi/2$, with two periodic and two reflective free-slip boundaries. (All quantities are in non-dimensional units.) Because of the periodic boundary conditions, only waves with a wavelength that is an integer fraction of 2π are admitted. So the wave modes have wave numbers: $k_x = 2\pi/\lambda = m$ with $m = 1, 2, 3\ldots$. The equations solved are Eq. (2.1) with an initial piecewise linear velocity profile as indicated in Fig. 2.2. The shear layer has a width of $2d = 0.19$, the density is initially uniform ($\rho = 1$) and the Mach number $V/c_s = 0.1$ so that a sound wave crosses the width of the box approximately 6 times in one unit of time. Calculations are performed with a Courant number of 0.9. A small random perturbation of amplitude 10^{-10} is added to the velocity to start up the instability.

To calculate the growth rate of the instability, the kinetic energy per unit mass per wave number (k_x, k_y) has been calculated and is then summed over k_y. The logarithm of this energy $E(k_x)$ is plotted as a function of time for the 7 lowest wave modes in Fig. 2.4. The $m = 4$ and $m = 5$ modes are the fastest growing, which is in agreement

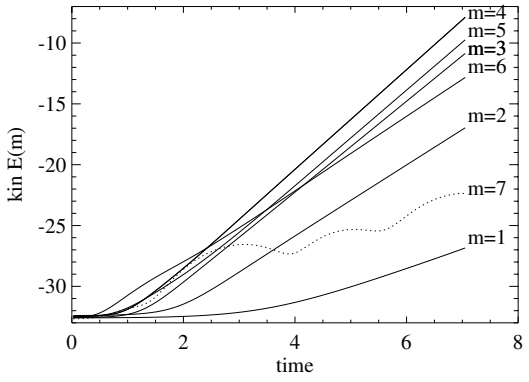

Figure 2.4: Kinetic energy versus time for the shearing instability on a 64×64 grid. The first stable mode $m = 7$ is indicated with a dotted line.

Table 2.2: Comparison of the numerically calculated dimensionless growth rates of the shearing instability for three different resolutions and their analytical values from Ong and Roderick (1972).

mode	growth rate Γ			
m	analytical	32×32	64×64	128×128
1	0.082	0.074	0.077	0.078
2	0.143	0.131	0.138	0.139
3	0.182	0.165	0.177	0.179
4	0.199	0.178	0.194	0.197
5	0.190	0.174	0.187	0.187
6	0.140	0.155	0.145	0.140

with the rule of thumb that the most unstable wave has a wavelength of 2π times the width of the shear layer. The growth rates determined in this way are compared to analytical results (Ong and Roderick, 1972), Table 2.2. The growth rate has been scaled with the width of the shear layer (as in Ong and Roderick, 1972), $\Gamma = \gamma d/V$ where γ is the measured growth rate. It is clear that the simulations are in agreement with linear stability theory. It can be concluded that the implementation is correct and that the code describes this kind of instabilities correctly.

2.4.2 The partner-exchange dipole vortex collision

This experiment was performed to compare the Arakawa-Lamb scheme with a typical shock-capturing algorithm. As a prototype of these methods, the Total Variation Diminishing (TVD) method of Harten (1983) as it is implemented in VAC (Tóth and Odstrčil, 1996; Tóth, 1997) has been used. TVD methods discretise a conservative hyperbolic system of equations, such as the shallow-water equations, with a limiting function applied to the fluxes to prevent numerical oscillations.

The experimental set up of this test is based on laboratory experiments of dipole collisions (van Heijst and Flór, 1989) and the phenomena are schematically indicated in Fig. 2.5. In the experiment, dyed fluid was injected trough two small pipes on both sides of a square tank filled with a stratified fluid. First two turbulent plumes formed, then owing to the stratification the vertical velocity component collapsed, the fluid behaved as if it was two-dimensional, and two dipolar vortices formed. These traveled towards each other and collided. During the collision, opposite halves of each dipole bounded together to form two new dipoles. These new dipoles moved away from each other in the horizontal plane under an angle with respect to the original paths of the dipoles. Depending on the parameter setting, a second collision could follow.

In an attempt to reproduce the above described process, Eq. (2.1) is solved numerically on a square domain. Initially two jet like structures are superimposed on a uniform state ($\rho = 1, v = 0, c_s = 4$) as shown in Fig. 2.6. In this figure the area of

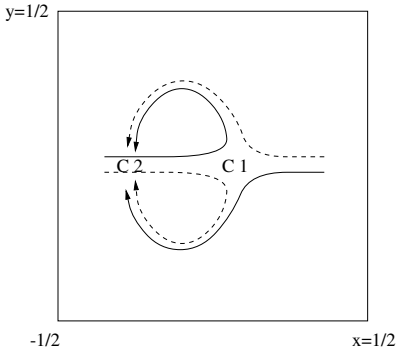

Figure 2.5: Schematic path of the vortices. At C1 the first dipole collision occurs, at C2 another one might follow depending on the strength of the vortices. The two vortices with positive vorticity are indicated with solid lines, the two with negative vorticity with dashed lines.

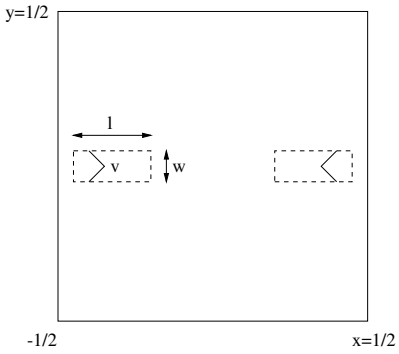

Figure 2.6: Numerical initial condition for partner-exchange dipole collision. The dashed boxes give the area of the jet like structures. Their velocity profiles are indicated within these regions.

the "jet" is indicated with a dashed line. On this area the "jet" has a linear velocity profile: $v_x(y) = v_{\max}(1 - 2|y|/w)$. In this way the injection of fluid through a pipe is simulated. The parameters for the left "jet" are: $l = 0.2, w = 0.1, v_{\max} = 2$, and for the right "jet": $l = 0.2, w = 0.1, v_{\max} = -1.5$. Because the "jets" are not of equal strength, this simulation is qualitatively very similar to the interaction described in (van Heijst and Flór, 1989) which led to a second dipole collision.

This initial state is evolved in time both with the Arakawa-Lamb algorithm and with the TVD scheme with Woodward limiters with a Courant number of 0.9. The potential vorticity distribution at some typical times is displayed in Fig. 2.7. The last picture is taken at the moment that the vortices in the Arakawa-Lamb calculation are undergoing their second dipole collision C2. The vortices in the TVD calculation however, are just halfway between collision C1 and C2. This indicates that the TVD

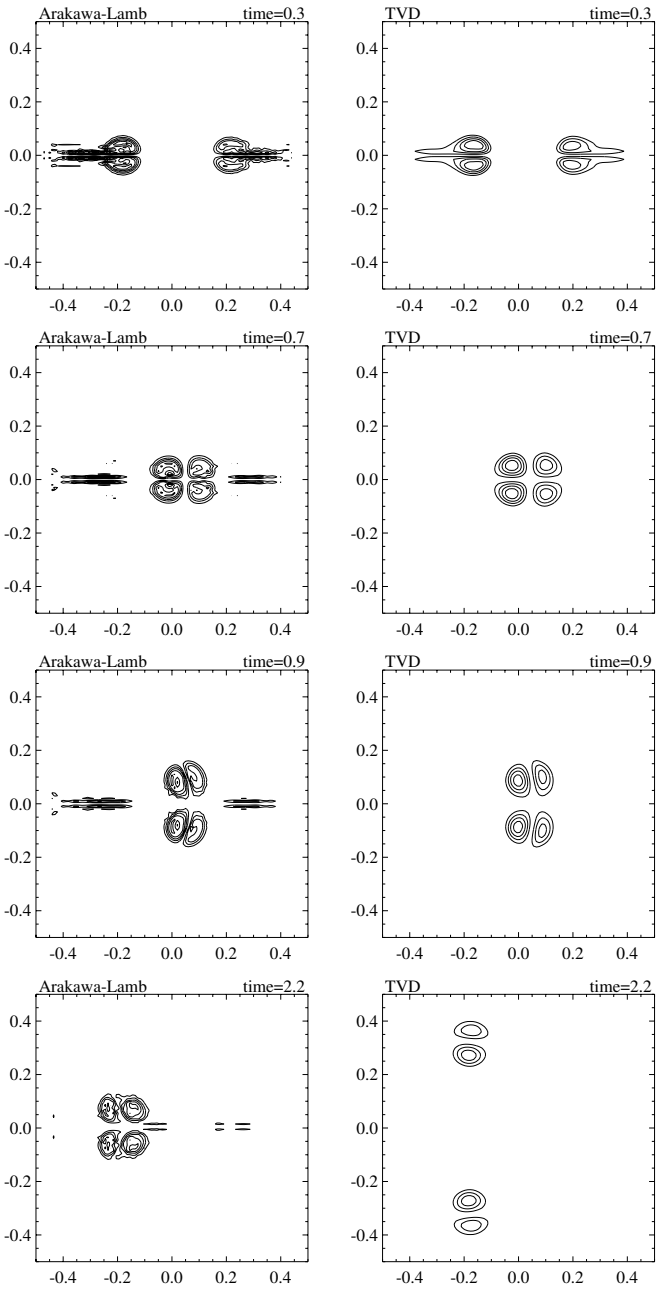

Figure 2.7: Dipole vortex collision shown in potential vorticity for four different times. The left pictures show the simulation with our Arakawa-Lamb scheme, the right with TVD. The contour interval is 10 and the zero-contour has been left out.

algorithm is much more diffusive in potential vorticity. The dipoles are larger and smoother, the peak potential vorticity is smaller and the propagation speed of the dipoles is lower. Also the distribution of potential vorticity is very smooth, which seems to be in disagreement with the dye distribution of the laboratory experiment (van Heijst and Flór, 1989) and the Arakawa-Lamb calculation.

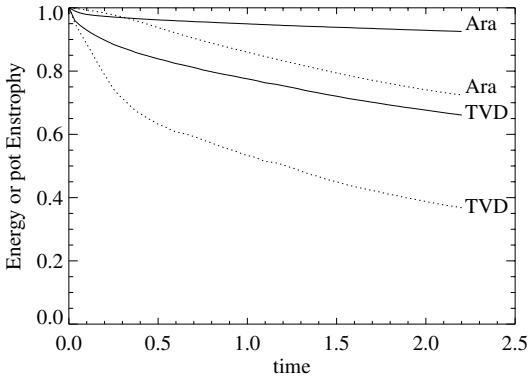

Figure 2.8: Evolution of total energy (solid lines) and potential enstrophy (dotted lines) for the dipole collision for both numerical algorithms. All data are normalized to their initial values.

This diffusiveness is confirmed by the graph of the energy and potential enstrophy as a function of time, Fig. 2.8. For an ideal fluid these quantities should be conserved. However to prevent enstrophy pile-up (Sect. 2.2.1) a small ($\nu = 5 \cdot 10^{-10}$) biharmonic diffusion has been added to the Arakawa-Lamb scheme which explains the decrease in both energy and potential enstrophy. The influence of this small diffusion on the position of the vortices, as shown in Fig. 2.7, was found to be negligible because a calculation *without* diffusion ended with the vortices at the same location as in Fig. 2.7, however some suspicious spikes showed up which were attributed to enstrophy equipartitioning. Again the TVD calculation exhibits a much larger dissipation of energy and potential enstrophy, as seen in Fig. 2.8, confirming the diffusiveness of this algorithm. Also note that the decrease in potential enstrophy is only twice the decrease of energy in the TVD run, while for Arakawa-Lamb this ratio is almost 4. In 2D-turbulence simulations it is usually tried to make this ratio as large as possible.

A TVD run with a higher resolution should give results closer to the results of the Arakawa-Lamb scheme. With a grid of 200×200 TVD gives similar positions for the dipoles at time=2.2 as shown in Fig. 2.7 for the Arakawa-Lamb calculation on a grid of 100×100. This shows that the Arakawa-Lamb scheme is much more efficient for these kind of problems.

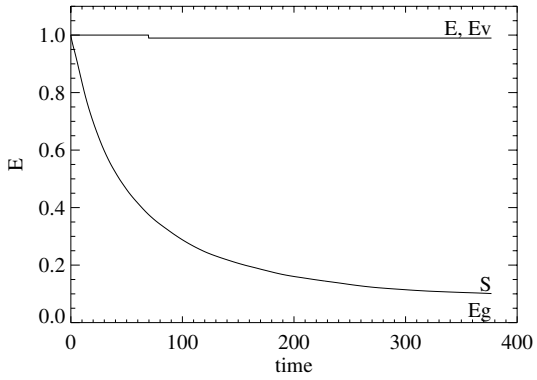

Figure 2.9: Evolution of total energy (E), potential enstrophy (S), vortical energy (Ev) and energy in the compressible modes (Eg) for decaying shallow-water turbulence. Notice that the latter energy is almost zero during the whole run so that the total energy is practically equal to the vortical energy. The data was normalized with the initial energy and potential enstrophy respectively.

2.4.3 Decaying shallow-water turbulence

In order to investigate how the Arakawa-Lamb scheme compares with a pseudo-spectral code, which is the prevailing method for 2D-turbulence simulations, the decaying shallow-water turbulence experiment of Farge and Sadourny (1989, FS) (their case BM) is repeated. In their article they distinguished two classes of eigenmodes: the divergent free vortical mode and two compressible modes with zero linearized potential vorticity. Their main findings were the existence of an inverse energy cascade in the vortical component of the flow, no energy exchange between the two classes of modes and the emergence of coherent vortices. In this paper all parameters and initial conditions are chosen as close as possible to the one described by FS, i.e. an initial Gaussian random field is evolved according to Eq. (2.1) up to time 377 on a square periodic domain on a grid of 256×256. The only exception is in the diffusion operator. FS used a ∇^{16} operator which is considered to be too high for a finite difference code, so here a ∇^8 operator is used instead.

The evolution of energy split into the two classes of eigenmodes (Ev: energy in vortical mode, Eg: energy in compressible modes), total energy and potential enstrophy is shown in Fig. 2.9 and is similar to Fig. 2a of FS. The potential enstrophy decreases rapidly by an order of magnitude, while the energy goes down with only 2 percent. This is typical for 2D-turbulence and in FS the decrease in energy was even less than 1 percent. In agreement with FS is the finding that the initial balanced state, which is a state in which $\nabla \cdot \vec{v} = \partial \nabla \cdot \vec{v} / \partial t = 0$, remains in balance equilibrium which is apparent because all the energy resides in the vortical component.

This is also clearly depicted in the energy spectra, Fig. 2.10, which is to be compared with Fig. 3a of FS. A power law spectrum with an index of -4 is seen in the

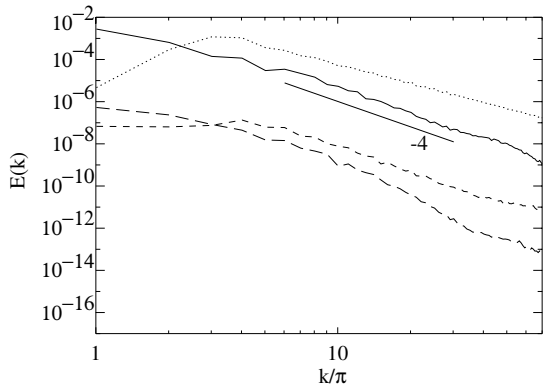

Figure 2.10: Spectra of vortical energy (dotted line at $t = 0$, solid line at $t = 377$) and compressible energy (short dashed line at $t = 0$, long dashed line at $t = 377$) on a log-log plot. A straight line with slope -4 is shown for reference.

vortical energy, which is commonly observed for 2D-turbulence. The energy spectrum of the compressible modes seems to have approximately the same slope, clearly different from FS where this spectrum is rather flat. This can partly be explained by the lower order of our diffusion operator. This moves the wavenumber at which the dissipation regime starts to lower values. Another part seems to be intrinsic to the algorithm.

Finally the spatial distribution of vorticity, potential vorticity, divergence of the velocity, stream function and height of free surface is shown in Fig. 2.11. A similar gray scale was used as in FS, their Fig. 6a. The vorticity and potential vorticity plots show the coherent vortices very clearly. The divergence is still randomly distributed, but comparison with FS indicates that the high wave number compressible components are more damped in this finite difference calculation than in the pseudo-spectral one. This same conclusion was already drawn from the spectra. The stream function and the height are again in agreement with FS.

For comparison reasons, a similar calculation was done with the TVD method of VAC with the same settings as in Sect. 2.4.2 The shade perspective representation of the vorticity is given in Fig. 2.12. The flow field is clearly very much affected by the relatively large intrinsic viscosity of this algorithm.

The overall conclusion is that the simulation of the vortical component with this finite difference scheme is quite good, the same qualitative conclusions can be drawn from this simulation as Farge and Sadourny did from theirs. However some prudence is called for if it comes to the high wave number compressible modes. They might be more damped than is desirable. This disadvantage should be contrasted with the advantage of a finite difference formulation which is more flexible in the sense that other non-Cartesian (but orthogonal) grids can easily be used with non-periodic boundary conditions.

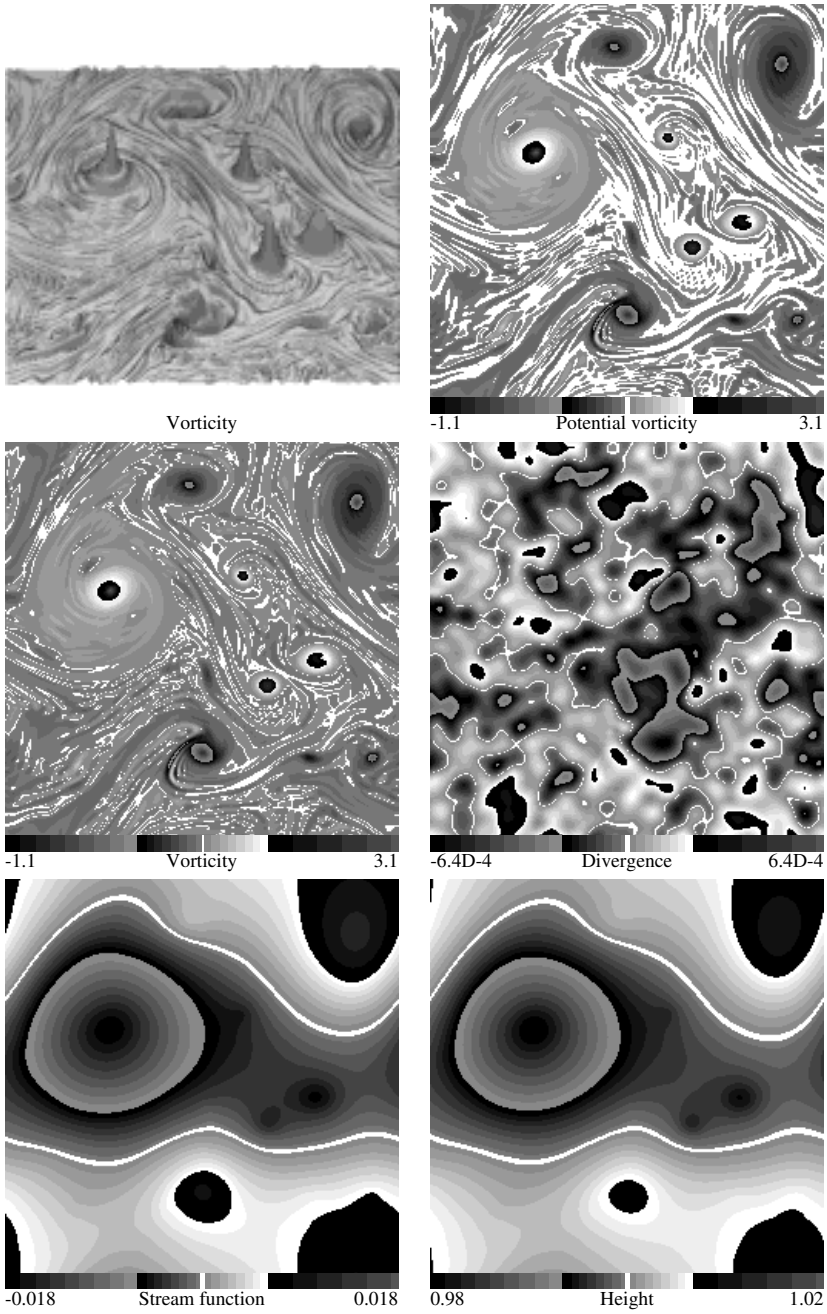

Figure 2.11: Spatial distribution of vorticity in shade perspective representation and potential vorticity, vorticity, divergence of velocity, stream function and free surface height in cartographic representation at time=377 of an initially Gaussian random field.

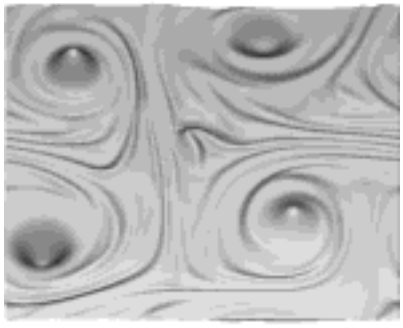

Figure 2.12: Shade perspective representation as in Fig. 2.11 of the vorticity for a TVD calculation.

2.4.4 A nonlinear instability in a quasi-Keplerian flow

This last test problem is astrophysically motivated and is related to stability issues in accretion disks (see also the introduction). Hydrodynamic stability of Keplerian flow has been a controversial point for a long time. However, at least one special type of instability seems very likely to develop in an accretion disk, the instability of sheared disturbances (Haynes, 1987). The mechanism of this instability is outlined here, for details consult the original publication.

Suppose there is a finite amplitude perturbation in the disk. For most disturbances the lines of constant potential vorticity will be distorted, for example as sketched in Fig. 2.13 on the left. The temporal development of this disturbance is governed by the advection equation for potential vorticity, Eq. (2.2). If the amplitude of the disturbance is not too large then the Keplerian flow dominates the advection. This deforms the disturbance as indicated in Fig. 2.13 on the right. Naturally the lines of constant potential vorticity bend over and develop a Z-shape. Rossby waves running along the diagonal of this Z-shape move to the left because the potential vorticity gradient is positive while on the horizontal branches they move to the right because of the negative potential vorticity gradient. As discussed in Sect. 2.4.1 for the shearing instability, this is a potentially unstable situation if the Rossby waves are fast enough to travel up against the shear (second stability criterion of Arnol'd). Since the phase speed of Rossby waves is proportional to the gradient in the potential vorticity and this quantity increases in time, in the end such fast Rossby waves will be possible. This instability can be prevented by viscosity, by limiting the maximum potential vorticity gradient achievable. Viscous effects for these kind of flow phenomena were discussed by Dubrulle and Zahn (1991).

To test the cylindrical grid and gravity, an initial condition was set up such that it was expected to show the behavior as described above. Similarly to Haynes, we

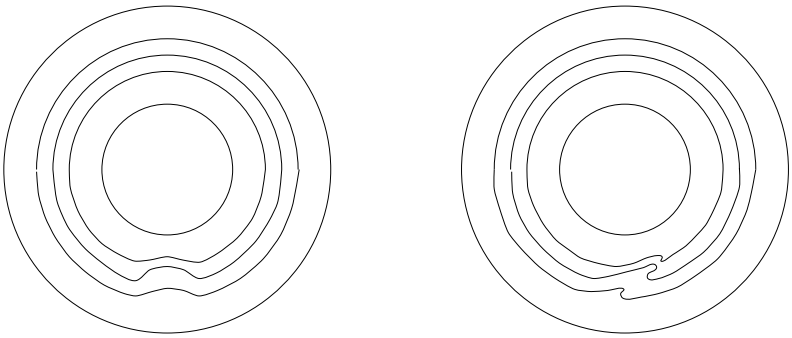

Figure 2.13: Sketch of the potential vorticity contours in a Keplerian rotating disk with a initial disturbance (left) and the same disturbance after a while (right). Because the potential vorticity is mainly advected with the Keplerian flow inflection points of potential vorticity form naturally.

save computer time by choosing an initial disturbance with an inflection point as depicted on the right panel of Fig. 2.13. Since the Keplerian shear $1.5\sqrt{GM/R^3}$ is much larger than typical potential vorticity gradients $0.75\sqrt{GM/R^5}$ and Arnol'd's second stability criterion should be violated, the initial disturbance is chosen to be much more stretched than that of Haynes. The disturbance takes the form of a tightly wound spiral as shown in Fig. 2.14 on the top left. The sheared disturbance is derived from the stream function:

$$\Psi = a_0 \frac{\cos(\kappa\phi + \lambda(R-r))}{\kappa^2+\lambda^2} \exp\left(-(R-r)^6\right),$$

where R is the average radial distance of the disturbance and we have chosen $\kappa = 1$ and $\lambda = 6.4\pi$. The extra exponential factor compared with Haynes was added because here reflective boundary conditions are used at the inner and outer edge of the disk at $0.75R$ and $1.25R$ respectively. The evolution in time is governed by Eq. (2.3) (where $\gamma = 1.4$ is used). Calculations are performed in a coordinate frame that rotates with the Keplerian speed at $r = R$. To obtain the non-dimensional parameters that determine the problem it is better to transform these equations to a shearing coordinate frame where Ω is a function of r and the complete Keplerian velocity is removed. The resulting non-dimensional parameters are: the *Rossby number* $\mathrm{R_o} = V/2\Omega L$ (and $1/2\Omega T$) where V, L and T are the typical velocity, length and time scale of the non-Keplerian component of motion respectively; the *Mach number* $\mathrm{M_a} = V/c_\mathrm{s}$; and the *ratio of the sound speed and the Keplerian velocity* $c_\mathrm{s}/v_\mathrm{kep} = c_\mathrm{s}/\sqrt{GM/R}$. Typical parameters used are: $c_\mathrm{s}/v_\mathrm{kep} = 0.1$, $\mathrm{M_a} = 0.006$ (based on the disturbance), and $\mathrm{R_o} = 0.002$. The grid is 128×128 and the diffusion time for one grid cell is typically 80 orbital periods. A small random perturbation starts up the instability, which can be seen in Fig. 2.14. We plot the potential vorticity after 9.6, 11.2 and 15.9 orbits around the compact object. The potential vorticity is broken up into patches of comparable width to the original spiral. This instability is not expected to drive turbulence because it

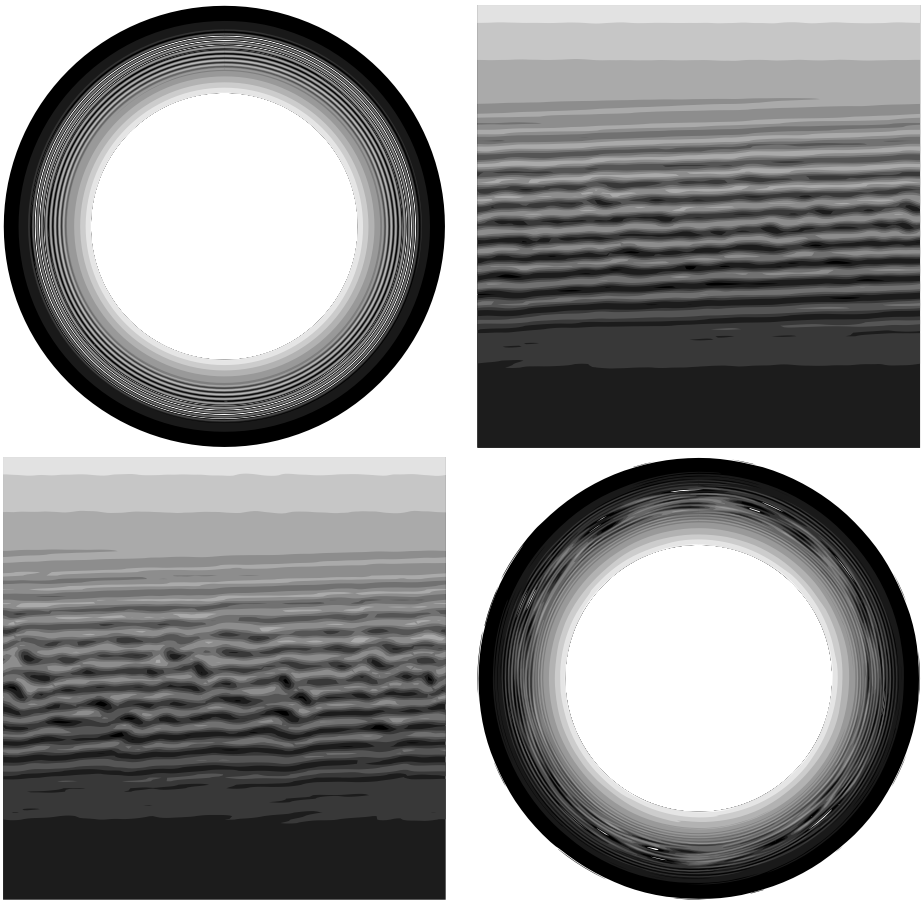

Figure 2.14: The potential vorticity of the initial condition and after 9.6, 11.2 and 15.9 orbital periods for the sheared disturbance instability in a quasi-Keplerian rotating disk. To show the instability more clearly, the data at 9.6 and 11.2 orbital periods is plotted as a square with angle along the horizontal and radius along the vertical axis.

seems that it does not extract energy from the Keplerian flow, only from the sheared disturbance. In this sense the results are in agreement with Balbus *et al*. (1996).

Shocks were not observed in these simulations although at the boundaries compressible phenomena developed that hardly showed up in the potential vorticity plots. Possible influence of the over-reflective instability (Narayan *et al.*, 1987) was checked by repeating the simulation with a kind of absorbing boundary condition (Martinsen and Engedahl, 1987). The potential vorticity evolution was found to be very similar to the experiment with reflective boundaries indicating that over-reflection is not very important in this experiment on these timescales.

2.5 Conclusion

The main goal of this work is to present a numerical algorithm which is suited to investigate vortices in thin polytropic accretion disks, in particular to answer the question why large 2D-vortices have not been found in studies of disks so far (e.g. Różyczka and Spruit, 1993; Godon, 1997) and Brandenburg *et al*. (1995) even mention this explicitly. The algorithm is basically a shallow-water scheme from geophysical fluid dynamics (Arakawa and Lamb, 1981). Because of the similarity of the shallow-water equations with the 2D-polytropic gas equations, it can also be used to investigate thin polytropic accretion disks.

The tests performed demonstrate that the algorithm is well suited to describe instabilities of the shearing type also when they occur in an accretion disk in the form of instability of sheared disturbances (Haynes, 1987). In the latter case the instability does not seem to draw its energy from the Keplerian rotation but from the initial disturbance creating an inflection point. This is in agreement with the results from Balbus *et al*. (1996). Why these authors did not observe this phenomena can only be guessed. They may not have waited long enough for the second stability criterion of Arnol'd to be violated or their Reynolds number may have been too low.

The essential aspects of 2D-turbulence are also simulated correctly with this algorithm. The inverse energy cascade is well represented and long lived coherent structures are seen to form out of random initial conditions as they should. This algorithm combines the low diffusivity needed for this kind of work with the flexibility of a finite difference formulation. Therefore, it is expected to be well suited to study vortices in accretion disks around compact objects and their influence on transport. Another interesting application is to study the role of vortices in planet formation in protoplanetary disks (Tanga *et al.*, 1996). The main disadvantage of this algorithm is that it results in oscillations around discontinuities such as shocks. If these occur, shock-capturing methods such as TVD are preferable.

Acknowledgements. MDN thanks prof. J. Kuijpers and prof. J.T.F. Zimmerman for their help and guidance and prof. M.E. McIntyre for drawing his attention to P.H. Haynes' work. The Versatile Advection Code was written by GT while funded by the Dutch Science Foundation (NWO). He is currently supported by the post doctoral fellowship D 25519 of the Hungarian Science Foundation (OTKA). We thank the anonymous referee for his/her detailed review which helped us in improving this article.

Chapter 3

Two-Dimensional Turbulence and Accretion Disks

Abstract. It has been suggested that two-dimensional turbulence is operating in thin astrophysical accretion disks and would give rise to long-lived vortices. This hypothesis is investigated by studying the development of 2D-turbulence under some of the typical circumstances that occur in thin non-selfgravitating accretion disks. This is done with what is in essence a shallow-water code. It is found that the influence of Coriolis forces is limited but that the shearing flow alters 2D-turbulence significantly. Only prograde vortices are expected in an accretion disk and, more over, they should be strong enough to withstand the shear. Also, the maximum radial extend of the vortices is probably limited to the thickness of the disk. This implies that the flow geometry is not flat and the Rossby number not small so that a 2D-treatment of the fluid dynamics is formally only correct if the flow is in hydrostatic equilibrium in the direction perpendicular to the disk. Therefore it is questionable whether 2D-vortices really abound in accretion disks, and our results suggest why many numerical simulations of accretion disks do not show long-lived 2D-vortices. However, the existence of such vortices is not ruled out.

M.D. Nauta
submitted to *Geophysical and Astrophysical Fluid Dynamics*

3.1 Introduction

From a fluid dynamical point of view, one of the most interesting astrophysical objects is an accretion disk. It comes in different flavors, but the standard is a plasma disk around a compact star such as a white dwarf, neutron star, or black hole. Another manifestation is a gaseous and dusty disk around (proto-) stars that have just formed. Our solar system is thought to be a remnant of such a protostellar disk. These disks derive their name from transport of material through the disk onto the central object: they accrete material. Accretion rates have been determined observationally (e.g. Rutten *et al.*, 1992) and were found to be much larger than can be explained by simple transport processes such as molecular viscosity. That is why it was suggested that accretion disks are turbulent (e.g. Shakura and Sunyaev, 1973). Lately, most research concentrates on magnetohydrodynamically (MHD) driven turbulence. For a recent review of accretion disks see Papaloizou and Lin (1995) and Lin and Papaloizou (1996).

A special version of turbulence, namely two-dimensional hydrodynamic turbulence, was proposed to be active in thin accretion disks because such disks are thin and rapidly rotating (Dubrulle and Valdettaro, 1992). Two-dimensional turbulence is characterized by an inverse energy cascade (Kraichnan and Montgomery, 1980) and the formation of coherent structures or vortices (McWilliams, 1984) (Sect. 3.3), and it is invoked to explain certain phenomena in planetary atmospheres and oceans, e.g. the robustness and persistence of Jovian vortices (Dowling, 1995). Similarly, the existence of large-scale vortices has also been suggested in thin accretion disks (Abramowicz *et al.*, 1992; Kuijpers, 1995; Adams and Watkins, 1995). Unfortunately, lack of spatial resolution prohibits direct observational verification of this hypothesis.

The above mentioned characteristics of 2D-turbulence apply to an isotropic incompressible flow. For many 2D-flows in nature these assumptions do not hold. Violation of these assumptions can lead to different phenomena. For example from Geophysical Fluid Dynamics (GFD) it is known that variation of the Coriolis force with latitude (the β-effect) introduces an anisotropy and leads to the growth of longitudinally elongated structures (the Rhines effect; Rhines, 1975). Also in an accretion disk the assumption of an isotropic incompressible 2D-flow is clearly not justified as the flow pattern is highly directive and (some) motions are highly supersonic. Even if gross simplifications are made - such as assuming 2D-flow (because of stratification or the Taylor-Proudmann theorem) and using a polytropic relation instead of an energy equation - the character of 2D-turbulence may still differ from the standard picture by, for example, the shear of the Keplerian motion. It is the aim of this paper to investigate the influence on 2D-turbulence of some of the typical circumstances in an accretion disk. The main question I would like to answer is why only so few studies (only Bracco *et al.*, 1998 to the author's knowledge) do find vortices in their (2D-) simulations of accretion disks, whereas it is claimed that vortices are a robust feature of 2D-flow. For this purpose, the 2D-polytropic gas equations that are often used in theoretical studies of disk dynamics, (e.g. Goldreich *et al.*, 1986), are solved with what is in essence a shallow-water code (Arakawa and Lamb, 1981). The equations

and numerical procedure are briefly outlined in Sect. 3.2. A thorough discussion and testing of the code was presented in a previous paper (Nauta and Tóth, 1998). Ordinary 2D-turbulence is discussed in Sect. 3.3, which is mainly written for those unfamiliar with the subject. It serves as the standard to which the other simulations are compared. The influence of Coriolis forces is investigated in Sect. 3.4. Next, a background shear flow is introduced in Sect. 3.5. The paper ends with a discussion on the implications of the observed phenomena for an accretion disk.

3.2 Equations

Two-dimensional turbulence is usually (e.g. McWilliams, 1984; Santangelo *et al.*, 1989; McWilliams, 1990) studied by numerically solving the vorticity equation (the curl of the momentum equation):

$$\frac{\partial \omega}{\partial t} + \nabla \cdot (\omega \vec{v}) = \mathrm{Dif}, \tag{3.1}$$

on a square periodic grid for a given initial condition. All variables have their usual meaning: $\omega = \nabla \times \vec{v}$ is the vorticity and Dif stands for some diffusion process. In case of molecular diffusion Eq. (3.1) is the 2D incompressible Navier-Stokes equation. However, if Dif represents the influence on the resolved scales of sub-grid scale motions, then it is not clear that Dif is described by a Laplacian operator, and often a higher order differential operator is chosen to simulate flow with an effectively higher Reynolds number. This is called hyperviscosity.

In principle Eq. (3.1) could be used to study the flow in an accretion disk. However, to arrive at this equation so many approximations have to be made that possibly significant physical effects (e.g. compressibility) could have been neglected. At the opposite end are the 3D MHD equations with self-gravity and radiative transfer. They are highly relevant for an accretion disk, but they are also extremely complicated to solve and it is hard to unravel the different physical processes going on at the same time from their solutions. Here an "intermediate" approach is chosen, the 2D-polytropic gas equations:

$$\begin{aligned} \frac{\partial \Sigma}{\partial t} + \nabla \cdot \Sigma \vec{v} &= \mathrm{Dif}, \\ \frac{\partial \vec{v}}{\partial t} + \vec{v} \cdot \nabla \vec{v} + 2\Omega \hat{z} \times \vec{v} &= -\frac{1}{\Sigma} \nabla P + \nabla \Phi_{\mathrm{G}} + \mathrm{Dif}, \\ P &= K \Sigma^{\gamma}. \end{aligned} \tag{3.2}$$

Here Σ is the surface density, P the height integrated pressure and $\Phi_{\mathrm{G}} = GM/r + \Omega^2 r^2/2$ describes the effective gravity of the central compact object. This simplified set of equations describes an accretion disk in a frame rotating with fixed angular rotation speed $\Omega\hat{z}$ (and they have been used before by for example Goldreich *et al.*, 1986). The simplifications implicit to the 2D-polytropic gas equations consist of neglecting magnetic fields, radiative transfer and self-gravity of the gas and integrat-

ing over the vertical thickness of the disk. To eliminate baroclinic effects, a polytropic equation of state between surface density Σ and height integrated pressure P is used. It short-circuits the energy equation so that only the continuity and momentum equations need to be solved. If the adiabatic index, $\gamma = 2$, is chosen, then the 2D-polytropic gas equations are identical to the shallow-water equations which have been used before in 2D-turbulence simulations (e.g. Cho and Polvani, 1996). Now the surface density is to be interpreted as the height of the free surface. The shallow-water equations are often considered to form the most simple dynamical model of a planetary atmosphere or ocean. Similarly, the 2D-polytropic non-selfgravitating gas equations can be considered as the most simple model of an accretion disk.

Equations (3.2) are written in a rotating coordinate system. This introduces the Coriolis acceleration and centrifugal force. A solution in which the fluid motion is circular and determined by a balance of centrifugal force with gravity of the central compact object, causing the velocity to be Keplerian, is:

$$v_{\rm k} = \left(\frac{GM}{r}\right)^{1/2} - \Omega r,$$

where $\Omega = (GM/R^3)^{1/2}$ and R is a fixed reference value. A velocity field superposed on this flow is required to explain the large radial transport of mass and angular momentum observed in astrophysical accretion disks.

For a planetary atmosphere or ocean, the fluid layer on which the turbulence is superimposed is a thin layer in solid body rotation on the surface of a sphere. The influence of these conditions on 2D-turbulence was investigated by Cho and Polvani (1996a). For an accretion disk the turbulence is superimposed on a thin layer in Keplerian rotation. It follows that at least two conditions may change the character of 2D-turbulence from its standard behavior: rotation of the coordinate frame (also studied by Polvani *et al*. (1994) and others) and shear of the Keplerian motion. The influence of these is studied in an elementary way: I take a 2D-turbulence simulation and add only Coriolis forces (this is the influence of a rotating coordinate frame) in Sect. 3.4, and in another simulation I add a uniform shear flow in Sect. 3.5. The application to accretion disks is the subject of Sect. 3.6.

3.2.1 Technicalities

The equations are made dimensionless by introducing a typical length (L), velocity (V), time (T) and density (the unperturbed value is set to unity so that the total density is $1 + \Sigma$) scales. The resulting non-dimensional numbers are discussed at the initial conditions (Froude or Mach number ($\mathrm{M_a}$) and the scaling of the time) and at the sections where they are first introduced (Burger number (B) in Sect. 3.4, non-dimensional shear in Sect. 3.5). Simulations were performed on a square Cartesian grid of $[-1,1] \times [-1,1]$ with 256^2 grid points. The algorithm used is in essence a shallow-water code (Arakawa and Lamb, 1981) and, because of the close similarity between the shallow-water equations and the 2D-polytropic gas equations, can also be used for the latter. The reason for not choosing a shock capturing scheme is

that the present algorithm allows for higher Reynolds number simulations (Nauta and Tóth, 1998). It also conserves potential enstrophy (average of vorticity squared divided by free surface height) for ideal flow. Two periodic and two free-slip reflective boundaries were used. As hyperviscosity a $\nu\nabla^8\cdot$ operator is used on the right hand side of all three differential equations (3.2). The diffusion is such that a wave of wavelength four grid cells is suppressed in approximately one initial eddy turnover time.

In the analysis of turbulence, spectral information plays an important role; especially the analysis of energy spectra has a long tradition. Two technical points regarding the calculation of spectra merit closed inspection.

The kinetic plus internal energy in the polytropic 2D-gas equations is:

$$E = \iint \left(\frac{1}{2}(1+\Sigma)\left|\vec{v}\right|^2 + \frac{1}{\mathrm{M_a^2}} \frac{1}{\gamma(\gamma-1)}(1+\Sigma)^\gamma \right) d^2\vec{x}.$$

Since the energy is not a quadratic function of the flow variables it is far from clear how energy spectra should be constructed for this case. Even for shallow-water ($\gamma = 2$) the kinetic part of the energy is not quadratic. Previously this was solved by using the kinetic energy per unit mass (Polvani *et al.*, 1994) or a linearization procedure (Farge and Sadourny, 1989). For the spectra presented here the difference between the two methods is small. The spectra shown are calculated following the approach of Farge and Sadourny. They assumed small perturbations (small Froude number ($\mathrm{M_a}$) and small deviations in free surface height) and linearized the shallow-water equations (so $\gamma = 2$). For this new set of equations the energy is a quadratic quantity:

$$E' = \frac{1}{2} \iint \left(\left|\vec{v}\right|^2 + \frac{1}{\mathrm{M_a^2}}\Sigma^2 \right) d^2\vec{x},$$

from which a spectrum can be calculated. Because of two quadratic conserved quantities, the energy and the potential enstrophy, the flow field can be split into three distinct eigenmodes which are called: one potentio-vortical and two inertio-gravitational modes. The potentio-vortical mode contains all the potential vorticity (the absolute vorticity divided by the surface density) and is incompressible. The two inertio-gravitational modes are compressible and do not contain any potential vorticity. As these eigenmodes facilitate the analysis and the results did not depend very strongly on γ all simulations presented in this paper are performed with the shallow-water equations unless stated otherwise. As a result, the nomenclature is adjusted: when the shallow-water equations are used terms like surface density and Mach number are replaced with their equivalent terms: free surface height and Froude number respectively.

There is another problem in the construction of the energy spectra. Flow variables are not periodic in the direction perpendicular to the closed boundaries. Most notably the stream function can be different on both closed boundaries (which implies that there is a net flow through the periodic boundaries). When Fourier transformed this jump results in significant power in the high wavenumber bins. To remove this artifact the stream function (ψ) and velocity potential (χ) ($\vec{v} = \hat{z} \times \nabla\psi + \nabla\chi$) are

multiplied with a function that is flat in the middle and decreases smoothly to zero (as $(1-\cos(x))/2, 0 \le x \le \pi$) in the 20 grid cells next to the closed boundaries. The modified stream function and velocity potential are used to calculate spectra, from Farge and Sadourny (1989):

$$\begin{aligned} E'_{\mathrm{v}}(k_n) &= \frac{1}{2}\Sigma_{k_n \le |\vec{k}| < k_{n+1}} \frac{\left| k^2\psi(\vec{k}) + \phi(\vec{k})/(\mathrm{M_a B}^{1/2}) \right|^2}{1/\mathrm{B} + k^2}, \\ E'_{\mathrm{g}}(k_n) &= \frac{1}{2}\Sigma_{k_n \le |\vec{k}| < k_{n+1}} k^2 \left(|\chi|^2 + \frac{\left| \psi(\vec{k})/\mathrm{B}^{1/2} - \phi(\vec{k})/\mathrm{M_a} \right|^2}{1/\mathrm{B} + k^2} \right), \end{aligned}$$

where $\vec{k}$ is the wave vector, ϕ the free surface height.

The initial condition is constructed with the help of a stream function which is defined in Fourier space by the relation:

$$E(k) = E'_{\mathrm{v}}(k) = 2\pi k \frac{1}{2}\left(\frac{1}{\mathrm{B}} + k^2\right)\left|\psi(\vec{k})\right|^2 \propto \frac{k}{1+(k/k_0)^4},$$

which has the same spectral energy distribution as in McWilliams (1984). The phases of the Fourier components of the stream function are chosen randomly. By choosing k_0 relatively large ($k_0 = 10\pi$ resulting in 10 waves on the simulation domain) a clear inverse energy cascade can be seen. The amplitude of the stream function determines the amplitude of the velocity field or the Froude number. Here a maximum Froude number of approximately 0.1 is used which results in an rms value of 0.036 for the given initial spectrum. The initial velocity potential is chosen zero because the usual 2D-turbulence simulations are incompressible and here we want to add extra elements one by one. The initial distribution of free surface height is chosen such that in the subsequent evolution the amplitude of the excited inertio-gravitational waves is small. The free surface height distribution that satisfies this condition is called a balanced equilibrium, and to calculate it the simple balancing procedure of Farge and Sadourny (1989) is used, though more elaborate balancing procedures are known (Polvani *et al.*, 1994). The initial enstrophy S_0 (spatial average of vorticity squared) determines the "initial eddy turnover time" $t_{\mathrm{eddy}} = T = 2\pi/(S_0)^{1/2}$, the time scale that is used throughout this article.

3.3 Standard two-dimensional turbulence

If fluid motion is restricted to two dimensions then the vorticity vector is directed perpendicular to the flow. All vortex tubes are parallel which implies that they do not stretch each other. In this way the process responsible for transfer of energy to small length scales in 3D-turbulence is absent from 2D-flow. It is a well known result (e.g. Pedlosky, 1987) that in 2D-incompressible turbulence the energy goes to large length scales or small wave numbers. This process is called the inverse

energy cascade. Numerical simulations (e.g. McWilliams, 1984) show that during the inverse cascade coherent structures or vortices form. This is nowadays considered the most characteristic process of 2D-incompressible turbulent flows.

It was shown (Farge and Sadourny, 1989) that 2D-turbulence in shallow-water shares many of its characteristics with 2D-incompressible turbulence. Shallow-water differs from 2D-incompressible flow in that there is a free surface. Local changes in the thickness of the fluid layer introduce 2D-compressibility ($\partial v_x/\partial x + \partial v_y/\partial y = -\partial v_z/\partial z \neq 0$). In this section a low Froude number shallow-water simulation is used to demonstrate the characteristics of 2D-turbulence. Eq. (3.2) is solved without Coriolis acceleration ($B = \infty$) and effective gravitational potential. The results serve as "the standard" reference material for the simulations in the following sections.

The formation of coherent structures is clearly seen in potential vorticity or vortensity ($\nabla \times \vec{v}/\Sigma$), Fig. 3.1. The initial distribution looks very random. Initially the potential vorticity is stretched, creating thin vorticity structures. This corresponds to the enstrophy cascade that transfers enstrophy towards the dissipation regime at

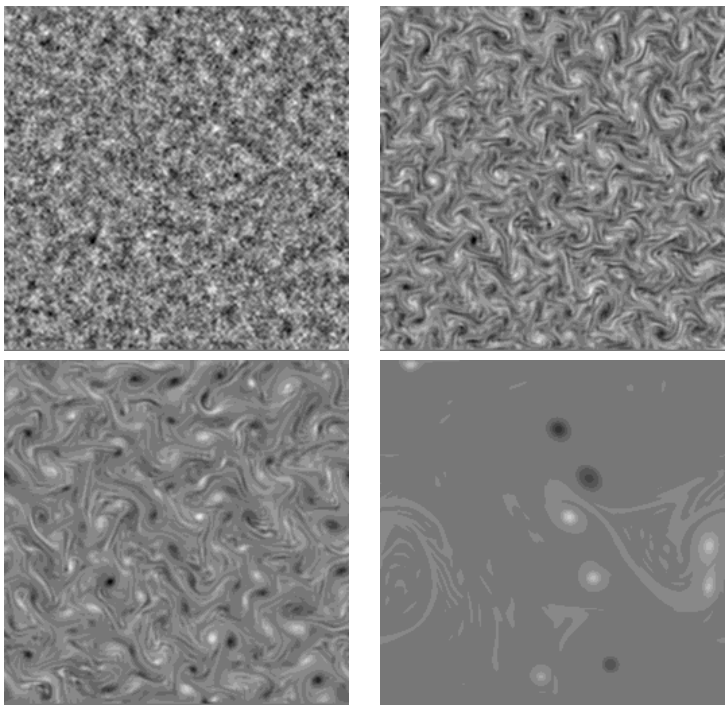

Figure 3.1: Potential vorticity distribution at four different times (left to right, top to bottom). The initial potential vorticity is distributed randomly. After 0.75 eddy turnover times some of the vorticity is elongated into thin structures transferring enstrophy towards high wave numbers. At 2.8 turnover times the coherent structures are clearly visible. A small number of them is left after approximately 120 eddy turnover times.

high wave numbers. A bit later part of the vorticity rolls up to form vortices. These vortices interact with each other in the form of (partial) mergers and (partial) strainings. Merging only occurs among vortices of the same sign and is often interpreted as manifestation of the inverse energy cascade in configuration space, creating large scale structures. After many mergers only a limited number of vortices remain. This is already the case after a couple of eddy turnover times. Eventually these vortices interact with each other to result in two vortices of opposite sign (Matthaeus *et al.*, 1991), but this takes longer than the time over which the present simulation was evolved.

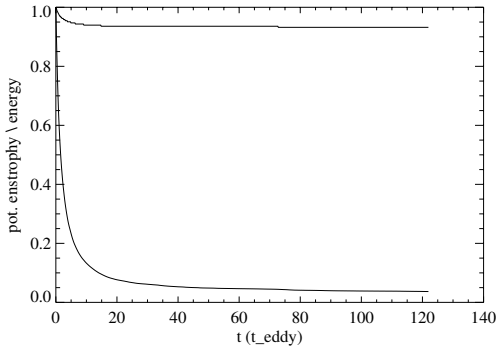

Figure 3.2: The total energy (upper curve) and potential enstrophy (lower curve) as a function of time. The data are normalized with their initial values. The time t_{eddy} is defined in Sect. 3.2.1.

Characteristic for 2D-turbulence is also the evolution of energy and potential enstrophy, Fig. 3.2. Because of the inverse energy cascade little energy flows into the dissipation regime so that the total energy is almost conserved. The energy plotted is the total energy which includes the energy in the inertio-gravitational components which can cascade in the "ordinary" direction and be dissipated by diffusion. However, because of the initially balanced state, the contribution of this energy to the total is negligible and the total energy is almost fully comprised of potentio-vortical energy. On the other hand, potential enstrophy does cascade in the normal direction and is dissipated. A considerable decrease in potential enstrophy is observed. The enstrophy decrease slows down as soon as vortices form, because non-linear enstrophy transfer is prohibited inside vortices (Babiano *et al.*, 1987; Benzi *et al.*, 1986).

The inverse energy cascade can be observed in the spectrum, Fig. 3.3. Plotted is the energy in the potentio-vortical component. The initial energy spectrum peaks at a wavenumber of $3^{-1/4}k_0 \approx 7.6\pi$. At the end of the simulation the energy peaks at the lowest possible wavenumber π. Also, from the shape of the spectrum it is clear that the energy at lower wavenumbers grows at the cost of the energy at higher wave numbers. The slope of the spectrum is approximately -4 which deviates from what a Kolmogoroff style of analysis would give (-3). This has been attributed to the coherent vortices (e.g. Benzi *et al.*, 1987) and to intermittency (localization of phenomena in space and/or time).

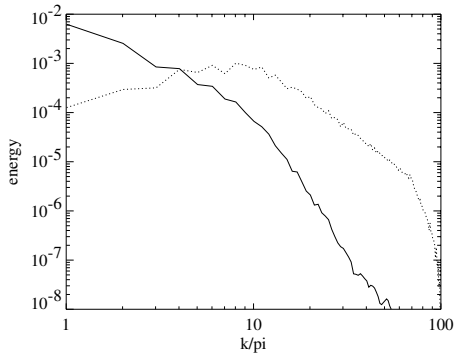

Figure 3.3: The energy spectra at the initial time (dotted) and at the end of the simulation, $t \approx 120\, t_{\mathrm{eddy}}$ (solid).

The intermittency of the turbulence can also be measured in real space with the kurtosis of the relative vorticity ($\nabla \times \vec{v}$). The probability density function of the relative vorticity becomes a strongly peaked function around zero, while there are tails to positive and negative relative vorticities due to the vorticity in the coherent structures that hardly decays. So the distribution deviates strongly from Gaussian and it is this quality that is measured by the kurtosis (Press *et al.*, 1992). It increases with time, as shown in Fig. 3.4.

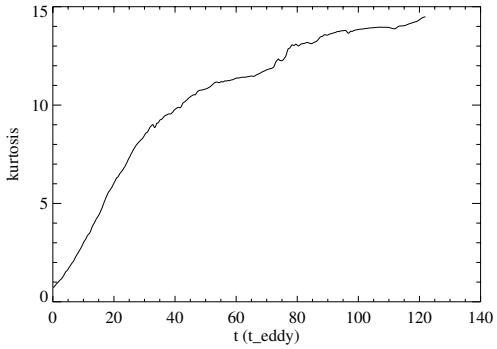

Figure 3.4: The kurtosis of relative vorticity as a function of time.

Since vortices appear to form the elementary building blocks of 2D-turbulence, their statistical properties were determined as a function of time (McWilliams, 1990). Here this is done as well but with a different vortex recognition algorithm, see the Appendix. Fig. 3.5 shows the number of vortices as a function of time. Due to mergers and hyperviscosity the number of vortices drops as a power law with exponent -0.70, which is in agreement with McWilliams (1990). Power laws for other observables were predicted and claimed to be found by Carnevale *et al*. (1991). The average vortex radius, circulation, the enstrophy and vorticity kurtosis should exhibit

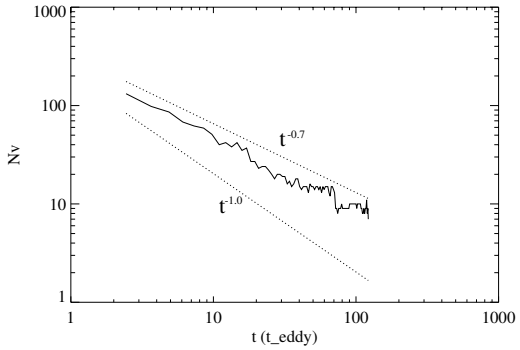

Figure 3.5: The number of vortices as a function of time.

power law behavior in time. This follows from combining the observed power law in the number of vortices as a function of time, a dimensional analysis and conservation of energy and peak vorticity (of the vortices). The theory was heavily criticized (Dritschel, 1993) and in the present simulations the predicted power law exponents could not be verified.

Summarizing, the low Froude number shallow-water simulation is well equipped to demonstrate the formation of coherent structures, the intermittency and the cascading in energy and enstrophy such as are typical for 2D-turbulence.

3.4 Two-dimensional turbulence and Coriolis forces

Two-dimensional turbulence as it was studied in the previous section forms an idealized paradigm for large-scale geophysical turbulence. It is easy to make it a bit more realistic by adding solid body rotation, so that Coriolis forces should be taken into account (which also play a role in an accretion disk). Eq. (3.2) is solved with Coriolis acceleration but without effective gravitational potential. The f-plane approximation is made implying that variation of the Coriolis parameter or planetary vorticity $f = 2\Omega$ with a latitude coordinate is *not* considered. Influence of rotation on 2D-turbulence is expected to become visible as the Coriolis parameter is increased because the force balance within vortices changes from cyclostrophic (pressure gradients balancing centrifugal forces) to geostrophic (pressure gradients balancing Coriolis forces).

More specifically, rotation of the coordinate frame introduces a new time scale $1/f$ and, when combined with the gravity wave speed (c_s), a new intrinsic length scale:

$$L_D = \frac{c_s}{f},$$

called the Rossby radius of deformation. Traditionally this length scale is interpreted as the scale at which the Coriolis force becomes of the same order of magnitude as the pressure gradient. Perhaps a better interpretation follows from an expansion of

the (dimensional) potential vorticity in small parameters:

$$\frac{f + \nabla \times \vec{v}}{\Sigma} \approx \frac{f}{\Sigma_0} + \frac{\nabla \times \vec{v}}{\Sigma_0} - \frac{f\Sigma_1}{\Sigma_0^2}.$$

The third term on the rhs (which describes the contribution of vortex stretching to the potential vorticity) is of the same order of magnitude as the second (which describes the contribution of relative vorticity to the potential vorticity) if the length scale of the phenomenon is of the order of the Rossby deformation radius (Pedlosky, 1987, p.92). (In this scale analysis geostrophic equilibrium is used.) The square ratio of the Rossby deformation radius to the typical length scale of the flow (L) is called the Burger number:

$$\mathrm{B} \equiv \left(\frac{L_\mathrm{D}}{L}\right)^2.$$

To investigate the influence of the Coriolis force (or, equivalently, a finite Rossby deformation radius or finite Burger number), several simulations were done with different values for the Coriolis parameter f. The initial energy spectra were the same for all simulations. Similar experiments have been done before by Farge and Sadourny (1989) and especially the work of Polvani *et al*. (1994) is valuable. This topic has also been investigated with a reduced set of equations (Cushman-Roisin and Tang, 1990; Larichev and McWilliams, 1991). The main findings are illustrated on the basis of my simulation with Rossby deformation radius 0.031 or Burger number 0.16, where the energy centroid of the initial energy spectrum was used to get a typical length scale. This small Burger number simulation is compared with the standard which has a Burger number of infinity. Other experiments were done at Burger numbers of 0.64 and 10.2.

Comparison of the potential vorticity for the small Burger number simulation after approximately 120 initial eddy turnover times, Fig. 3.6, with that of the standard, Fig. 3.1, shows that there are many more vortices in the small Burger number

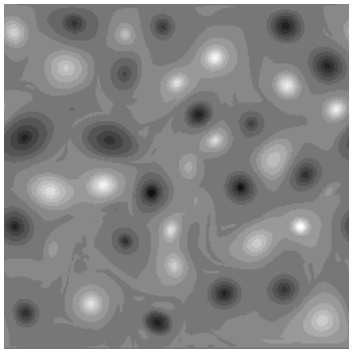

Figure 3.6: Potential vorticity distribution of a simulation with small Burger number (0.16) after approximately 120 initial eddy turnover times.

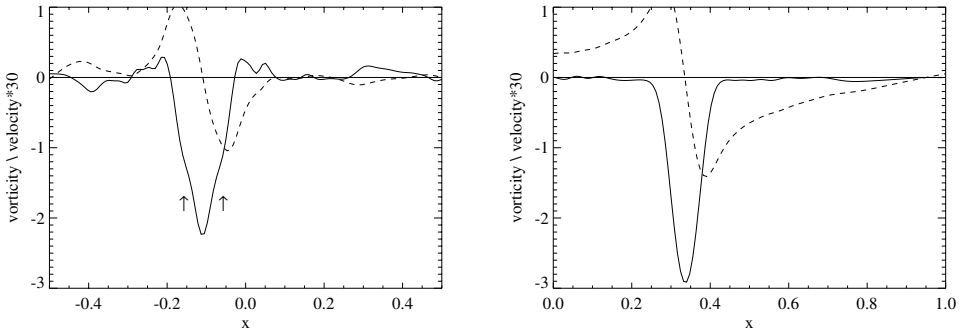

Figure 3.7: Cross section through two vortices. On the left, a vortex larger than its Rossby deformation radius, on the right, from the standard simulation with infinite deformation radius. Relative vorticity is indicated by the solid line, velocity by the dashed line, the arrows are discussed further down the text. The difference in profile is very clear: the vortex on the left is shielded as it is surrounded by a ring of opposite vorticity so that the velocity drops off rapidly, while the vortex on the right is surrounded by potential flow.

case. The reason becomes clear in a movie. The vortices are seen to be much more stationary and move around far less at small Burger number, as was also reported by Polvani *et al*. (1994). This can be understood from the typical profile of a vortex. In Fig. 3.7, cross sections through an isolated vortex from both simulations are juxtaposed. It is observed that at small Burger number the negative vorticity core is surrounded by a ring of opposite vorticity while this is not the case at infinite deformation radius. A possible reason for this shielding at low Burger number is that the velocity and density are continuous on the boundary of the vortex, where the potential vorticity drops. As a result, outside the vortex the density deviates from the background density and at small Burger number this contributes significantly to the potential vorticity. To cancel such a contribution, the vortex creates a ring of relative vorticity of opposite sign at its edge. The velocity induced by the vortex in the standard simulation typically drops as $1/r$ at large radii, but decreases much more rapidly if the vortex is larger than the Rossby deformation radius. This implies that, at small Burger number, the vortex only interacts with its immediate neighbors and that the velocities with which the vortices propel each other are reduced. This results in fewer encounters among vortices and less mergers, Fig. 3.6.

The potential vorticity distribution in Fig. 3.6 suggests that the inverse energy cascade is slowed down at small Burger numbers. This can be quantified by measuring the number of vortices as a function of time. In the standard simulation this number drops as a power law with index -0.7, Fig. 3.5, while here the index is -0.41. The reduced cascade is corroborated by a slower decay of potential vorticity and a slower growth of the vorticity kurtosis (not shown). The slow down of the inverse energy cascade is also very clear from the spectral evolution, Fig. 3.8. The peak in the spectral distribution only shifts from 7.6π to 4π during the time interval studied, while in standard decaying 2D-turbulence it is at the lowest wavenumber where

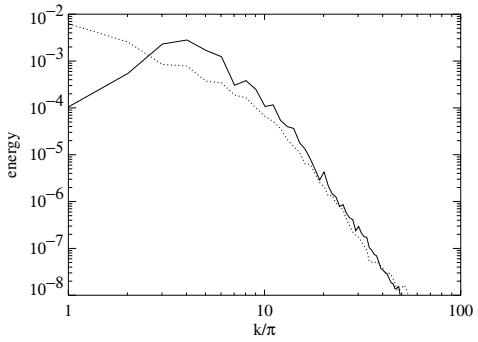

Figure 3.8: The energy spectrum of the potentio-vortical component after approximately 120 eddy turnover times. The dotted line indicates the standard.

most of the energy is contained.

The slowing down of the inverse energy cascade raises a question: Is there an upper limit to the size of the vortices that can form? The vortex size is often related to the peak in the spectral energy distribution (Polvani *et al.*, 1994) and the peak position almost comes to a standstill. The existing literature is rather unclear on this point. That is why the vortices were identified by an algorithm (see the Appendix) and their radii measured, Fig. 3.9. The measurements show that the largest vortices grow to several times the Rossby deformation radius and even the average radius gets larger than this value. So I don't find that the Rossby deformation radius sets an upper limit to the size of the vortices. The simulations at other Burger number indicate

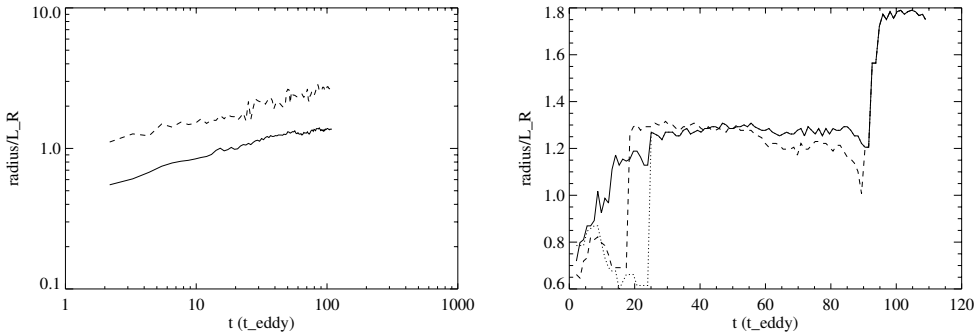

Figure 3.9: On the left, the average vortex radius (solid) and the radius of the largest vortex (dashed), both expressed in the number of deformation radii, as a function of time. On the right, the vortex radius of a particular vortex. It undergoes several mergers, at t=25 it merges with the vortex indicated with the dotted line and at t=90 with that indicated with the dashed line. During merging the vortex radius can substantially increase, but without mergers the radius hardly changes.

that the physical growth rate of the vortex radius depends little on this parameter. That the radial growth is more than just viscous widening, follows from tracking the behavior of one particular vortex which undergoes several merger events, Fig. 3.9. It is observed that the vortex radius mainly increases due to merging with other vortices. If there is no merger ($25 < t < 90$), then the radius increases (the solid line) or decreases (the dashed line) only a little bit, indicating that during these phases viscosity is not very important in determining the vortex radius. It should also be noted that the radii before and after merging imply that areas of the vortices add up (for this particular merger). This is contrary to what is supposed to occur in 2D incompressible turbulence where $R^4_{\text{1before}} + R^4_{\text{2before}} = R^4_{\text{after}}$ (Carnevale *et al.*, 1991). Also the fact that the average vortex radius growth rate is independent of Burger number indicates that at lower Burger number, when there are fewer mergers, the growth of the radius per merger is larger. This was also noted by Waugh (1992) in contour dynamics simulations of the merging of two quasi-geostrophic vortices.

These are not the only indications that the merging process is different at small Burger number. The vorticity profile of a typical vortex has already been partly discussed in Fig. 3.7, where the emphasis was on shielding. But the vortex core itself is also different: at small Burger number, there is a kink halfway the vorticity core, which is indicated by arrows in Fig. 3.7. A lot of vortices have a similar kink. One of the most extreme examples is shown in Fig. 3.10. The large negative vortices clearly exhibit strange kinks while the small positive vortex is fairly regular. It turns out that the kinks are a very persistent phenomena and are not the result of a recent merger. It looks as if it results from merging of a small intense and a large weak vortex many turnover times ago. Apparently, after the merger, there is little redistribution of vorticity if the vortex is larger than the Rossby deformation radius. As a result, large vortices look less robust and they have shapes that deviate considerably from a circular monopolar vortex which was also noted by others (Polvani *et al.*, 1994). Unfortunately I could not turn this lack of robustness into a criterion that sets

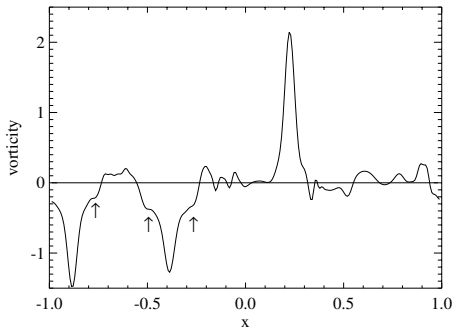

Figure 3.10: A cut through the relative vorticity field. The large anti-cyclonic vortices show a strange kink (indicated with arrows) in their vorticity distribution, while the small cyclonic vortex has a regular profile.

limits on the properties of the vortices that are expected.

In the literature there is only one such a report as far as I know. With a reduced set of equations Cushman-Roisin and Tang (1990) found that cyclonic vortices with huge perturbations in free surface height become unstable and break up if they get larger then the Rossby radius of deformation. In experiments with the full shallow-water equations with a single Gaussian vortex I could confirm this result, but the instability turns out to be very sensitive to the depth of the depression. The instability is very clear if the free surface height drops to some 10 percent of its average value, but at 25 percent the instability could not be noticed. Such large depressions are very hard to reach with decaying shallow-water turbulence experiments, and that is why Polvani *et al*. (1994) could not verify it.

To summarize, the inverse energy cascade is slowed down when vortices grow larger than the Rossby deformation radius. The reason is that a typical vortex becomes shielded. However this does not imply that the vortex growth stops, because the merging leads to more efficient growth at small Burger number. So the Rossby deformation radius does not impose an upper limit to the vortex size. Vortices larger than the Rossby deformation radius do look less robust, but this could not be translated to a maximum size of the vortex that can develop.

3.5 Two-dimensional turbulence and a shearing background flow

The simulations presented so far address turbulence in the absence of a background shear. In an accretion disk, however, the turbulence is superposed on Keplerian shear flow. How 2D-turbulence develops when it is subjected to a shear flow, is a topic which received little attention.

Here I restrict myself to uniform shear flows (with a linear velocity profile) because these are unlikely to support 2D-turbulence so that, just as in the previous sections, decaying turbulence and not forced turbulence is studied. For 2D-incompressible flow it is easy to show (Toh *et al.*, 1991) that any turbulence superposed on a uniform shear flow must be decaying. Because the turbulence here is 2D-compressible similar reasoning can only make it plausible that turbulence decays. This follows from the enstrophy equation. Multiply the ideal vorticity equation by the vorticity:

$$\frac{\partial \omega^2}{\partial t} = -2\omega \nabla \cdot (\omega \vec{v}) = -\nabla \cdot \omega^2 \vec{v} - \omega^2 \nabla \cdot \vec{v}.$$

Next split the flow in contributions from the uniform shear flow (indicated with index 0) and the turbulence (indicated with index 1):

$$\frac{\partial \omega_1^2}{\partial t} = 2\omega_0 \nabla \cdot (\omega_0 + \omega_1)\vec{v} - \nabla \cdot (\omega_0 + \omega_1)^2 \vec{v} - \omega_0^2 \nabla \cdot \vec{v} - 2\omega_0 \omega_1 \nabla \cdot \vec{v} - \omega_1^2 \nabla \cdot \vec{v},$$

where the first term on the right hand side comes from the time derivative of the vorticity which has been expressed as a spatial derivative with the help of the vorticity

equation. Then integrate over the area and use the boundary conditions (periodic or free slip closed boundaries are used):

$$\frac{\partial}{\partial t}\int\int \omega_1^2 dA = -2\omega_0 \int\int \omega_1 \nabla\cdot\vec{v}_1 dA - \int\int \omega_1^2 \nabla\cdot\vec{v}_1 dA.$$

The result shows that turbulence can only grow at the expense of the shear flow if there is a negative correlation between vorticity and divergence of the turbulence. Since simulations are started from a balanced state so that initially $\nabla\cdot\vec{v}$ is small, it is expected that the right hand side is approximately zero. Also at later times, when non-linear interactions or the overreflection instability have created a non-vanishing $\nabla\cdot\vec{v}$, the vorticity and divergence are found to be approximately uncorrelated. If a diffusion process is incorporated then an extra negative term is added on the right hand side of the equations above, indicating that the enstrophy of the turbulence is a decaying function of time. This behavior is also observed on average when the enstrophy is monitored during the simulations. It exhibits small amplitude, short term fluctuations around a decaying curve. So, just like in the previous sections, the turbulence decays.

Simulations were done with a modified version of the numerical algorithm because the (large) shear leads to serious dispersion errors. It was found that the partly fourth order modification (Takano and Wurtele, 1982) of the Arakawa-Lamb scheme gave considerably better results for these kind of simulations than the second order scheme. Therefore, the partly forth order, algorithm is used throughout this section.

The equations solved are just the continuity and momentum equations, Eqs. (3.2), without contributions from Coriolis acceleration and effective gravity but including shear flow; $\vec{v}$ consists of two parts: the linear shear flow $\vec{v}_0 = sy\hat{x}$ in the x-direction and the turbulence $\vec{v}_1$. The new non-dimensional parameter in this problem is the ratio of shear speed (over the typical length scale L) over typical turbulent speed: V_0/V, where $V_0 = s \times L$.

Simulations over 50 initial eddy turnover times were performed for the same initial turbulent field but with different values of the shear. The shear V_0/V was varied between the values 0 and 3.6, where V/L was determined from the rms initial relative vorticity. The potential vorticity distribution of four simulations is shown in Fig. 3.11. For small values of the shear ($V_0/V = 0.06$) the potential vorticity looks very similar to that of ordinary 2D-turbulence without shear. When the shear is increased ($V_0/V = 0.11$), retrograde vortices are removed. These are the white vortices with vorticity of the opposite sign to that of the shear of the background flow. This behavior is well-known (Kida, 1981) and has also been observed in previous studies (Marcus, 1988; Toh *et al.*, 1991). If the shear gets larger than 0.135 times the peak vorticity of a vortex, then that eddy is torn apart (Legras and Dritschel, 1993). The reason is that the vorticity is distributed beyond the separatrix of the stream function, Fig. 3.12. This allows (potential) vorticity to be removed from the vortex (a process called vortex stripping) and be carried away to infinity, thus degrading the vortex. For vortices of the opposite sign (the black ones in Fig. 3.11), the position of the separatrix of the stream function is well outside the vorticity distribution. Therefore, these vortices survive at these values of the shear.

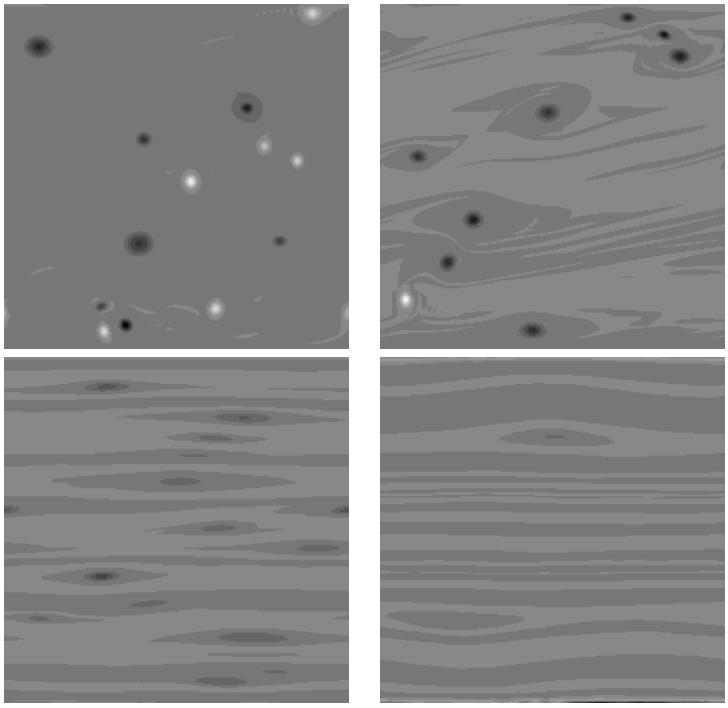

Figure 3.11: Potential vorticity distribution for four different values (left to right, top to bottom) of the shear ($V_0/V = 0.06$, 0.11 and 1.8) after 50 and ($V_0/V = 3.6$) after only 12 eddy turnover times.

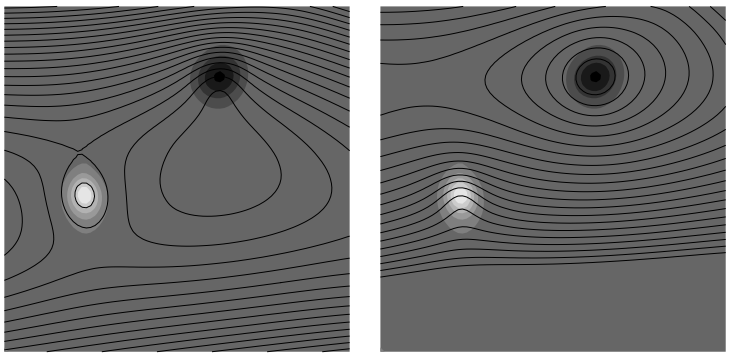

Figure 3.12: Zoom in of the lower left corner of the potential vorticity distribution of the simulation with shear=0.11 in Fig. 3.11. Superimposed are contours of the stream function: on the left in a frame co-moving with the retrograde vortex, on the right co-moving with the prograde one. It is clear that the separatrix of the stream function is at the edge of the retrograde vortex while the potential vorticity of the prograde vortex is well inside its separatrix. The slight misalignment between streamlines and potential vorticity can be attributed to uncertainty in the advection speed of the vortices.

A further increase in shear ($V_0/V = 1.8$) leads to the destruction of all retrograde vortices. The prograde vortices are now strongly deformed in the shape of an ellipse. An animation of the potential vorticity shows that the mobility of the vortices in the direction perpendicular to the shear decreases. The prograde vortices stay at approximately the same y-coordinate throughout their lifetimes. There could be several explanations for this phenomenon. Firstly, the result of the elliptical deformation of the prograde vortices is that the velocity induced by the vortex perpendicular to the elongation decreases compared to that of a circular vortex of the same circulation. So vortices at different y-coordinates feel less of each other. Secondly, vortices of opposite sign have the tendency to propel each other through the fluid. This is most clearly exhibited by dipolar vortices (which consist of one positive and one negative vorticity core). Vortices of the same sign only rotate around each other (and merge), but remain localized. With the removal of all retrograde vortices by the shear , it is expected that the mobility of the prograde vortices drops. Thirdly, it is found that the vortices at higher shear are on average weaker, that is they have a lower circulation. This is, at least partly, the result of viscosity. The vortices develop thinner structures which diffuse more easily. For another part it may be intrinsic, namely that vortex merging leads to a larger waste in the presence of a background shear flow. As weaker vortices have weaker interactions, this can also explain the decreased mobility. The drop in mobility in the x-direction is of course compensated by the advection of the shear flow.

The decreased mobility implies that there are fewer encounters with other vortices of the same sign that can be swallowed. So we expect to see fewer mergers and an increase in the number of vortices with increasing shear. In Fig. 3.13 the number of prograde vortices after 50 initial eddy turnover times is plotted as a function of shear. We see a marked increase in the number of vortices when the shear increases from 0.11 to 0.66. This seems to be related to the decreased mobility of the vortices in the direction perpendicular to the shear. For very small values of the shear, from

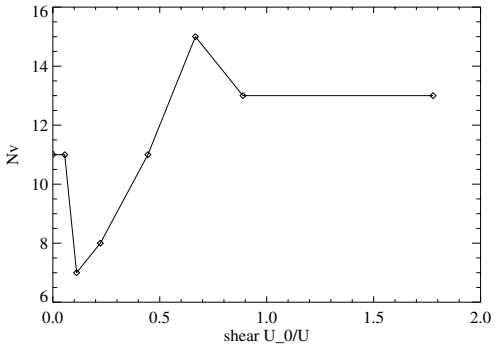

Figure 3.13: The number of prograde vortices as a function of the background shear after 50 initial eddy turnover times. The vortices were identified by eye. The data points are connected by straight line segments.

0 to 0.11, the number of vortices drops. This may be due to an increased inverse energy cascade when a small amount of shear is added forcing eddies onto each others neighbors, a phenomenon known from forced 2D-turbulence (Toh *et al.*, 1991). For larger values of the shear, larger than 0.66, the number of vortices drops slowly.

The final increase of shear ($V_0/V = 3.6$) gets rid of all vortices, Fig. 3.11. There could be several reasons for this.

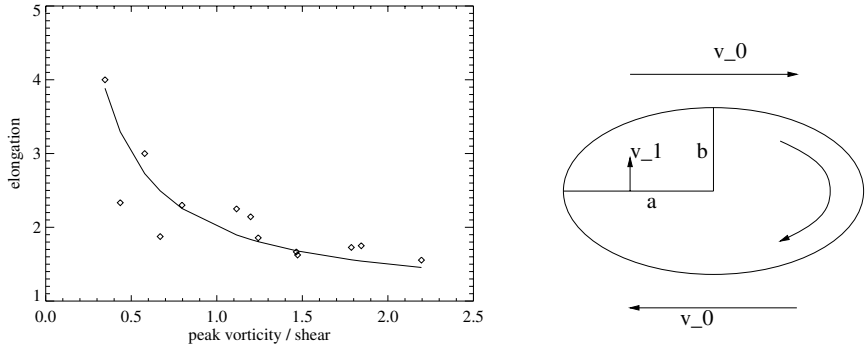

Figure 3.14: On the left, vortex elongation as a function of peak vorticity from one of the simulations. The drawn curve is from a model based on continuity. On the right a sketch of a vortex superimposed on a shear flow. Indicated are the ingredients of the continuity model for vortex elongation.

One phenomenon already observed at lower values of the shear is that vortices adjust their shape and become elongated. Fig. 3.14 shows the measured elongation, semi major axis divided by semi minor axis, of the vortices. The drawn curve is from a model based on continuity (of the potential vorticity transport). Suppose the vortex adds a velocity of magnitude v_1 to the shear flow v_0, Fig. 3.14. Then the net transport of potential vorticity through the semi-major axis is $v_1 \cdot a$. This must equal transport through the semi-minor axis $(v_1 + v_0) \cdot b$. So the elongation of the vortex is $a/b = (v_1 + v_0)/v_1 \approx (\omega + s)/\omega$ where ω is the peak vorticity of the vortex. Considering the simplicity of the argument, the continuity model (drawn line) is a decent fit to the data. What is apparent from Fig. 3.14 is that when the peak vorticity of the vortex drops significantly below the shear of the background flow, the vortex's elongation rises dramatically. It is questionable if a vortex with an aspect ratio of 5 or more can be discriminated from a filament. Such highly elongated structures are not characterized properly by the predicate vortex.

Even if prograde vortices are somehow able to withstand the elongation process, then at high enough values of the shear they will be prone to vortex stripping, the same process that removes retrograde vortices at smaller shear, Fig. 3.12. The exact value of the shear at which vortex stripping starts is hard to calculate because the position of the separatrix also depends on the position and strength of other vortices.

Finally, a third reason for the lack of vortices at large shear is that viscosity is more effective when vortices develop thin structures.

Closely related to the elongation effect is a timing argument against large scale

vortices in strong shear flows. If the time to shear structures apart is much longer then the vortex rotation period:

$$\left(\frac{dv_0}{dy}\right)^{-1} \gg 4\pi \left(\frac{1}{r}\frac{drv_1}{dr}\right)^{-1},$$

then vortices can form. Here the velocity v_0 is to be interpreted as due to the shear flow and v_1 due to the vortex. In the opposite case, eddies will be torn apart by the shear.

These considerations indicate that there is a minimum threshold on the peak vorticity for vortices to exist in a uniform shear flow. The hope that this threshold can be reached by vortex merging is in vain because one of the fundamental observations from decaying 2D-turbulence experiments is that the peak vorticity of a vortex stays almost constant. (The vortex scaling theory of Carnevale *et al*. (1991) is based on this fact.) This, in combination with the apparent lower limit on peak vorticity of vortices in shear flow, leads to a significant difference between 2D-turbulence with and without shear flow. In the absence of shear, no matter how small the initial turbulent fluctuations, vortices form. The strength of the fluctuations determines the time scale of formation. In the presence of a shear flow, the perturbations have to be large enough, namely of the order of the shear in the background flow, otherwise no vortices form at all.

Finally, there is a limit to which the turbulence decay experiments did not extend but which could be important. The gravity wave speed can be combined with the shear to form an intrinsic length scale, $L_s = c_s/s$, rather similar to the Rossby deformation radius. If the typical length scale of the perturbations in the y-direction is larger than L_s then the difference in the background shear over the typical distance is larger than the gravity wave speed. All vortices observed are considerably smaller than L_s (in their cross-stream extent). In experiments on single vortices in shear flows, those that were close to this limit broke up into two smaller vortices. The author has not been able to produce a vortex larger than L_s. This intrinsic length scale, L_s, seems to put an upper limit to the cross-stream size of vortices that are to be expected in shear flows.

3.6 Discussion

In this section the implications of the phenomena described in the previous sections for 2D-turbulence in an accretion disk are discussed.

3.6.1 Rotation of the disk

In Sect. 3.4 the influence of the Coriolis force on shallow-water turbulence was studied. It was found that the inclusion of such a simple new element (and 2D-compressibility) could already change the character of standard 2D-turbulence considerably. 2D-turbulence changes its character if the typical length scale gets larger than the

Rossby radius of deformation:

$$L_D = c_s/f.$$

For an accretion disk the equivalent of the planetary vorticity f is the vorticity of the Keplerian disk $f = 0.5(GM/r^3)^{1/2}$ and this can be used to determine the Rossby deformation radius. It can also be argued that f is twice the rotation frequency. Then the Rossby deformation radius is four times larger. To settle this controversy an experiment was done in which an azimuthally symmetric density perturbation was allowed to develop freely in an accretion disk (1.5D model). This excites compressional waves that move to the inner and outer edge of the disk. What is left is a bump in the density (in geostrophic equilibrium) with a typical width given by the Rossby deformation radius. The Rossby deformation radius determined in this way was found to be in between both estimates given above: $L_D = rc_s/v_{kep}$. This is to be compared with the typical half-thickness H of a thin accretion disk which follows from hydrostatic equilibrium in the direction perpendicular to the disk (z-axis): $GMz/(r^2+z^2)^{3/2} = -(c_{s_{iso}}^2/\rho)(\partial\rho/\partial z)$ which approximates to $GMH/r^3 = c_{s_{iso}}^2/H$. It is observed that the Rossby deformation radius is of the order of the half thickness of the disk. So if the vortices get larger than the half thickness of the disk then shallow-water turbulence becomes different from standard 2D-turbulence.

The most important conclusion from Sect. 3.4 is that vortices can grow larger than the Rossby deformation radius. So the Coriolis force poses no objection to large-scale vortices in accretion disks. Most changes in the character of 2D-turbulence at small Burger number result from a change in the vorticity profile of a typical vortex. Vortices tend to be shielded. It is unclear if something similar can occur in an accretion disk as a shear flow was left out of the simulations in Sect. 3.4 while in Sect. 3.5 it was shown that a shear flow is inhospitable for the wrong kind of vorticity. It is, therefore, quite well possible that the shielding due to a small Burger number is removed by the shear in an accretion disk. This makes it hard to apply the other results from Sect. 3.4 to an accretion disk.

3.6.2 Keplerian shear

In Sect. 3.5, shallow-water turbulence superimposed on a uniform shear flow was studied. Several of the conclusions drawn there also apply to 2D-turbulence in an accretion disk, as will be discussed in this section.

The most obvious observation from the shear flow experiments is that there is an asymmetry between prograde and retrograde vortices, Fig. 3.11. Retrograde vortices have the tendency to be stripped and torn apart. This behavior is known from a single vortex in a shear flow where only those vortices with peak vorticity larger then 7.4 times the shear (Legras and Dritschel, 1993) survive. In the experiments done here where many vortices interact, the requirement on peak vorticity is even higher. For example, in many experiments where the initial vorticity fluctuations were up to 17 times larger than the shear, no retrograde vortices were found after 50 initial eddy turnover times. So an accretion disk is much more likely to have prograde vortices than retrograde. This implies that the vortices will be dominantly

of anti-cyclonic nature.

Prograde vortices were found to withstand shear much better. But at high values of the shear, larger than the peak vorticity in the vortices, they are also lost. It was argued that vortices get elongated to such an extent that it is hard if not impossible to identify them as vortices. If the prograde vortices are not stretched then they are stripped, just as retrograde vortices at lower shear. It has not been possible to give a firm bound on the ratio peak vorticity to shear below which vortex stripping starts, because the position of the separatrix with respect to the vorticity distribution is determined not only by the relative strength of the shear but also by the relative strength and position of other vortices. So, the simulations suggest that there is a kind of lower limit to the peak vorticity of prograde vortices as well if they are supposed to withstand a given shear. The peak vorticity should be of the order of the shear or larger. This fact can be used to calculate a Rossby number for vortices in an accretion disk because the Rossby number is the ratio of relative to planetary vorticity. The relative vorticity of the vortices is of the order of the shear or larger, which is $3v_{\mathrm{kep}}/2r$ in an accretion disk. In the previous Sect. 3.6.1 it is argued that the "planetary vorticity" of a Keplerian flow is v_{kep}/r so that we find a Rossby number of 1.5 or larger. So these vortices are not in geostrophic equilibrium, an assumption made in previous work (Adams and Watkins, 1995). Strong (anti-cyclonic) vortices with large Rossby numbers are probably low pressure areas where the centrifugal force is balanced by the pressure force. For Rossby numbers of order unity the Coriolis force alone might be large enough to balance the centrifugal force, so that the perturbation in pressure is small.

With the simple continuity model for vortex elongation (semi-major over semi-minor axis $a/b \approx (\omega + s)/\omega$), the Rossby number of a vortex can be connected to its shape. If the background shear is the result of a Keplerian flow then we can relate the shear again to the "planetary vorticity". This gives an estimate for the Rossby number of the vortex:

$$\mathrm{R_O} = \frac{\omega}{f} \approx \frac{1.5}{a/b - 1}.$$

This relation implies that geostrophic vortices in an accretion disk hardly look like Jovian or Earth like vortices, but are very elongated structures that are easily taken as filaments. They should also be far apart otherwise they are prone to vortex stripping. This implies that they will have few interactions with each other. From the point of view of mass and angular momentum transport in the radial direction through an accretion disk, this is probably not a very interesting situation. Efficient transport probably requires intense interactions among vortices and it is questionable if geostrophic vortices could live through this.

Another problem in accretion disks is how to create the required intense vortices. Rossby numbers of order unity and larger imply that we are dealing with huge disturbances of the Keplerian profile. At the inner edge of the accretion disk it may be in contact with a central compact object and large perturbations in vorticity can be expected (although not necessarily only in the component perpendicular to the disk). This is equally true for the outer edge where a jet of overflowing material impinges on the disk. But in the middle of the disk, there seems to be little cause

for strong vorticity perturbations. Perhaps they can be created by magnetic fields or the interaction of shock waves. The combination of an incident and a reflected shock and a Mach stem (which together form the letter Y) is known to produce strong shear layers (e.g. Srivastava, 1994) that might break up into vortices, but this is mere speculation. Besides, high resolution 2D-simulations of shocks in accretion disks (Godon, 1997) gave no indication of long-lived vortices.

Shear does not only put conditions on the strength of the surviving vortices but also on their size. Vortices in cross-stream direction larger than the intrinsic length scale $L_\mathrm{s} = c_\mathrm{s}/s$ have not been observed in the experiments. If the Keplerian shear is substituted, one obtains:

$$L_\mathrm{s} = \frac{2c_\mathrm{s}}{3v_\mathrm{kep}} r,$$

which again is of the order of the thickness of the accretion disk. So it is not obvious how to produce long lived 2D-vortices that are larger in cross-stream direction than the thickness of the accretion disk.

For vortices in an accretion disk that have elongations of order 2 or 3 (which is common for vortices on Earth and Jupiter), the Rossby number is not small and they are also not larger then the thickness of the disk. This points in the direction of an internal inconsistency. From the start it was assumed that the fluid motion is essentially two-dimensional. Fluids are known to behave as if they are two-dimensional under a number of different conditions, the most important of which is that the Rossby number is small. Another is that the flow geometry is thin. If these conditions are violated, as seems to be the case for vortices in accretion disks, then it must be the stable stratification in the direction perpendicular to the disk that keeps the dynamics two-dimensional. If this condition is not satisfied, then there is no reason to expect long-lived two-dimensional vortices to be abundant. This does not exclude that they exist but it now comes as no surprise that most numerical studies of accretion disks do not show vortices. Firstly, often the perturbations in vorticity have been chosen too small to develop into vortices. Secondly, the resolution is often too low to resolve vortices smaller than the thickness of the disk (and I don't expect larger vortices). Thirdly, in 3D-simulations that don't show hydrostatic equilibrium in the vertical direction, long lived 2D-vortices are not expected.

The conclusions reached here are rather different from those of Bracco *et al*. (1998). They also noted the threshold on initial vorticity perturbation for vortices to develop in Keplerian shear. However, neither did they relate this to the peak vorticity of the vortices, nor did they come to the conclusion that the Rossby number is of order unity or larger in vortices (although this is visible in their Fig. 2). Also because they mainly did 2D-incompressible calculations, they didn't find that L_s acts as an upper limit to the vortex size. These are the reasons why they are much more optimistic about long-lived 2D-vortices in real accretion disks then the author of this article.

Acknowledgements. I want to thank prof. J. Kuijpers and prof. J.T.F Zimmerman for their help with this paper.

Appendix: A vortex recognition algorithm

An automatic vortex recognition algorithm was described by McWilliams (1990). Its main disadvantage is that it uses only one vorticity contour to determine if a flow structure is a vortex. Here it was prefered to use all points that belong to the candidate vortex for that decision. Therefore, a new algorithm to recognize vortices was constructed. Many of the steps are extensively described by McWilliams (1990). The main difference is that the Weiss field is used instead of the vorticity, and that the accuracy of a Gaussian fit replaces the vortex shape analysis.

- Determine the Weiss field (Brachet *et al.*, 1988) out of the stream function. The Weiss field is strain squared minus the vorticity squared: $S_1^2 + S_2^2 - \omega^2$, where $S_1 = \partial u/\partial x - \partial v/\partial y$, $S_2 = \partial v/\partial x + \partial u/\partial y$.
- Determine the local minima.
- If the minima are within 3 grid cells from each other then keep the strongest.
- Determine for each minimum the grid points that fall within the $0.1\times$ minimum contour of the Weiss field. This contour sets the boundary of the vortex.
- Remove the candidate vortices that are too large or too small (6 grid cells).
- From those candidates that overlap only keep the one with the strongest minimum.
- Fit a Gaussian profile to the grid points of the candidate.
- Calculate the chi-squared value of the fit; if it is too large then remove the candidate vortex.

Candidates that pass these tests are accepted as a vortex.

Chapter 4

A Single Vortex in a Two-Dimensional Polytropic Accretion Disk

Abstract. A single vortex in a two-dimensional polytropic Keplerian shear flow is studied with the help of numerical simulations. It is found that fluid motion within the vortex is to a good approximation described by a balance between Coriolis, centrifugal and pressure forces. The shape of the vortex, either stationary or nutating, is well explained by the Kida vortex model. The nutation leads to the phenomenon of chaotic advection. The vortex excites two compressional waves which interact with the supersonic Keplerian flow and give rise to two trailing spiral bores (shocks) (one inward, one outward). The vortex drifts in the azimuthal direction owing to gyres (secondary vortices) created by the deflection of the flow around the vortex. A radial drift is also observed. Implications for accretion are discussed. Dust released during the simulation concentrates in the vortex confirming earlier incompressible calculations.

M.D. Nauta, J. Kuijpers and J.T.F. Zimmerman
submitted to *Astronomy and Astrophysics*

4.1 Introduction

The ubiquity of two-dimensional (2D) vortices in large-scale geophysical flows led to the suggestion that such vortices are also present in accretion disks (Abramowicz *et al.*, 1992). The underlying reason for such omnipresence is an inverse energy cascade that is typical for quasi 2D-flows. Whether or not a similar inverse energy cascade and the accompanying vortices are likely to occur in an accretion disk, was discussed in a previous paper (Nauta, 2000). It was concluded that the conditions for quasi 2D-behavior are not exactly satisfied: the ratio height over width and the Rossby number of vortices in accretion disks are of order unity or larger, so any quasi 2D-behavior depends sensitively on vertical hydrostatic equilibrium. As a result, ubiquitous occurrence of vortices in accretion disks remains uncertain. However, we have shown that, once created, 2D-vortices with Rossby numbers of order unity can persist over a considerable amount of time, which was recently corroborated for vortices in protoplanetary disks (Godon and Livio, 1999). This is also the approach that we take in this paper: we assume that somehow a vortex is created and we superimpose it on a Keplerian shear flow. It is the subsequent evolution that we study with the help of a numerical code (Nauta and Tóth, 1998). In this paper we restrict the discussion to a single vortex in a polytropic, two-dimensional Keplerian flow with uniform background surface density.

Previous work on vortices in accretion disks has concentrated on highlighting the similarity with geophysical flows (Yecko, 1995; Adams and Watkins, 1995; Bracco *et al.*, 1998). Yecko (1995) performed simulations of single and multiple vortices in accretion disks with a similar code as ours. Emphasis in his computations is on the qualitative overall behavior while we try to understand the detailed physical processes and try to get some quantitative results. The analytical vortex solutions of Adams and Watkins (1995) make use of the geostrophic approximation (a balance between pressure gradient and Coriolis force) which is unrealistic in an accretion disk. That is why these solutions have not been used in the computer simulations of the next sections. However, these authors do point out the relevance of self-gravity. This could lower the effective Rossby number making their approximations more valid. Self-gravity is not included in our simulations. The recent work of Bracco *et al*. (1998, 1999) is different from ours in that it mainly uses incompressible calculations whereas our code is 2D-compressible. Further they focus on a collection of vortices in the whole disk rather than looking in detail at a single vortex. These authors are primarily interested in the role of vortices during planet formation while our interest is in the transport properties of vortices, in particular in the transport of angular momentum induced by a vortex in a disk.

The outline of this paper is as follows: First we present the equations and method of solution in Sect. 4.2; then the internal structure of the vortex in Sect. 4.3; the interaction of the vortex with its surrounding in Sect. 4.4; and finally the discussion and conclusion in Sect. 4.5.

4.2 Equations

The equations to be solved are the polytropic 2D-gas equations in a coordinate frame rotating at angular frequency Ω:

$$\begin{aligned} \frac{\partial \Sigma}{\partial t} + \nabla \cdot \Sigma \vec{v} &= 0, \\ \frac{\partial \vec{v}}{\partial t} + (\vec{v} \cdot \nabla)\vec{v} + 2\Omega \hat{z} \times \vec{v} &= -\frac{1}{\Sigma} \nabla P + \nabla \left(\frac{GM}{r} + \frac{\Omega^2 r^2}{2} \right), \\ P &= K \Sigma^\gamma, \end{aligned}$$

Σ is the surface density (the height integrated density), $\vec{v}$ the 2D velocity in the rotating coordinate frame, P the height integrated pressure, M the mass of the central star, r the distance to the central star and $\hat{z}$ is a unit vector perpendicular to the disk. For Ω we take the Keplerian rotation frequency at $r = R : \Omega = \sqrt{GM/R^3}$. Different interpretations of these equations are possible. Firstly, in the case of $\gamma = 2$, where the pressure gradient term is proportional to Σ, they describe motion of a thin layer of 3D-incompressible fluid with a free surface (the shallow water equations). Secondly, if motion is interpreted to be strictly two-dimensional, then these equations describe 2D polytropic compressible gas dynamics with arbitrary γ. A third interpretation sometimes encountered is that of a hydrostatic gas layer with a free surface. In this case the pressure is partly due to 3D-compressibility and partly due to a larger height of the gas column. As such it is a hybrid of the first and second interpretations. These different interpretations also imply that similar phenomena can be given different names. For example, what in the shallow water case would be called gravity waves could be called sound waves according to the second interpretation. In this article preference is given to shallow water terminology to emphasize that the gas dynamics that we study uses a polytropic relation instead of the full energy equation.

The equations can be combined to give the (pseudo scalar) equation of advection of potential vorticity (or vortensity):

$$\left(\frac{\partial}{\partial t} + \vec{v} \cdot \nabla \right) \frac{2\Omega + (\nabla \times \vec{v}) \cdot \hat{z}}{\Sigma} = 0.$$

Potential vorticity is used extensively in diagnosing the simulations.

The equations are made dimensionless by introducing typical scales of the vortex: its radial length scale L, its internal velocity scale V, its time scale $T = L/V$ and the speed of sound of the unperturbed accretion disk c_s:

$$\frac{\partial \Sigma}{\partial t} + \nabla \cdot \Sigma \vec{v} = 0, \tag{4.1}$$

$$\begin{aligned} \frac{\partial \vec{v}}{\partial t} + (\vec{v} \cdot \nabla)\vec{v} + \frac{\Omega L}{V} 2\hat{z} \times \vec{v} &= -\frac{c_s^2}{\gamma V^2} \frac{1}{\Sigma} \nabla \Sigma^\gamma + \\ &\left(\frac{\Omega L}{V} \right)^2 \nabla \left(\frac{R^3}{L^3 r} + \frac{r^2}{2} \right). \end{aligned} \tag{4.2}$$

In Eqs. (4.1) and (4.2) the derivatives, all lower case symbols (except c_s) and Σ are dimensionless. The scale of the surface density is arbitrary and depends on the sound speed and constant K: $c_s^2 = \gamma K \Sigma_0^{\gamma-1}$. The following non-dimensional numbers can be recognized: the Rossby number of the vortex

$$\mathrm{R_O} = V/(\Omega L),$$

its Mach number

$$\mathrm{M_a} = V/c_s,$$

and

$$\mathrm{R_S} = R/L,$$

the dimensionless distance at which the Keplerian velocity $v_{\mathrm{kep}} = \sqrt{GM/R}$ equals the rotation rate of the coordinate frame ΩR. This is also the distance at which the vortex will be superimposed. These three non-dimensional numbers determine the evolution of the system. Other important quantities of an accretion disk can be expressed in them, most notably the thickness of the (thin) disk at distance R (which is based on the assumption of hydrostatic equilibrium in the vertical direction and uses the isothermal speed of sound):

$$H/R \equiv c_s/(\sqrt{\gamma} v_{\mathrm{kep}}) = \mathrm{R_O}/(\sqrt{\gamma}\mathrm{M_a}\mathrm{R_S}),$$

and the vertical aspect ratio of the vortex:

$$L/H = \sqrt{\gamma}\mathrm{M_a}/\mathrm{R_O}.$$

Here the Rossby number, the Mach number and the co-moving radius $\mathrm{R_S}$ are chosen as independent non-dimensional numbers.

The initial condition consists of a circular perturbation in velocity $v \propto \xi \mathrm{erf}(\xi^2)$ (ξ is the distance to the vortex center) that is added to the Keplerian profile in a co-rotating frame:

$$v_k V = \sqrt{GM/rL} - \Omega r L = \left(\mathrm{R_S}^{3/2}/\sqrt{r} - r\right) V/\mathrm{R_O}. \tag{4.3}$$

Other circular perturbations with similar non-dimensional parameter values resulted in very similar vortices. All give rise to very smooth shapes in potential vorticity. The vortex core is well described by a Gaussian vortex. This is related to the diffusion process that is used to stabilize the calculation. Here a biharmonic operator (Δ^2) was used on all three variables (Σ, v_r, v_ϕ) with an e-folding time of 10 orbits for waves at a wavelength of the diameter of the vortex.

We choose a simulation domain of $20L$ squared and use grids of 128×128 or 256×256 grid points. The adiabatic index is $\gamma = 1.4$ in all calculations. At low resolution, simulations were done within the range: $0.3 < \mathrm{R_O} < 2.5$, $0.1 < \mathrm{M_a} < 0.9$, $15 < \mathrm{R_S} < 90$, $0.03 < H/R < 0.4$ and $0.14 < L/H < 1.4$. These numbers are based on the initial condition and they may vary considerably during the simulation. For example, after ten orbits around the compact object, which is the typical duration of

a run, the aspect ration L/H is found to vary from 0.12 to 0.84. Efforts to get this number above unity failed because of the development of negative densities (lack of pressure support). Only a small number of experiments was done at high resolution. The numerical technique used, the Arakawa-Lamb scheme (1981), has been developed for geophysical fluid dynamics and its merits (in particular enstrophy conservation) were discussed in Nauta and Tóth (1998). The partially fourth order version of the Arakawa-Lamb scheme (Takano and Wurtele, 1982) is used, just as in part of Nauta (2000). Only a sector of an accretion disk is simulated (approximately $1/6$) and periodic boundary conditions are used in the azimuthal direction. (So strictly speaking it is not a single vortex that is simulated but there are several mirror vortices of which the influence is assumed to be negligible.) In the radial direction a kind of absorbing boundaries are used (Martinsen and Engedahl, 1987): the solution is forced to an unperturbed Keplerian disk in a smooth way. Extensive use is made of a vortex recognition algorithm. It is briefly described in Nauta (2000) and it is based on a similar algorithm by McWilliams (1990). The main difference with Nauta (2000) is that a potential vorticity contour is used as boundary of the vortex (instead of a contour in the Weiss field). The value of the potential vorticity contour is chosen such that it is close to what the Weiss contour would give.

4.3 Vortex properties

Simulations are performed over ten orbits around the compact object. It is found that after an initial adjustment phase, during which many waves are excited (and removed by the absorbing boundaries) and which lasts for some four orbits, a kind of stationary state is reached. It is this state that is described here.

As a typical example, a vortex with initial $\mathrm{R_o} = 0.95$, $\mathrm{M_a} = 0.48$, $\mathrm{R_s} = 20$ is discussed. The corresponding thickness of the disk is: $H/R = 0.085$ while the initial aspect ratio is $L/H = 0.59$; the extent of the vortex in z-direction is larger than its radial extent. The non-dimensional parameters after the initial adjustment phase are: $\mathrm{R_o} = 1.1$, $\mathrm{M_a} = 0.43$, $\mathrm{R_s} = 26.9$, $H/R = 0.085$, $L/H = 0.44$. Where appropriate the influence of other parameter values is discussed.

The potential vorticity after 10 orbits is shown in Fig. 4.1. Observable is the gradient in the unperturbed Keplerian disk where the potential vorticity drops as $r^{-1.5}$ (because of the uniform surface density) and the vortex as the prominent dark elongated region close to the middle of the plot. There is also some spurious small amplitude potential vorticity at the absorbing boundaries which is of little consequence.

The associated surface density and velocity fields on the complete domain are shown in Sect. 4.4, Fig. 4.11. Fig. 4.1 (on the right) shows a zoom in of the vortex. The density (and pressure) distribution within the vortex is "quadrupolar". Keplerian rotation dominates the velocity field. Close inspection shows that the velocity is parallel to the potential vorticity contours which is in agreement with potential vorticity advection. Rotation is clockwise in this anti-cyclonic vortex. Cyclonic vortices are torn apart (Marcus, 1993; Nauta, 2000).

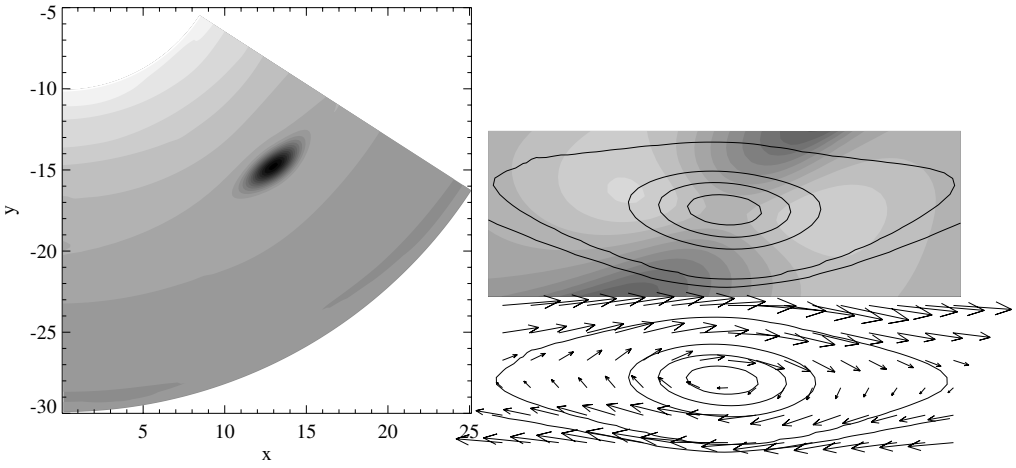

Figure 4.1: The potential vorticity distribution (range: -1.3 to 1.5) of the standard vortex after 10 orbits. On the right a zoom in of the surface density (range 0.79 to 1.22) and of the velocity with superimposed some potential vorticity contours. The vector plot of the velocity is on a polar grid and doesn't show the geometrical distortion of the other two pictures. The compact object is at the top of the pictures. The (inner) disk rotates counter clockwise. Dark shading implies low values, light shading high values.

4.3.1 Balance of forces

The saddle point in surface density (Fig. 4.1) is the result of balance of forces within the vortex. The stationary state implies that a balance should exist between Coriolis force, pressure gradient and centrifugal force (gradient wind balance). (The curvature of the streamlines that gives rise to the centrifugal force, has two causes: the vortex and the central compact object.) Because the Rossby number is of order unity the inward (towards the vortex center) Coriolis force should be of the same order of magnitude as the outward centrifugal force.

First the ϕ-component of the balance of forces is analyzed (Fig. 4.2). The analysis of the forces is done in a coordinate system co-rotating (solid-body) with the center of the vortex, also taking the azimuthal drift speed (Sect. 4.4) into account. The grayscale gives the sum of the three forces, the dashed curves are potential vorticity contours and the solid lines are the lines where $v_r = 0$ and $v_\phi = 0$ respectively. Note that these lines distribute the vortex in four quadrants. It is observed that in the left half of the vortex there is a net force in the positive ϕ-direction. In the other half the net force is in the opposite direction. This is in agreement with rotation within the vortex. The clockwise flow should accelerate and decelerate in the ϕ-direction respectively. To check the balance of forces the net force along the line $v_\phi = 0$ is determined because here there is no azimuthal acceleration or deceleration. Shown in Fig. 4.2 is the net force along a grid line that comes closest to the line $v_\phi = 0$. The Coriolis force balances the centrifugal force approximately and the pressure force

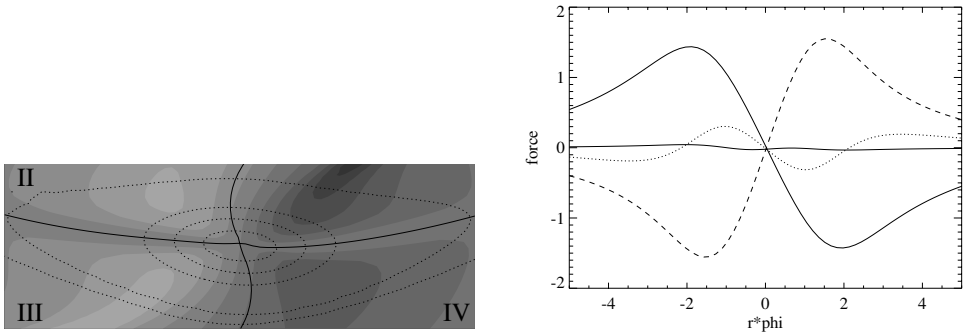

Figure 4.2: Grayscale distribution (range -2.2 to 1.4) of the net force density in the azimuthal direction. Superimposed are some potential vorticity contours and the lines where $v_r = 0$ and $v_\phi = 0$. The picture next to it shows the individual forces along a grid line closest to the line $v_\phi = 0$. The centrifugal force (dashed) is found to balance the Coriolis force (solid) and the pressure force (dotted). The net force is indicated by the middle solid line and is close to zero everywhere.

only contributes a little. The sum of the three forces is almost zero. The small wiggle in the middle can probably be attributed to the curvature in the line $v_\phi = 0$ and inaccuracy in determining gradients in the middle of the vortex.

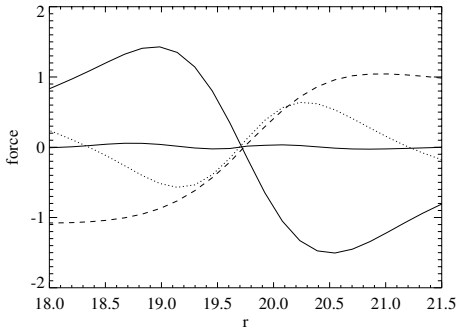

Figure 4.3: The balance of forces "along" the line $v_r = 0$. The Coriolis (solid) is balanced by the centrifugal (dashed) and pressure (dotted) forces. The middle solid line is the sum of all three and should be zero in case of a stationary state.

A similar analysis is applied to the radial force (Fig. 4.3). The balance of forces along the grid line that is closest to the line $v_r = 0$ is displayed. The zero-order Keplerian balance was removed to show the balance in the vortex. The centrifugal and pressure forces combined, balance the inward Coriolis force. There is no sign of a higher order balance (involving accelerations). Note that in the radial direction the pressure force is outwardly directed with respect to the vortex center (Fig. 4.3) while in the azimuthal direction the pressure force is inwards (Fig. 4.2). This is a result

of the elliptical shape of the vortex, which makes the curvature radius and thus the centrifugal force in both directions different and which leads to a larger inward Coriolis force in the radial direction. This explains the saddle shape in surface density (pressure) which is very different from that of terrestrial vortices.

Of course these results depend on the parameters chosen. Decreasing the Rossby number implies increasing the influence of the Coriolis force. So at $R_O \approx 0.5$ a high pressure vortex is found instead of the saddle point because the ϕ-component of the centrifugal force needs help from the pressure force to balance the Coriolis force, even in the ϕ-direction and even though the vortex is very thin. The opposite occurs if the Rossby number is increased. Now the pressure has to come to the aid of the Coriolis force to make a balance. At $R_O \approx 2.5$ the pressure gradient in the radial direction is zero. The dependence on Mach number is small. In simulations with a higher resolution and a lower viscosity an imbalance is found. This is the result of non-stationary motion (see Sect. 4.3.3).

4.3.2 Shape analysis

A notable feature of the vortex is its shape. It is not circular but elliptic. This shape can be compared with that of other vortices in shear flows, for example the Great Dark Spot on Neptune (Polvani *et al.*, 1990; LeBeau, Jr., R. P. and Dowling, 1998). An "analytical tool" to understand the shape and orientation is the Kida vortex (Kida, 1981) which encompasses the solutions of Rankine, Kirchhoff, Chaplygin and Moore and Saffman (see Meleshko and van Heijst (1994) for a review). It is a patch of uniform vorticity in a uniform background flow for which analytical solutions exist. If the background is a pure (uniform) shear flow then the vortex shape is known to exhibit different kinds of behavior. It can be stationary, rotating, nutating (rocking) or become stretched to infinity, depending on the relative strength of vortex and background flow, and the initial orientation and elongation.

Similar behavior is found in our simulations. The elongation and orientation are determined from a fit of a rotated elliptical Gaussian shape to the potential vorticity (Fig. 4.4). The elongation is defined as minor over major axis, and the orientation as

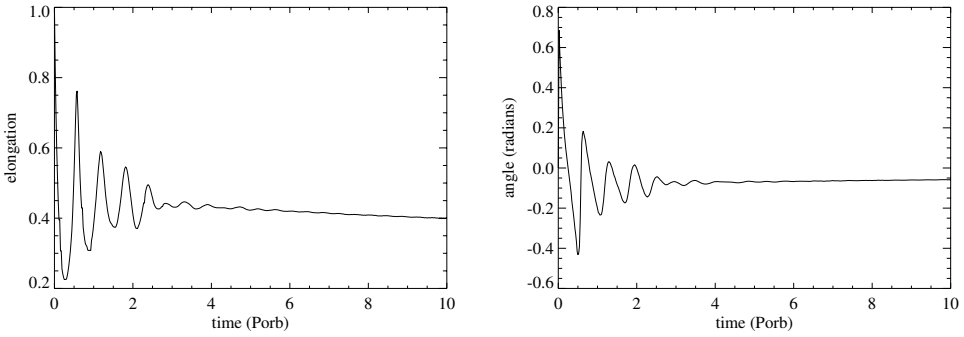

Figure 4.4: The elongation and orientation angle of the vortex as a function of time.

the angle of major axis with the direction of the shear flow measured anti-clockwise (range $-\pi/2$ to $\pi/2$). The elongation is seen to vary considerably initially but it rapidly approaches an almost constant value in time. The orientation of the vortex shows similar behavior. A movie shows that, initially, a rotation over π radians is completed, but the swing back from angle $\pi/2$ to zero occurs very rapidly. This is also visible in the orientation in Fig. 4.4; while the elongation rises rapidly, the orientation jumps from a negative to a positive value. After this first full rotation the variation in angle and elongation indicate that no other full rotations are completed. The vortex nutates a couple of times with rapidly decaying amplitude and then settles into a kind of stationary state. At the end of the simulation after 10 orbits the major axis is 2.5 times larger than the minor axis and the vortex stands under a small angle with the ϕ-direction.

For stationary states the elongation λ can be compared with the analytical solution (Moore and Saffman, 1971):

$$\frac{\text{strain}}{\omega_\text{v}} = \frac{1-\lambda}{\lambda(1+\lambda)},$$

from which

$$2\lambda = -1 - \frac{\omega_\text{v}}{\text{strain}} + \sqrt{1 + 6\frac{\omega_\text{v}}{\text{strain}} + \left(\frac{\omega_\text{v}}{\text{strain}}\right)^2}, \tag{4.4}$$

where we use the strain of the background flow ($rd(v_\text{k}/r)/dr$) instead of the vorticity of the background flow, because it is the strain that leads to deformation (in a uniform shear flow these quantities are numerically equal). The equation holds for a patch of piecewise constant vorticity ω_v while in the simulations we have a continuous vorticity distribution. To relate the two, we use the area averaged relative vorticity as a measure of the vorticity of the vortex, ω_v. This was also done successfully in laboratory work (Trieling *et al.*, 1997) on a vortex in a strain flow. This determination depends sensitively on the location of the edge of the vortex (Sect. 4.2). The measured elongations are compared with the analytical theory in Fig. 4.5. Simulations with an initial Mach number of 0.48 and varying Rossby number are indicated with pluses, while those with initial Rossby number 0.95 and varying Mach number are indicated with diamonds. Simulations where both the Mach and the Rossby number were varied such that initially $L/H = 0.59$, are indicated by crosses. No significant dependence on the third parameter R_S was found. The analytical prediction Eq. (4.4) is indicated with the solid line while the dotted line gives the simple continuity model of Nauta (2000). A reasonable agreement with Eq. (4.4) is found, definitely for strong vortices. The weaker vortices seem to be a bit more robust against shear than the model predicts, although it is also possible that the procedure to determine the vorticity of the vortex gives too low values at small Rossby number. For example, if instead of the area averaged vorticity the peak vorticity is used in Eq. (4.4), then all points lie below the theoretical curve. The continuity model is a worse fit. A slight dependence on Mach number is also observed. This can probably be attributed to the "bores" (shocks) (Sect. 4.4). It leads to compression of the potential vorticity contours in the azimuthal direction.

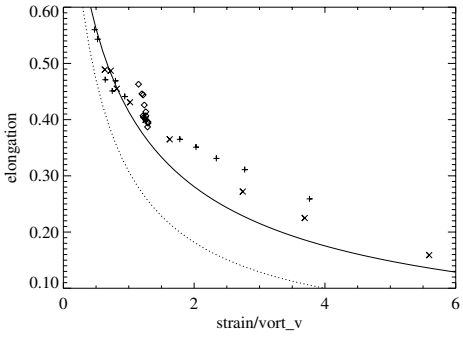

Figure 4.5: The elongation of the vortex as a function of the ratio background strain to vorticity of the vortex, which is like an inverse Rossby number for vortices in an accretion disk. The pluses indicate simulations with (initially) constant Mach number (and R_S) and variable Rossby number, the crosses with constant disk thickness and aspect ratio of the vortex (varying M_a and R_O simultaneously) and the diamonds with (initially) constant Rossby number and various Mach numbers. The drawn line is from Eq. (4.4). The dotted line is the continuity model of Nauta (2000).

One might wonder why the model is such a decent fit to the data even though the model assumes a balance of pressure and centrifugal effects only, which was not the case in our simulations (Sect. 4.3.1). The reason is that the vorticity equation (of which Eq. (4.4) is a solution) is not changed by the inclusion of a constant Coriolis acceleration (in case of incompressible flow). So the velocity field of the model is not changed and this, together with advection of vorticity, sets the elongation.

The analytical theory predicts no angle between the vortex's major axis and the direction of the shear. However, a Keplerian flow is not a uniform shear flow and the geometry is curved instead of Cartesian so it was expected that the orientation would depend on the second derivative of the Keplerian speed (expressed in non-dimensional units):

$$\phi \propto \frac{L^2}{V}\sqrt{\frac{GM}{R^5}} = \frac{1}{R_O R_S}, \tag{4.5}$$

or on R_S because of the geometry. The observed angles are small (mostly less than 12 degrees) and are found not to depend on the distance to the compact object R_S, contrary to Eq. (4.5). Also the β-effect (the spatial variation of the background (potential) vorticity), that is known to drive many geophysical fluid dynamical phenomena, is not important because of the independence of the angle with respect to R_S ($\beta \propto R_O/R_S$). This conclusion is further strengthened by simulations of a vortex in a β-free disk ($v_\phi \propto (1/r - r/R_0^2)$ instead of Eq. (4.3)) which give the same orientation as for a Keplerian flow. Instead, quadratic dependence on the Rossby number is found, and a linear dependence on the aspect ratio (Fig. 4.6). Note that the linear dependence on aspect ratio does not go through the origin. The main source of the rotation is 2D-compressibility as simulations in a shearing sheet (Cartesian grid

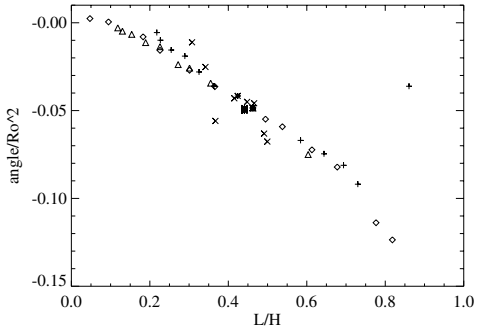

Figure 4.6: The orientation of the vortex divided by the Rossby number squared as a function of the aspect ratio. The non-dimensional numbers used, are those determined after the initial adjustment phase. The different symbols have the same meaning as in Fig. 4.5. The triangles are from simulations at constant disk thickness varying M_a and R_s simultaneously.

with uniform shear flow) indicate. In these simulations the flow is antisymmetric, but even in this case the same orientation is measured as for a Keplerian flow. The observed trends correlate well with the position and strength of the pressure minimum on the edge of the vortex. Since flow deflects around the vortex, a minimum in pressure develops, just like on an airplane wing. With increasing aspect ratio this minimum strengthens and shifts in the downstream direction. This compresses the potential vorticity lines in the first and third quadrant. As a result the elliptical fitting procedure attributes a more negative rotation angle to the vortex. At constant aspect ratio but increasing R_o (and M_a) a similar phenomenon occurs. But now it is the stronger advection by the vortex that increases the strength of the divergent region and shifts it to the downstream side.

4.3.3 Stability and chaotic advection

The simulations presented so far were all done at low resolution (128×128) and with biharmonic diffusion. It is clear (Fig. 4.4) that diffusion influences the vortex substantially and that is why all simulations end up as stationary vortices whose shapes hardly change with time. Indeed, if a simulation is done at high resolution (256×256) and with a highly localized diffusion operator ($\propto \Delta^4$ making the e-folding time 10^5 times longer) then a nutating vortex is found (Fig. 4.7). The oscillations in elongation and orientation persist and after the adjustment phase they become fairly regular. A Kida vortex is fitted to the numerical result. The Keplerian shear sets the background strain and vorticity of the Kida model. The initial elongation and orientation are determined from the observations. The last free parameter in the Kida model, the vorticity of the vortex is adjusted to fit the oscillation period. This vorticity, $\omega_v = -2.09$, is higher than the observed (peak) vorticity of the vortex, $\omega_v = -2.5$ and a bit lower than the area averaged relative vorticity $\omega_v = -1.96$. It is observed that the Kida model is a reasonable fit to the data. The oscillation amplitude

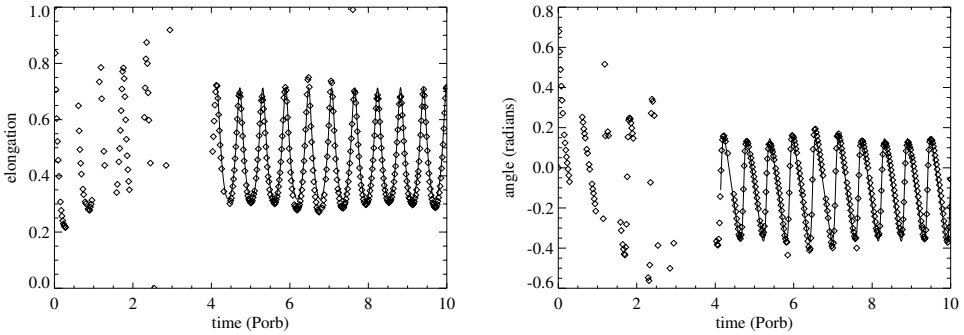

Figure 4.7: The elongation and orientation of a vortex in a low diffusivity run. The vortex nutates. The drawn curve is from a Kida vortex with vorticity -2.09 and the angle is shifted by -0.11 radians. The Kida vortex has been matched after 4 orbital periods.

and the oscillation shape, the only things not fitted for, are fairly well described by the Kida model. The orientation angle has to be lowered by 0.11 radians to give a decent fit (see also Fig. 4.6). Again the amplitude and shape of the oscillations in angle are fairly well caught by the Kida model. That the Kida model can only be an approximation becomes clear if the area of the vortex is monitored. In the Kida model the area is constant but in the simulation it fluctuates with the nutation period at an amplitude of some 10 percent.

The linear stability (Meacham *et al.*, 1990) of the equivalent Kida vortex is also determined. Unstable vortices are known to shed vorticity filaments and perhaps this could explain the weak spiral structure observed in potential vorticity (see Fig. 4.9b). However, for the given shear and vorticity of the vortex, all perturbations of the vortex boundary (up to an azimuthal mode number of more than 100) are linearly stable. The unstable part of phase space in Fig. 4.8 is far removed from the orbit of this vortex. This implies that the weak spiral arms are probably due to the smooth distribution of potential vorticity.

Another characteristic of nutating Kida vortices is their ability to lead to chaotic advection (the seemingly chaotic motion of fluid parcels in a smooth time-dependent flow field) over a considerable area in the neighborhood of the vortex (Polvani and Wisdom, 1990). To investigate if this also occurs for the present vortex, the Poincaré surface of section of the equivalent Kida vortex was determined (using the recipe given by Polvani and Wisdom (1990)). Fig. 4.9 shows the position of a passive tracer particle in the flow field of the Kida vortex, every time a nutation is completed. It was initially released at $r = 0, \phi \approx 0.18$ and in time it fills a large chaotic zone around the vortex. This is related to the advection of passive tracers in the simulation. After 10 orbits around the compact object 1000 tracers are placed on an area as small as 0.25 grid cell squared (full domain is 256×256 grid cells) at $r = 21.46$ and the same ϕ-coordinate as the vortex center. The simulation is continued for another 10 orbits and the tracers are advected. Linear interpolation is used to determine the flow field at the tracer position. As is observed in Fig. 4.9 (the grayscale plots) the tracers first

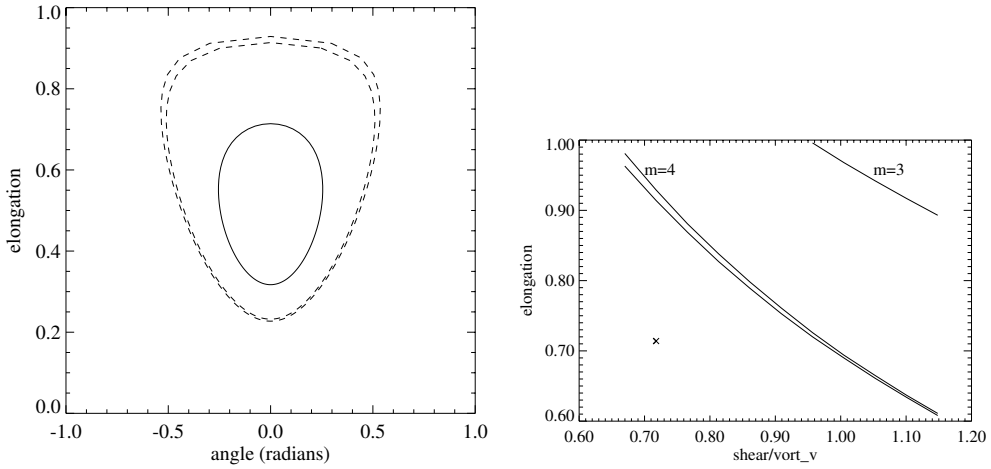

Figure 4.8: The phase plane of the equivalent Kida vortex in which the angle and elongation of the vortex is indicated by the drawn line. Linear stability analysis of nutating (and rotating) vortices (Meacham *et al.*, 1990) shows that there can be unstable bands in the phase plane. Only one band of instability was found for this case, a $m = 4$ mode, as is indicated by dashed lines. Next to it the unstable bands as a function of the ratio background shear to vortex vorticity are indicated (at zero angle). The cross denotes the present simulation.

stretch to form a thin line. Next, this line folds. The process of stretching and folding continues and leads to a very complicated distribution of tracers. After a while it gives rise to a distribution that looks fairly smooth. In that sense it is reminiscent of diffusion, although it is clearly a nonlocal phenomenon.

4.3.4 Dust and a vortex

Another interesting application of vortices is in planet formation (Tanga *et al.*, 1996; Bracco *et al.*, 1998; Bracco *et al.*, 1999). Dust particles interact with the gas by drag, but have no pressure. So the vortex gives them anti-cyclonic rotation on which the Coriolis force works. This concentrates the dust particles inside the vortex. In the context of accretion disks this was shown explicitly with an incompressible calculation (Bracco *et al.*, 1999). Here it is verified that the same process still works if 2D-compressibility is allowed for (Fig. 4.10). First, a well developed vortex is formed by running a simulation for 10 orbits around the compact object. Then 1000 passive tracers and dust particles are released at 1000 random positions in the disk (in the range $15 < r < 25$). The simulation is continued for another 10 orbits and the dust is advected with the same model as in Bracco *et al*. (1999) (the friction coefficient is proportional to the gas density divided by the particle radius: the Epstein regime). At the end the dust is seen to concentrate within the vortex while the passive tracers are still randomly distributed in the area of their release. Also note that the dust is distributed in a narrower band. This is probably related to the Coriolis force and the

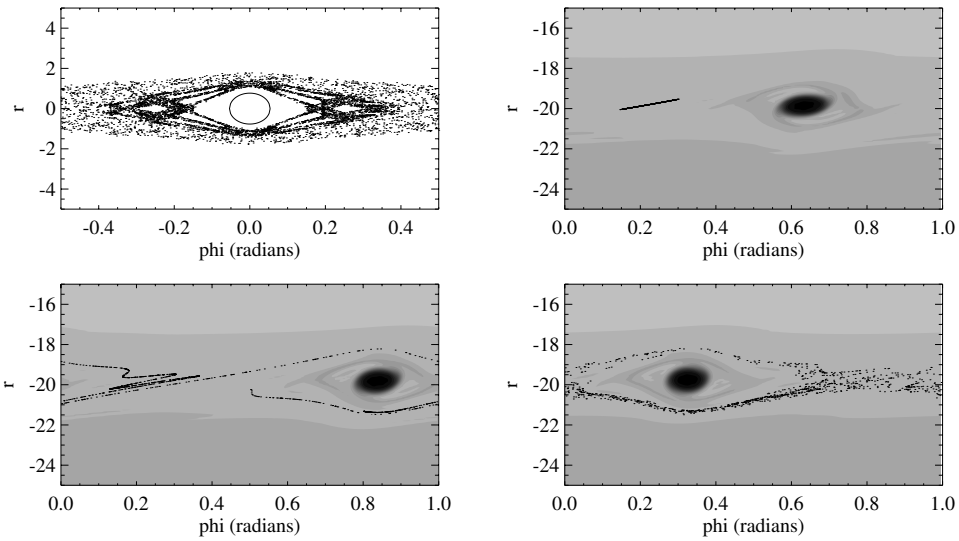

Figure 4.9: Top left: Poincaré section of surface of a passive tracer particle in the velocity field of a nutating Kida vortex. After every complete nutation the position of the tracer is plotted as a dot. The parameters of the Kida vortex are those determined from fitting the period of the nutation. The edge of the vortex is indicated by the solid line. The grayscale plots (potential vorticity range -2.13 to 1.56) are of a simulation in which 1000 passive tracers were advected with the flow. At t=10 $P_{\rm orb}$ the tracers were put in a very small area. After 1.91 orbits (3.3 nutations) the tracers are seen to have stretched to form a line (upper right). At t=14.78 $P_{\rm orb}$ (8.3 nutations) the line is seen to wrinkle (lower left) and at the end, 10 orbital periods (17 nutations) after the release, the tracers have spread over a considerable area (lower right).

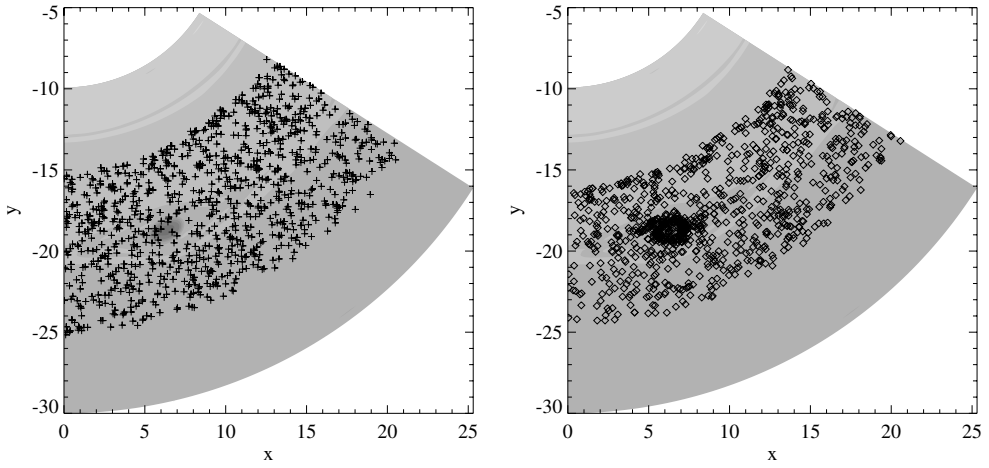

Figure 4.10: Passive tracers and dust particles are added to the simulation after 10 orbits around the compact object in a high resolution, low diffusivity run. The simulation is continued for another 10 orbits and the tracers and dust are advected by the fluid. It is observed that the passive tracers (left) are still randomly distributed within the area of release while the dust particles (right) that started at the same position as the tracers are concentrated in the vortex. This is identical to what happens in incompressible calculations, (Bracco *et al.*, 1999). The background grayscale is of potential vorticity (range -2.13 to 1.56).

velocity field between the "bow" and the "bore" (which are discussed in the next section). This mechanism might be relevant for the growth of planetessimals out of dust.

4.4 Interaction of vortex and surrounding

The results so far concern the vortex and its interior. However, plots of the surface density (Fig. 4.11) indicate that interesting structures appear outside the vortex as well. The vortex is accompanied by a large spiral shaped wave which is very prominent in surface density. Actually, the perturbations in surface density in the wave are larger than in the vortex. The wave is a low Mach number "shock" or "bore" in this 2D-polytropic model. The occurrence of this "bore" can be understood from the potential vorticity distribution (Fig. 4.12). The reason for using potential vorticity instead of the stream function is that the former shows small details much more clearly than the latter. The potential vorticity contours are almost parallel. Since potential vorticity is advected with the flow there is no flow through the parallel contours (in a stationary state): they form a kind of tube. On the upstream side of the "bore" a small-amplitude wavy perturbation is observed in potential vorticity. This is the nonlinear result of a gravity wave that acts as a "bow" wave coming from the front tip of the vortex (Fig. 4.11). This "bow" wave travels with the speed of sound and

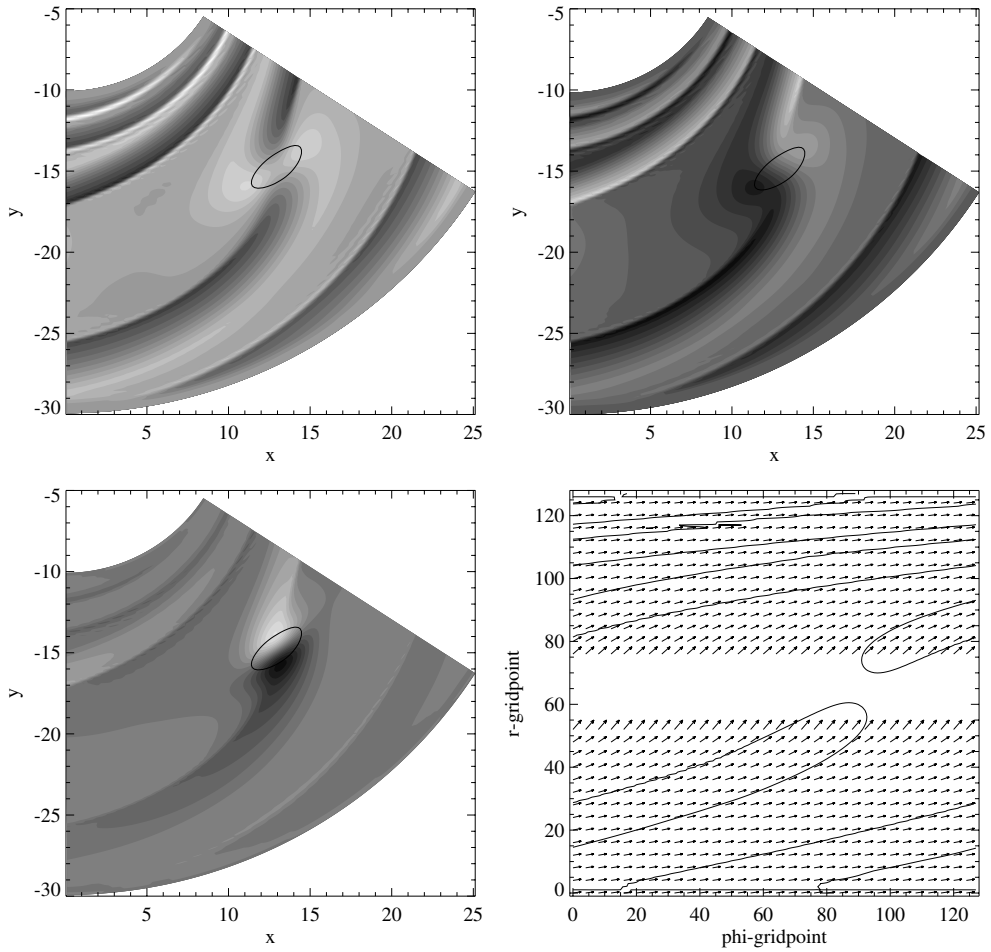

Figure 4.11: From left to right, top to bottom, the surface density (range 0.59 to 1.39), the radial velocity (range -1.1 to 0.77) and the azimuthal velocity minus the Keplerian velocity (range -0.76 to 0.73). Close ups have already been presented in Fig. 4.1. The vector plot compares the orientation of a density contour of the wave with the Mach angle and is in grid coordinates. The Mach angle is given by $\arcsin(c_s/v_k)$ where v_k is given by Eq. (4.3). It is indicated by the arrows. (The direction of the arrows is irrelevant.) The inner disk rotates counter clockwise.

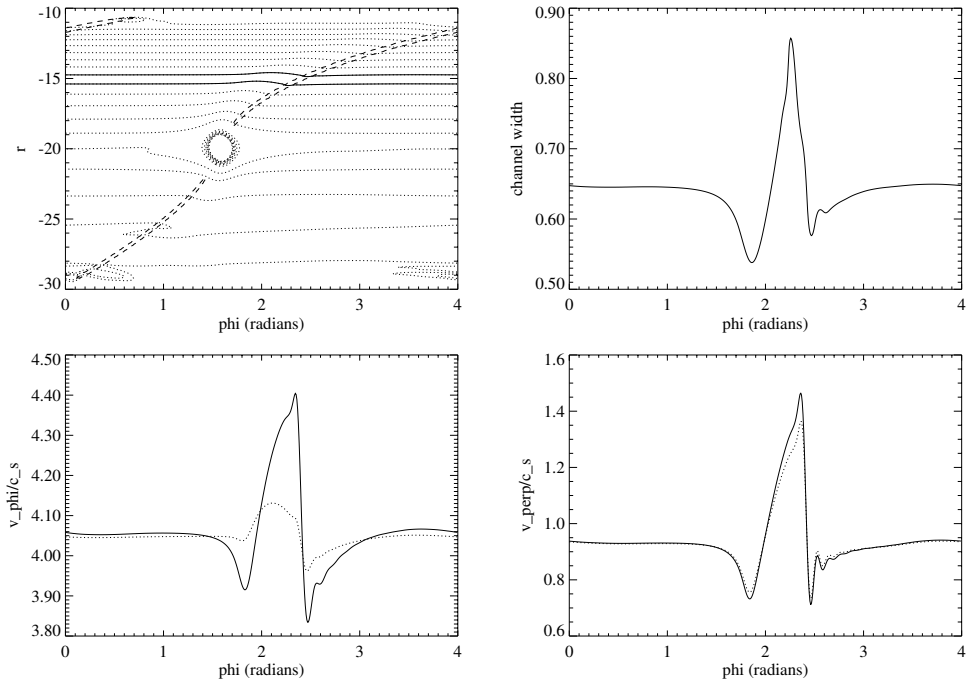

Figure 4.12: Potential vorticity contours (dotted) and the position of the "bore" (dashed) (top left). Two contours are highlighted as solid lines and form a flow channel. (These results are from a simulation on a larger domain and the data is compressed in the phi-direction to clearly show the wave in potential vorticity.) The width (along lines of constant phi) of this channel varies and forms a kind of converging-diverging nozzle (top right). The flow parallel to the phi-axis (at r=-15) is supercritical, first slows down in the converging part, and then accelerates in the diverging part (bottom left). The acceleration makes the velocity component perpendicular to the "bore" supercritical. Subsequently, this velocity component becomes subcritical and a "bore" occurs (bottom right). The dotted lines in the velocity plots are for the velocity normalized with the unperturbed speed of sound.

forms a kind of spiral arm in the supercritical shear flow. The angle of this "bow" wave with the Keplerian flow is just the Mach angle (Fig. 4.11). It is determined by the condition that the background flow speed projected onto the shock normal equals the speed of sound. The "bow" wave becomes more and more aligned with the azimuthal direction further away from the vortex. As a result the wavy potential vorticity perturbation at different radii shifts in the azimuthal direction, which leads to a kind of converging-diverging nozzle appearance in the contours. In the converging part, the supersonic (supercritical) flow slows down but in the diverging part it accelerates. Here the velocity component perpendicular to the "bore" attains supercritical values which are brought back to subcritical levels by the "bore". Note that since the "bore" stands under a similar angle as the "bow" wave, the "bore" has to be weak otherwise its propagation speed would exceed that of the "bow" wave which is its reason of existence. A fortunate incidental circumstance of the weakness of the "bore" (shock) is that the polytropic relation used in these simulations to replace the energy equation is a reasonable approximation for these shock strengths (Zucrow and Hoffman, 1976). The nozzle flow in the "bow" wave also provides insight into the intensification of the "bore" closer to the compact object. The potential vorticity contours are closer together and this seems to compensate for the smaller amplitude and increased wavelength of the wavy perturbation. Other spiral shocks (Spruit, 1987; Sawada *et al.*, 1987) are known to travel all the way towards the compact object.

The bore consists of sound waves traveling away from the vortex which is probably the source of the waves. This conjecture is based on Lighthill theory (Lighthill, 1978) (or in shallow water (Polvani *et al.*, 1994)) which describes sound generation by turbulent motion. Here it is hard to apply because flows are supersonic and the dispersion relation for sound waves in an accretion disk is only valid in a WKB sense (e.g. Binney and Tremaine, 1987). Anyhow, the source term of Lighthill radiation calculated in a coordinate system co-rotating with the center of the vortex is mainly confined to the vortex (and the "bores") and not its surrounding. The main contribution to the double divergence of the Lighthill tensor comes from the term $(\nabla \times \vec{v}) \cdot (\nabla \times \Sigma\vec{v})$ which is rather large inside the vortex. So we think that the sound waves originate from within the vortex and travel outward where they give rise to the "bow" wave and the "bore".

The back reaction of the waves on the vortex deserves closer inspection. The influence on the elongation of the vortex and on the measured orientation have already been discussed in Sect. 4.3.2. Fig. 4.6 shows that an asymmetry develops in the flow even for small Mach number. In the famous problem of inviscid incompressible flow past a cylinder, fluid motion has such symmetry that there is no drag on the cylinder (d'Alembert's paradox). This condition is apparently broken for a vortex in a 2D-compressible accretion disk. As a result the "bow wave and bore" may exert a pressure force and torque on the vortex. These are the topics of the next two subsections.

4.4.1 Forces in the radial direction

Local balance of forces within the vortex was studied in Sect. 4.3.1. Here we study net forces on the vortex as a whole. First radial forces are discussed.

Suppose there is a net radially outward force on the vortex. As a result, the vortex will move outward in the radial direction. As its angular momentum is conserved an increasing deficit builds up in the centrifugal force (proportional to r^{-3}) with respect to the gravitational force ($\propto r^{-2}$). The vortex settles at a radial distance where this deficit is just balanced by the initial force. So the way in which a net radial force shows up is not so much by the small radial displacement (for the simulation discussed below the radial displacement would be of order 5 percent of the initial vortex radius), but by an azimuthal drift of the vortex with respect to the local Keplerian velocity. This is indeed observed as Fig. 4.13 shows. The vortex lags behind with respect to the local Keplerian velocity. The drift velocity is small, $0.015c_s$.

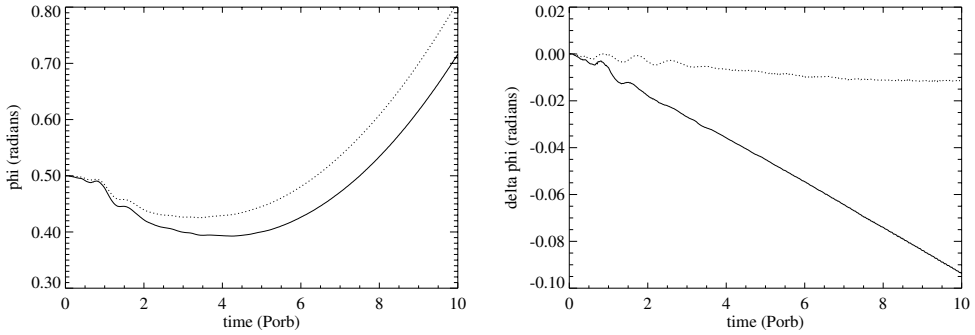

Figure 4.13: The azimuthal position of the vortex as a function of time (solid) and the position it would have had if it was advected with the local Keplerian velocity (dotted). Next to it the difference of these two positions as a function of time. The dotted line is the difference of a vortex in a β-free disk.

The radially outward force that works on the vortex has not been specified. To determine its nature the radial momentum equation is integrated over the area A of the vortex (in an inertial frame):

$$\frac{\partial}{\partial t}\iint \Sigma v_r dA + \iint \left(\nabla\cdot(\Sigma v_r \vec{v}) - \Sigma\frac{v_\phi^2}{r}\right) dA = \\ -\iint \left(\frac{\partial P}{\partial r} + \Sigma\frac{\partial \Phi_G}{\partial r}\right) dA. \tag{4.6}$$

Because the edge is defined as a potential vorticity contour which advects with the flow the divergence of the flux does not contribute (if the flow is stationary). Eq. (4.6) can be considerably simplified by introducing the velocity minus the local Keplerian

velocity ($v_\phi = v_{\rm kep} + \tilde{v}_\phi$):

$$\frac{\partial}{\partial t}\int\int \Sigma v_r dA = \int\int \left[\Sigma\left(2\tilde{v}_\phi\sqrt{\frac{GM}{r^3}} + \frac{\tilde{v}_\phi^2}{r}\right) - \frac{\partial P}{\partial r}\right] dA.$$

On the right we recognize the Coriolis, centrifugal and pressure forces.

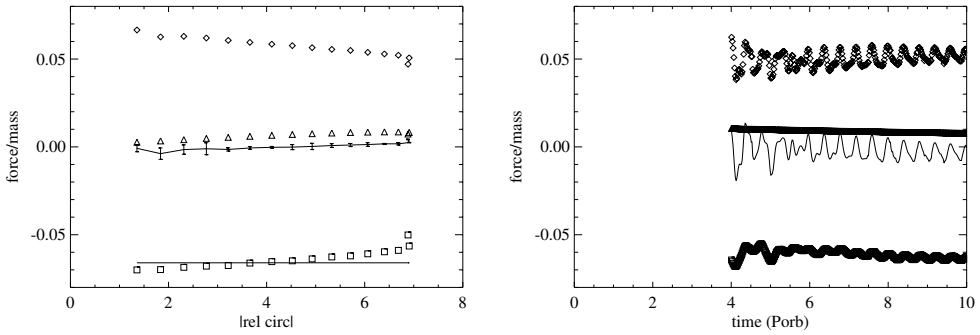

Figure 4.14: The non-dimensional pressure (diamonds), centrifugal (triangles) and Coriolis (squares) force divided by mass as a function of relative circulation $\oint \tilde{\vec{v}} \cdot d\vec{l}$. This represents a cross section through the vortex. The line gives the sum of the three forces. All three forces were calculated on two (staggered) grids, which gives the opportunity to determine something like an (three sigma) error. The lower solid line is the Coriolis acceleration that results from the azimuthal drift speed of the vortex. Next to it are shown the three forces and their sum as a function of time for one specific value of the relative circulation.

For a number of different potential vorticity contours these three forces were measured together with the mass and relative circulation within that contour (Fig. 4.14). The relative circulation plays the role of radius to the vortex center. We observe an outwardly directed pressure force and a very small centrifugal force which are balanced by in inwardly directed Coriolis force. Just at the edge of the vortex the balance of forces is lost. The observed Coriolis acceleration is largely explained by the azimuthal drift of the vortex (Fig. 4.13). Fig. 4.14 shows that there is a slight variation with circulation in the Coriolis force. This must be the result of the β-effect (the radial dependence of the Coriolis parameter $\Omega = \sqrt{GM/r^3}$) because if the Coriolis parameter is approximated to be constant over the area of the vortex, then the Coriolis force is $2\Omega \int\int \Sigma \tilde{v}_\phi dA = 2\Omega M_{\rm v} v_{\rm drift}$ for a steady drift ($M_{\rm v}$ is the mass of the vortex). In Fig. 4.14 this would be a horizontal line.

The three forces as a function of time are shown in Fig. 4.14 (on the right). The data of the initial adjustment phase was left out. The forces balance each other reasonably well. What is left is an oscillation. The oscillation period is that of the nutation (Sect. 4.3.2). This oscillation in net radial force results in radial fluctuations in the vortex position, but these are of very small amplitude and can not be observed (Fig. 4.17).

A kinematic approach explains the physical origin of the drift: after all, potential vorticity is advected by the local flow. A parameter study (see below) and experiments in β-free disks (Fig. 4.13) indicate that the gradient in background vorticity is an essential element of the explanation. Vortices on β-planes have been extensively studied in the oceanic (Cushman-Roisin *et al.*, 1990) and meteorological (Shapiro and Ooyama 1990; Smith and Ulrich 1993, and references therein) literature and have shown to develop a westward drift owing to the interaction of the vortex with the surroundings. This can be either due to Rossby wave emission (Shapiro and Ooyama, 1990) or the advection of the background vorticity: β-gyres (secondary vortices) (Smith and Ulrich, 1993). The latter occurs here. The Keplerian flow has to bend around the vortex. So potential vorticity that is initially at the same radius (but different ϕ-coordinate) as the vortex center at $r = R$ is displaced radially to $r = R \pm L$ when it is at the same ϕ-coordinate as the vortex. Since potential vorticity is materially conserved this induces relative vorticity anomalies (β-*gyres*) of order $\pm\beta L = \pm 3\Omega L/2R$ to the north and south of the vortex (Fig. 4.15). (The north, characterized by high background potential vorticity, corresponds in an accretion disk to the compact object). To the north a negative anomaly develops because the Keplerian contribution to potential vorticity is positive. This effect is strengthened by the divergent velocity field. In the south a positive anomaly develops (low Keplerian potential vorticity) which is weakened a bit by the divergence. The resulting dipolar vortex advects the monopolar vortex to the west with a speed that can be approximated from the circulation (Γ) of one dipole half $v_{\rm drift}/c_{\rm s} \approx \Gamma/(2\pi 2Lc_{\rm s}) = 0.0147$. This is in good agreement with the observed drift rate of $0.015c_{\rm s}$. For other simulations the correspondence is worse, a factor of two difference is quite common. A possible reason for this is that the monopolar vortex contributes to the dipole if the center of the monopole is slightly misplaced. Such apparent gyres are known as α-*gyres* or the

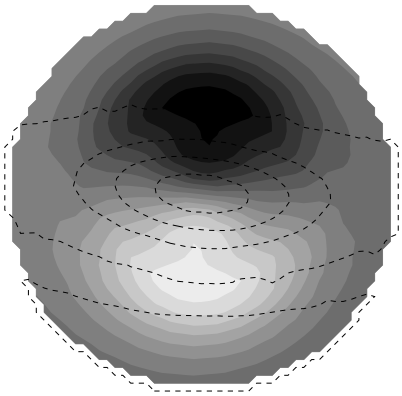

Figure 4.15: The m=1 mode of the relative non-Keplerian vorticity (range -0.07 to 0.07). The vorticity minus the Keplerian contribution is filtered to give the m=1 mode on circles around the vortex center. The dashed contours are of potential vorticity just like in Fig. 4.1. The contours extending out of the gray area are an artifact of the plotting routine.

"pseudomode", and they would give an unphysical contribution to the dipole. Also the determination of the propagation speed of the dipole by its circulation and size is just an estimate.

The drift was also determined at other values for the dimensionless parameters. The explanation above, with β-gyres, suggests that the drift scales as:

$$\frac{v_{\rm drift}}{V} \propto \beta L \frac{LL_{\rm D}}{VL} \propto \frac{1}{{\rm M_a R_S}},$$

the vorticity anomaly times the area of the gyres divided by the distance between the gyres. The area of the gyres is proportional to the size of the vortex (along the edge of the vortex) times the Rossby radius of deformation $L_{\rm D} \equiv c_{\rm s}/\Omega$ (perpendicular to the edge of the vortex). The one over radius dependence is indeed found (Fig. 4.16). The dependence on Mach number is more fuzzy (Fig. 4.16b). The bad value at the right in Fig. 4.16b is due to β-gyres that are larger than the domain of simulation. So it is concluded that the spiral waves play only a minor role in determining the azimuthal drift speed, which is largely due to β-gyres.

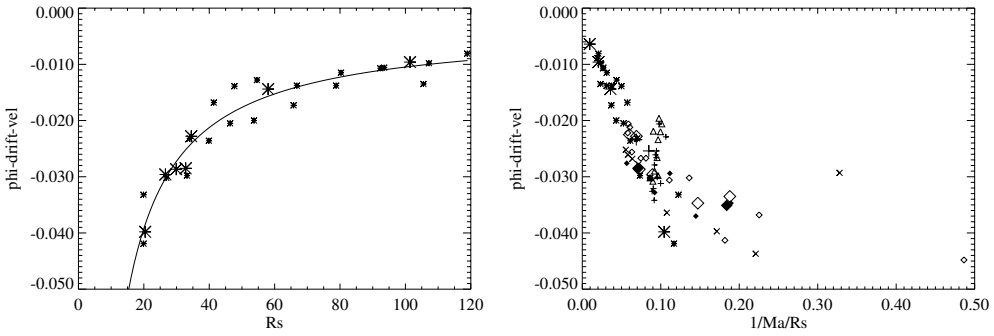

Figure 4.16: The dimensionless drift speed as a function of the distance $\rm R_S$ to the compact object. The line is the fit $-0.0033 - 0.718/\rm R_S$ and large symbols indicate high resolution runs. Next to it the dimensionless drift as a function of $1/(\rm M_a \cdot R_S)$.

4.4.2 Forces in the ϕ-direction, torque

Consider what happens to a vortex when there is a net azimuthal force working on it. A torque arises which extracts orbital angular momentum from or adds it to the vortex. As a result the vortex moves to smaller or larger radii (so it moves perpendicular to the applied force) (Fig. 4.17).

Another possibility is that fragments of the vortex break off. If the fragments carry excess angular momentum, then the bulk of the vortex loses angular momentum and moves to smaller radii. Possibly this occurs in the high resolution, low diffusivity simulation but in the low resolution simulations there is little observational support for this hypothesis.

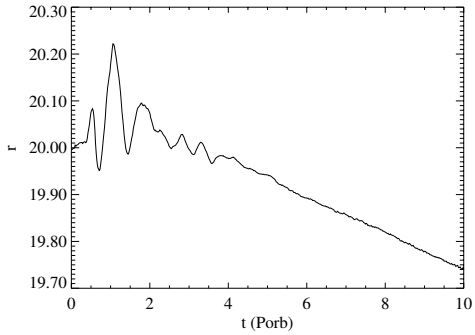

Figure 4.17: The radial position of the vortex center as a function of time. After an initial adjustment phase which lasts for some four orbital periods, the vortex drifts to smaller radii.

Let us therefore consider radial transport by applying an azimuthal force to the vortex. The only force capable of doing this is the pressure gradient as follows from integration of the equation of conservation of angular momentum (in an inertial frame) over the area of the vortex:

$$\frac{\partial}{\partial t}\int\int \Sigma r v_\phi dA + \int\int \nabla\cdot(\Sigma r v_\phi \vec{v}) dA = -\int\int \frac{\partial P}{\partial \phi} dA. \tag{4.7}$$

As boundary of the vortex a potential vorticity contour is used. Since potential vorticity is advected by the flow there is no flow through the boundary so the divergence term on the left is zero (if the flow is stationary). This leaves only the pressure as a mechanism to extract angular momentum from the vortex. To good approximation (within a few percent) the angular momentum consists of orbital angular momentum so that $\int\int \Sigma r v_\phi dA \approx r_{\rm c} v_{\phi{\rm c}} \int\int \Sigma dA = M_{\rm v} r_{\rm c} v_{\phi{\rm c}}$, where index $_{\rm c}$ indicates quantities at the vortex center. This allows a considerable simplification of Eq. (4.7):

$$M_{\rm v}\frac{\partial r_{\rm c} v_{\phi{\rm c}}}{\partial t} = -\int P|_{\phi_1}^{\phi_2} r dr, \tag{4.8}$$

where conservation of mass was used and the right hand side is an integral over the vortex boundary.

Inspection of the pressure (or surface density) distribution on a potential vorticity contour in Fig. 4.18 (see also Fig. 4.11 and Fig. 4.1 for a close-up), shows that there are indeed azimuthal pressure gradients. Low pressure areas that typically occur when flow deflects around a body, are shifted in the downstream direction, breaking the symmetry of reversible flow (as in d'Alembert's paradox). Consider two points at the same radius (to the compact object), one in quadrant I and the other in II. For most points the pressure in quadrant II is higher than that for the corresponding points in quadrant I. So at the inner side of the vortex the pressure distribution pushes the vortex in the positive ϕ-direction: it gives angular momentum to the vortex. In quadrants III and IV the opposite occurs. The pressure field exerts a force in

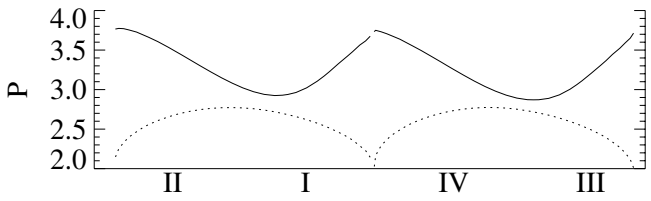

Figure 4.18: The dimensionless pressure along a closed potential vorticity contour. The vortex is cut in two halves and its shape is indicated by the dotted line. The horizontal axis is a proxy for the ϕ coordinate of the vortex and runs up and then down the vortex. Indicated are the quadrants in which the vortex is divided. Keplerian flow is from left to right.

the negative ϕ-direction: angular momentum is lost by the vortex to the external pressure field. The downstream shift in the pressure minimum is probably partly due to the emission of sound waves (Lighthill radiation) which was discussed in Sect. 4.4. If this is able to explain all of the shift is not known. The pressure forces on inner and outer edge of the vortex are of comparable magnitude. However, the arm to the outer edge is larger so that the vortex as a whole loses angular momentum to the external pressure field.

This process explains the inward motion seen in Fig. 4.17. For a number of different potential vorticity contours the mass and the right hand side of Eq. (4.8) are measured (Fig. 4.19). The slope of this relation gives the loss of specific angular momentum. The solid line indicates the loss of specific angular momentum measured directly from the radial position and azimuthal velocity (Fig. 4.17). Within the errors there is agreement except for the outermost potential vorticity contour. The pressure torque fluctuates in time around a small positive value after the adjustment phase (Fig. 4.19). The oscillation frequency is that of the nutation (Sect. 4.3.2).

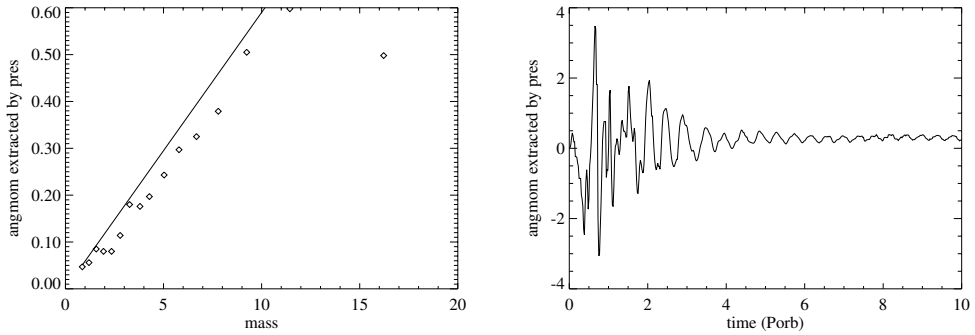

Figure 4.19: The pressure-torque as a function of mass. The solid line is the loss of specific angular momentum determined from the radial position and azimuthal velocity. The diamonds are determined from the right hand side of Eq. (4.8). Next to it the pressure-torque as a function of time for one mass value.

The simulation shown above turned out to be somewhat special. The simple mechanism of net angular momentum loss due to the difference in radius between inner and outer edge of the vortex doesn't hold for all simulations at other parameter values. If there is a net pressure force working on the vortex then this leads to additional angular momentum loss or gain as a splitting up of the right hand side of Eq. (4.8) shows:

$$-\int P|_{\phi_1}^{\phi_2} r dr = -\int P|_{\phi_1}^{\phi_2} (r - r_c) dr - r_c \int P|_{\phi_1}^{\phi_2} dr.$$

The last term on the right describes the effect of a net pressure force on the vortex while the first term is mainly due to the difference between inner and outer edge of the vortex. Quadrupolar sound wave emission could contribute to the first term but not to the second. Measurements show that the first term always extracts angular momentum and satisfies well behaved relations (Fig. 4.20). It is approximately linear in Mach number due to the intensification and downstream shift of the minimum in pressure with increasing Mach number, and is actually related to the vertical aspect ratio of the vortex $L/H = \sqrt{\gamma}\mathrm{Ma}/\mathrm{R_O}$. The variation with Rossby number shows a minimum around $\mathrm{R_O} \approx 1$ and goes to zero for small and large Rossby number. The decrease with large Rossby number is just another manifestation of the dependence on vertical aspect ratio. The decrease for small Rossby number results from approaching geostrophic balance, so that streamlines approach isobars. There is no dependence on $\mathrm{R_S}$.

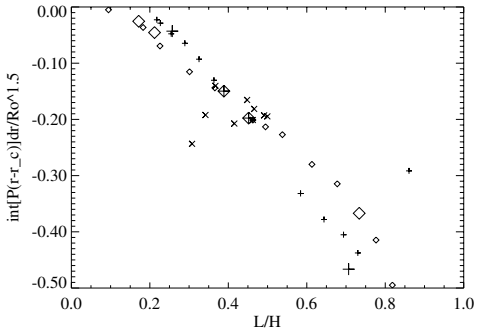

Figure 4.20: The part of the pressure torque not due to a net pressure on the vortex divided by the Rossby number to the power 1.5 as a function of the aspect ratio of the vortex. The meaning of the different symbols is explained in Fig. 4.5. Large symbols indicate high resolution runs.

The net pressure term shows much more scatter, it can extract from or add angular momentum to the vortex and it varies (with the nutation period?) in time. The net effect of this term can be larger than that of the first term. No clear dependence on Mach number has been found. Possibly the effect increases with increasing Rossby number, being about zero at $\mathrm{R_O} \approx 1$ and perhaps there is a dependence on $\mathrm{R_S}$. This term is found to be very sensitive to changes in numerical parameters such as boundary conditions and resolution. If the effect is of physical origin (which is

uncertain), a possible explanation may be found in the shape of the vortex. One might think that, at low Rossby number, aerodynamic streamlining of the vortex is better on the inner (north) side of the vortex where the non-uniform Keplerian shear is stronger, than at the outer edge. So this implies an increased loss of angular momentum. At larger Rossby number the aerodynamic streamlining is lost, implying a similar shape at inner and outer edges. Now the stronger shear at the inner edge makes the vortex gain angular momentum.

To summarize, the radial motion of the vortex is governed by a net pressure torque. What determines the pressure torque is only partly understood. The breaking of d'Alembert's paradox, probably partly due to quadrupolar sound wave emission, combined with the larger distance to the outer edge of the vortex only determines part of the pressure torque. Another contribution may perhaps be due to changes in the shape of the vortex. Also the β-gyres may contribute to a net pressure on the vortex if they are tilted away from the north-south position.

The change in angular momentum of the vortex results in a radial displacement. For comparison, the radial velocity can be expressed with the help of standard thin disk theory (Pringle, 1981) in the form of an effective alpha:

$$\alpha_{\rm eff} = \frac{\nu\Omega}{c_{\rm s}^2} = -\frac{2}{3}\frac{v_{\rm kep}}{c_{\rm s}^2}v_r \approx \frac{4}{3}\frac{1}{c_{\rm s}^2}\frac{dr v_\phi}{dt}.$$

The variation of $\alpha_{\rm eff}$ with Mach number is shown in Fig. 4.21. Quite respectable velocities seem possible. However, caution is required in interpreting $\alpha_{\rm eff}$ as α given by conventional mass transport. First, since a polytropic relation is used the surface density scale drops from the equations so real mass transport can be made as large as one wants. Second, only one vortex (per sector) was superimposed so only a small fraction of the total disk is involved in inward transport. Third, while the vortex looses angular momentum there must also be material that gains it. This material flows outward reducing the net inward mass transport. If the angular momentum is gained by matter close to the vortex, then α is lowered by one or two orders of

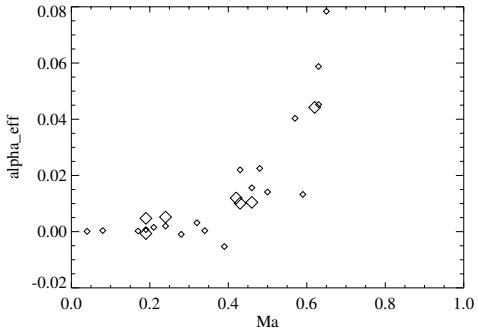

Figure 4.21: The effective α as a function of Mach number. Large symbols indicate high resolution runs.

magnitude. If, however, waves transport angular momentum to the outer edge of the disk then there is no reduction at all. It is hard to settle this by measurements because of the smallness of the effect. Angular momentum fluxes give a slight indication that it is material in the direct neighborhood of the vortex that is involved in angular momentum transport and this would make sense because it seems logical that the wake of the vortex is filled up.

Apart from mass transport by displacement of the vortex, an other form of mass transport might result from the bore. This is the first topic of the discussion.

4.5 Discussion and conclusion

The main goal of this research was to determine transport properties in 2D-disks owing to vortices. Different transport mechanisms were encountered:

- The "bores". The vortex excites waves in the surrounding flow which lead to spiral bores. If the full energy equation had been used, they would be low Mach number shocks to which the calculations of Spruit (1987) apply. Dissipation in these shocks would lead to loss of angular momentum and inward transport of mass in that part of the disk that is in between the vortex and the compact object because here the waves contain negative angular momentum. Matter would gain angular momentum and mass would be transported outward at radii larger than that of the vortex because of the positive angular momentum of the waves in this region. All other transport mechanisms relate to mass within or on the edge of the vortex, while this mechanism affects even mass that is far away from the vortex. The disadvantage of this type of accretion is that it is not very efficient; high values for α can not be explained in this way because of the weakness of the shocks.

- Breaking of d'Alembert's paradox. Apart from the excitation of the "bow wave" and the "bore", the pressure field also shows a downstream shift of the pressure minimum on the edge of the vortex. This is perhaps due to the emission of sound waves (and in that way linked to the previous observation) in which case a term like wave drag would be appropriate. It breaks the symmetry responsible for d'Alembert's paradox. As a result, pressure torques act on the vortex. Because of the larger distance to the outer edge of the vortex, some vortices are seen to lose angular momentum and move to smaller radii. This type of accretion is also inefficient because only a small fraction of the disk moves inward and the material that receives the angular momentum from the vortex moves outward.

- Beta-gyres. It was shown that β-gyres are responsible for the azimuthal drift (Sect. 4.4.1) and from terrestrial vortices we know that they can also lead to a north-south drift component which is the radial direction in an accretion disk. The orientation of the β-gyres observed in Fig. 4.15 are indeed such that a small

drift of the vortex towards the compact object would occur. However, this depends sensitively on the position of the vortex center. Since this is not accurately known, the contribution of the erroneous α-gyres to the β-gyres is uncertain and this makes it impossible to estimate the small radial velocity owing to the β-gyres. A rough upper limit would be that it is an order of magnitude smaller than the azimuthal velocity, but it could be zero just as well. Also, the scaling with the dimensionless parameters gives no clue as to whether β-gyres contribute to radial motion.

- Instabilities in the Kida vortex which lead to filamentation. Nutating and rotating Kida vortices in shear flow are known to be unstable in the right parameter regime (Meacham *et al.*, 1990). The one vortex that was investigated turned out to be in a stable part of parameter space. However vortices were found to move in the radial direction, which brings them to locations where a different background shear exists. Radially inward motion also leads to a larger contribution of "planetary vorticity" (the Keplerian contribution) to potential vorticity so probably the relative vorticity of the vortex decreases (the anti-cyclonic vortex gets stronger). The decrease in relative vorticity is slower than the change in shear so the net effect will be motion of the vortex towards the m=4 instability strip in Fig. 4.8. Upon reaching this strip vorticity filaments will be shed. As a result, the remnant of the vortex might undergo some further radial transport (Meacham *et al.*, 1990). To test this hypothesis much more prolonged simulations are needed than the ones shown here, where the radial motion of the vortex was observed to be small so that the change in background shear was accordingly negligible. Another consequence of this process would be that after going through several unstable zones the vortex is eventually dissipated.

- Chaotic advection around a nutating Kida vortex. It was observed that a passive tracer can spread rapidly over a considerable area owing to a nutating vortex (Fig. 4.9). Chaotic advection works as long as there is some periodicity in the flow field and the perturbations are large enough. This phenomena not only works with passive tracers but also on active tracers (Pierrehumert, 1991) such as potential vorticity. Chaotic advection homogenizes potential vorticity which is observed around for example Neptune's Great Dark Spot (Polvani *et al.*, 1990). The conceptual difficulty with active tracers is that their advection acts back on the velocity field, possibly destroying the source of chaos. Similar trouble arises for mass and angular momentum. Things are even worse, they are not only active tracers but they can also be transported by non-advective processes. However, it is not clear to us that the process of chaotic advection can be neglected in the determination of transport in accretion disks.

- Rossby wave emission. This is one of the primary transport mechanisms for vortices on earth and eventually leads to their destruction. The previously mentioned instability of the Kida vortex and subsequent filamentation is actually a special form of this. The process is important when the dimensionless gradient in the background potential vorticity is larger than unity. Expressed

in non-dimensional numbers the condition is:

$$\frac{\beta L^2}{V} = -\frac{3}{4}\frac{\Omega L^2}{RV} = -\frac{3}{4}\frac{1}{\mathrm{R_o R_s}} \gg 1, \tag{4.9}$$

from which it is clear that vortices in accretion disks can hardly be in this regime. Accordingly, the simulations gave no indication of this process to occur. An additional reason for the lack of Rossby wave emission could be the potential vorticity homogenization of the background by chaotic advection. On the other hand, while the vortex moves to smaller radius it must break through potential vorticity contours set by Keplerian rotation (see e.g. Fig. 4.12a). This involves a reconnection like process in which Rossby waves are bound to be emitted.

Apart from the question of transport, vortices might also be of interest for explaining certain observations. For example, the time variability of photometric observations is perhaps related to a collection of vortices in the disk. An early suggestion (Abramowicz *et al.*, 1992) was that vortices would form bulges on the disk. Our simulations indicate that this is only marginally true. The variations in surface density of the accompanying "bore" are much larger that the variations within the vortex.

Finally it is verified that dust particles tend to concentrate in vortices (Tanga *et al.*, 1996) also is a 2D-compressible calculation which is interesting from the point of view of planet formation.

Acknowledgements. MDN likes to thank Dr. E. Neven for many helpful comments and Dr. M. Montgomery for sharing his insights on vortex motion.

Appendix: Raw data

On special request some raw data is presented in Fig. 4.22, as if there are not enough pictures in this chapter already. Personally I think it is superfluous, but if I don't fill this page it will be blank. This is not part of the submitted publication.

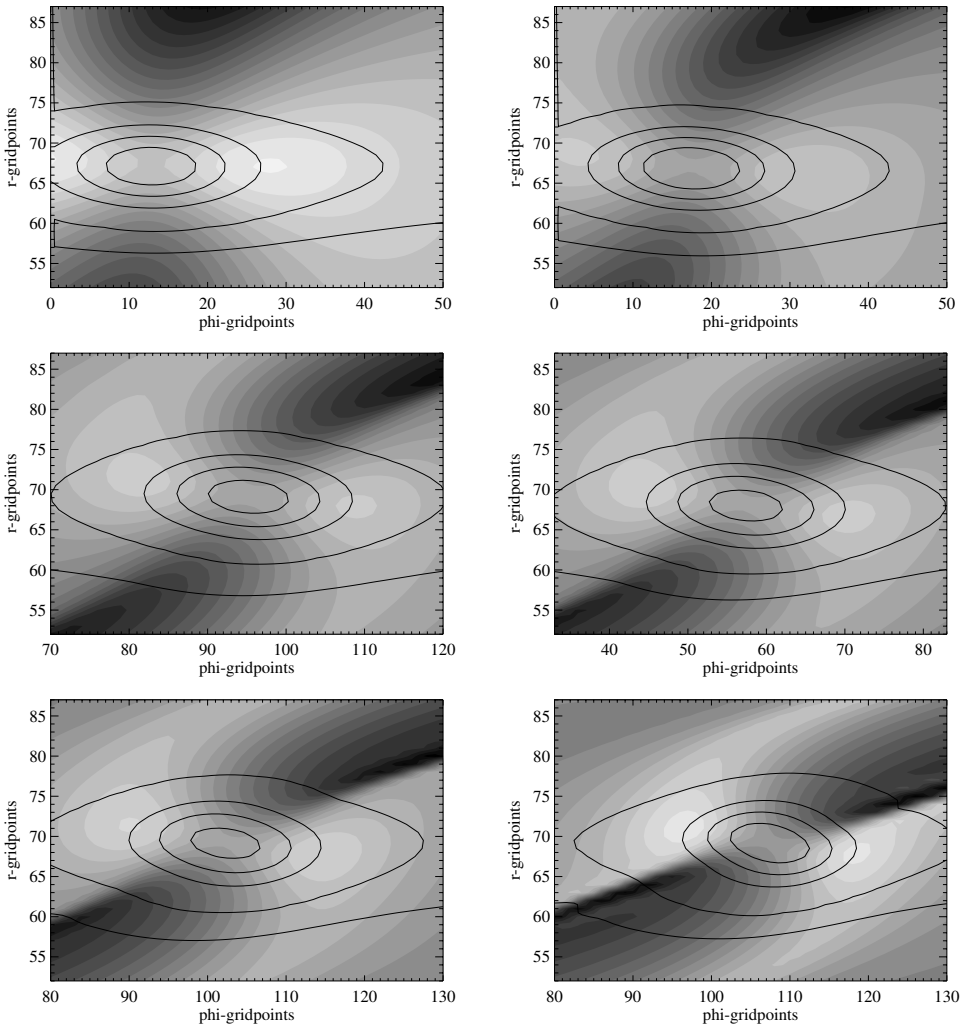

Figure 4.22: The surface density distribution for simulations with (initial) Mach numbers: 0.2, 0.3, 0.5, 0.6, 0.7 and 0.9. The third one is the standard vortex. The superimposed contours are of potential vorticity (levels: -1, -0.5, 0 and 0.5) and the grayscale consists of 21 equidistant filled density contours running from: $1 \pm (\mathrm{M_a} - 0.15)$.

Chapter 5

Two-Dimensional Vortex Dynamics in an Accretion Disk

Abstract. We extend previous work on two-dimensional vortices in accretion disks (Nauta *et al.*, 2000). A single vortex is studied not with a polytropic equation of state but the energy equation is solved together with the continuity and momentum equations. The results turn out to be similar to what was already known from a single vortex in a polytropic disk. Further, interactions of several vortices are studied in a polytropic disk. This can take the form of vortices interacting with the bore of an other vortex, or merging of vortices if they get really close together. The first leads to a somewhat faster decay of the circulation of the vortices but otherwise is of little consequence. Merging was found to lead to large losses of circulation while the drift velocity of the vortices is not much affected. The main conclusion is that vortex interactions do not enhance radial transport of mass significantly over that of individual vortices.

5.1 Introduction

With the realization that a magnetohydrodynamic (MHD) instability occurs in accretion disks (Balbus and Hawley, 1991) and the subsequent verification that it leads to turbulence and an MHD dynamo, efficient transport of mass and angular momentum through an accretion disk seems almost explained (for a review see e.g. Balbus and Hawley (1998)). Still a purely hydrodynamical explanation would be of interest, for example in cases where the degree of ionization is too low to couple the magnetic field to the gas. Also, it could learn us about fundamental fluid-dynamical principles of accretion disks that are more difficult to obtain from MHD calculations.

One suggestion, based on the hydrodynamics of planetary atmospheres and oceans, is that long-lived two-dimensional (2D) vortices would occur in an accretion disk (Abramowicz *et al.*, 1992). Such vortices form automatically out of random motion in 2D-turbulent flows (e.g. McWilliams, 1984) and it is thought that similar processes occur in the earth's atmosphere and oceans. The reason is that large-scale fluid dynamics in these systems is quasi-2D because the fluid layer is thin, in hydrostatic equilibrium and the Rossby number (measuring the importance of the nonlinear term in the momentum equation with respect to the Coriolis force) is small so that fluid motion is forced to move in columns parallel to the rotation axis (the Taylor-Proudman theorem). Similar conditions might be expected in an accretion disk but it was argued that, because of the supersonic Keplerian shear flow, vortices in an accretion disk can not grow larger than the thickness of the disk and that the Rossby number of vortices in accretion disks is of order unity or larger (Nauta, 2000). This makes it not very likely that long-lived 2D-vortices develop spontaneously in a disk.

However, if a 2D-vortex is somehow created with large enough Rossby number and a size smaller than the thickness of the disk, then it can persist over a considerable period of time. Other work that demonstrates this phenomenon are (mostly incompressible) simulations by Bracco *et al.* (1998,1999) and simulations of Godon and Livio (1999) on the effect of α viscosity on vortices in protoplanetary disks. The dynamical behavior of a single 2D-vortex in a *polytropic* disk was the subject of a previous study (Nauta *et al.*, 2000). Here this study is extended. After a brief summary of the equations and their numerical method of solution in Sect. 5.2, we first study a single vortex in an accretion disk where we extend the equations with the energy equation (so no polytropic equation of state is imposed) in Sect. 5.3. It appears that the results do not differ much from what was found in the previous article. Next, the interaction of two vortices is investigated in a polytropic disk in Sect. 5.4. Depending on the radial distance of the vortices two kinds of interaction are possible. If the vortices are well separated, they interact with the bore excited by the other vortex. If they get close together, then the vorticity distributions of both vortices interact and if they get close enough they merge. A discussion of three vortices is presented in Sect. 5.5 and that of multiple vortices in Sect. 5.6. Finally, the conclusion is given in Sect. 5.7.

5.2 The equations and their implementation

The polytropic gas equations are solved numerically in 2D with what is in essence a shallow-water code (Arakawa and Lamb, 1981) that has been used, among others, to study the Great Red Spot on Jupiter (Dowling and Ingersoll, 1989). Only a minor modification is required to handle 2D polytropic gas dynamics (Nauta and Tóth, 1998). The dimensionless form of the equations is (Nauta *et al.*, 2000):

$$\frac{\partial \Sigma}{\partial t} + \nabla \cdot \Sigma \vec{v} = 0, \tag{5.1}$$

$$\frac{\partial \vec{v}}{\partial t} + (\vec{v}\cdot\nabla)\vec{v} + \mathrm{R_o^{-1}} 2\hat{z} \times \vec{v} = -\mathrm{M_a^{-2}} \frac{1}{\gamma\Sigma}\nabla P + \mathrm{R_o^{-2}}\nabla\left(\frac{\mathrm{R_s^3}}{r} + \frac{r^2}{2}\right), \tag{5.2}$$

$$P = \Sigma^\gamma, \tag{5.3}$$

where $\vec{v}$ is the dimensionless 2D-velocity, Σ the surface density, P the (height integrated) pressure, r the distance to the compact object and γ the adiabatic index. In the scaling procedure we have used the radius of the vortex (L) as a length scale and the rotation velocity of the vortex (V) as a velocity scale. Three dimensionless parameters determine the solution:
The Rossby number:

$$\mathrm{R_o} = V/(\Omega L), \tag{5.4}$$

where Ω is the rotation rate of the coordinate system (which is the Keplerian rotation rate at a dimensional distance R from the compact object). Usually R is also the distance where the vortex is superimposed. All times will be expressed in orbital periods $2\pi/\Omega$.
The Mach number:

$$\mathrm{M_a} = V/c_\mathrm{s}, \tag{5.5}$$

and the dimensionless distance to the compact object:

$$\mathrm{R_s} = R/L. \tag{5.6}$$

Other dimensionless parameters can be constructed from these three, such as the thickness of the disk: $H/R = \mathrm{R_o}/(\sqrt{\gamma}\mathrm{M_a R_s})$. All simulations are done with $\gamma = 1.4$.

The numerical method is second order in space and we use the version that has fourth order accurate advection of potential vorticity if motion is incompressible (Takano and Wurtele, 1982). Calculations are stabilized with a hyperviscosity operator. Boundary conditions are periodicity in the ϕ-direction and absorption by a sponge layer (Martinsen and Engedahl, 1987) in the radial direction.

The initial condition consists of the Keplerian velocity profile to which a circular perturbation is added with $v \propto \xi \exp(-\xi^2)$ where ξ is the distance to the vortex center. The surface density is initially uniform.

5.3 A single vortex

In this section the interaction of a single vortex with a Keplerian flow is studied. On the one hand it extends previous work because we add an energy equation for an ideal gas:

$$\frac{\partial P}{\partial t} + \nabla \cdot P\vec{v} = (1-\gamma)P\nabla \cdot \vec{v}, \tag{5.7}$$

to the continuity equation Eq. (5.1) and the momentum equation Eq. (5.2) and do *not* enforce a polytropic relation between pressure and density Eq. (5.3). On the other hand it summarizes previous results because only minor differences with the preceding study were found.

The advantage of Eq. (5.7) is that all terms are of comparable magnitude. If instead the internal energy density is used as the independent variable, then the pressure would have to be determined from the difference between two large quantities which is prone to errors because the internal energy density is small in an accretion disk compared with the gravitational and (Keplerian) kinetic energy density. The price to pay for this primitive form of the equation is that shocks are not represented correctly, only conservative discretizations can do that. However, this objection holds already for our discretization of the momentum equation (see Arakawa and Lamb (1981) or Nauta and Tóth (1998)) so no extra inconsistency is introduced with Eq. (5.7). It is discretized in the same way as the continuity equation and in the right hand side the value of the pressure is taken at the cell center and the velocity components on the cell boundaries.

Initially the vortex is at $r = 20$, $\phi = 0.5$ and has $\mathrm{R_O} = 1.0$ and $\mathrm{M_a} = 0.5$ ($\mathrm{R_S} = 20$, $H/R = 0.085$). Simulations are done on a region of $10 < r < 30$, $0 < \phi < 1$ at a resolution of 256×256. The hyperviscosity is a Δ^2 operator with an e-folding time of 160 P_{orb} for waves with a wavelength which is the diameter of the vortex.

Since the initial condition is just a circular perturbation of the velocity field, there is no balance of forces so that the vortex goes first through an adjustment phase. This is followed by more regular behavior.

Neither the surface density distribution of the vortex nor the pressure has a monotonic profile. Rather they have saddle shapes. This is a consequence of the local balance of forces where in the radial direction pressure plus centrifugal forces oppose the Coriolis force and in the azimuthal direction centrifugal force counterbalances Coriolis and pressure forces. Because the supersonic Keplerian flow has to bend around the vortex compressible waves are excited. Especially the shock is prominent (Fig. 5.1). Close inspection shows that it is preceded by a compression similar to a bow wave. In between the bow wave and the shock there is a divergent flow region. The shock leads to a difference between the simulation with energy equation and the polytropic simulation (where we call the discontinuity a bore). The bore has no entropy change, it is reversible, and there is no heating of the gas, while with an energy equation the temperature does increase as Fig. 5.1 shows. Especially at the inner side where the shock is tightly wound, shock heating is clearly visible. Dissipation in the shock leads to accretion of matter at $r < r_{\mathrm{vortex}}$ while matter at

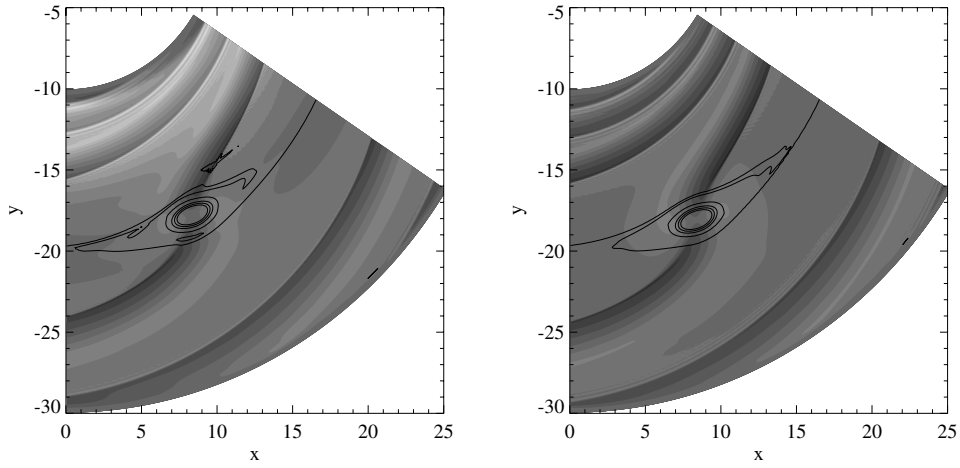

Figure 5.1: The temperature (P/Σ) after 10 orbits around the compact object. On the left is the simulation in which also the energy equation is solved and on the right is the polytropic gas simulation. The grayscale consists of 20 equidistant contours varying from 2 to 4. The overlying curves are potential vorticity contours (-1,-0.5,0,0.563).

$r > r_{\rm vortex}$ gains angular momentum (e.g. Larson, 1990). This might eventually form a ring of low density around the vortex as happens around protoplanets in protostellar disks. Apart from this difference in temperature, the spatial distribution of the other variables is alike.

The same holds for a close examination of the vortex. Fig. 5.2 shows that the vortex is nutating and changes its orientation and elongation periodically. The elongation is defined as the semi-major over the semi-minor axis (which is the inverse from what was used previously). It was found that this kind of behavior is well described by the Kida vortex model (Kida, 1981). We attribute the decrease in the amplitude of the oscillation (Fig. 5.2) to the hyperviscosity that is used. A suggestion in the literature (Marcus, 1990) that positive vorticity filaments would be responsible for the damping of the nutation could not be verified. The nutation in both simulations is similar. In the second half of the calculation the nutation period of the polytropic case increases and its amplitude decays faster compared to the simulation which solves the energy equation. Similar small changes are observed in the area of the vortex (2 percent larger in the polytropic case), the peak vorticity (a small 2 percent weaker in polytropic case) and the circulation (0.4 percent stronger in polytropic case).

The motion of the vortex as a whole is also similar for both calculations. The vortex drifts in the azimuthal direction. The explanation is that the zonal flow moves around the vortex during which absolute potential vorticity is advectively conserved. This creates relative vorticity anomalies that are called β-gyres. These advect the vortex in the negative ϕ-direction. Fig. 5.3 shows that this advection is of comparable magnitude for both calculations. Usually the drift is constant, but not in all sim-

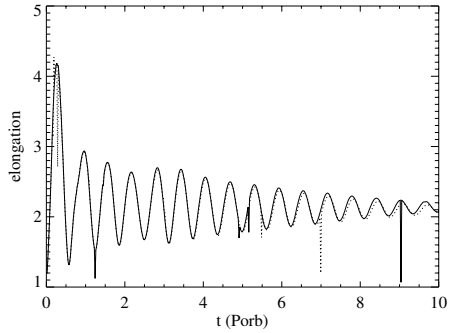

Figure 5.2: The elongation of the vortex as a function of time. The solid line is the simulation with energy equation and the dotted line is for the polytropic calculation. Occasionally the determination of the elongation fails and this gives rise to the spikes at for example $t \approx 9.1$ $P_{\rm orb}$.

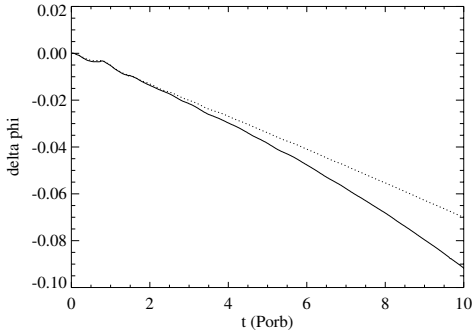

Figure 5.3: The ϕ-coordinate of the vortex minus the ϕ-coordinate if it was only advected with the local Keplerian flow. The azimuthal drift of the vortex is the slope of this graph. The meaning of the lines is as in Fig. 5.2.

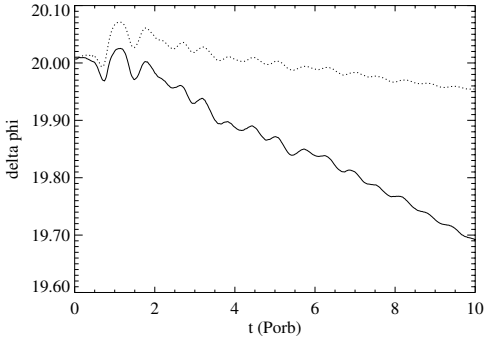

Figure 5.4: The radial position of the vortex as a function of time. The solid line is the ideal gas simulation and the dotted line is for the polytropic calculation.

ulations as Fig. 5.3 shows. Measurements of the circulation of the β-gyres are too uncertain to determine if they intensify or not.

The radial drift is an order of magnitude smaller that the azimuthal drift and Fig. 5.4 shows it for both calculations. It might seem as if there is a considerable difference between the two, but if we look at the spread found for various polytropic calculations (see Fig. 21 of Nauta *et al*. (2000)) then we do not think this difference is significant. The physical cause of this drift is only partly understood. There are pressure forces on the side of the vortex facing the compact object and away from it maybe due to the emission of sound waves. Even though the net force might be zero they can still extract angular momentum from the vortex because of its finite size.

To summarize, the difference between a vortex in a polytropic gas disk or in a disk where we also solve the energy equation is small. The main observable effect is the increase in temperature with the energy equation due to dissipation in the shocks.

5.4 Two vortices

After having studied a single vortex in a more realistic background flow, we return to the polytropic Keplerian disk with uniform surface density and study the interaction of two vortices. This problem has so many free parameters that we restrict the discussion to two vortices with, initially, the same size and internal velocity. The new free parameter (compared with a single vortex) is the impact parameter: the difference in radial position of the vortices. The relative Keplerian advection changes the azimuthal distance of the vortices periodically and can position them such that they interact. This can be either between one vortex and the bore of the other or direct interaction of the vortices with each other when they are close together. The latter can lead to merger as is known from vortices without background shear flow (e.g. Waugh, 1992). In this case, identical vortices merge only if their separation is

less than 3.2 vortex radii. Excess angular momentum is taken away by vorticity filaments. Similar behavior is expected in our simulations.

5.4.1 Large impact parameter

First the impact parameter is chosen so large that the vortices interact only with the bore excited by the other vortex. Vortex 1 starts at $r = 17.5, \phi = 1.0$ while vortex 2 is initially at $r = 22.5, \phi = 0.5$. The dimensionless parameters are $R_o = 1.0$, $M_a = 0.5$ and $R_s = 20$ and simulations are done on $10 < r < 30$, $0 < \phi < 2\pi$ with a resolution of 128×736. The hyperviscosity operator is Δ^3 and damps waves with a wavelength of the vortex diameter in 330 orbits around the compact object.

The interaction of a vortex with a bore is akin to the interaction of a vortex with a shock which received attention in the context of turbulent sound generation by rockets and airplanes. The following description was taken from Ellzey *et al*. (1995) and also applies to our calculation as Fig. 5.5 shows. A plain bore is distorted by a vortex and develops an S-shape: part of the bore is accelerated by the vortex while another part is retarded. Subsequently, a complex pattern of diffracted and reflected bores develops. Also a quadrupolar sound wave is generated. It combines with the reflected bore R2 to give an acoustic wave with a strong compression region attached to the most delayed part of the transmitted bore. This eventually restores the plain nature of the transmitted bore. While the shock and the acoustic wave have been studied in detail in the literature, the fate of the vortex has received little attention

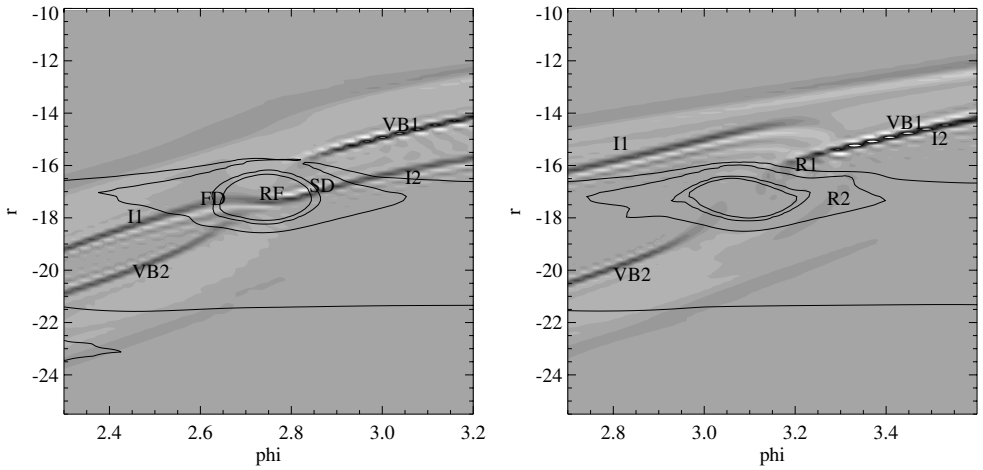

Figure 5.5: The divergence of the velocity shows the interaction of a bore with vortex 1 at $t = 9.84\ P_{orb}$ and $t = 9.94\ P_{orb}$. Vortex 1 moves to the right while the bore attached to vortex 2 moves to the left. The letters are the same as in Fig. 2 of Ellzey *et al*. (1995): I1 and I2 = incident bore, FD = fast diffracted bore, RF = diffracted bore, SD = slow diffracted bore, VB1 and VB2 = bores generated by vortex 1, R1 and R2 reflected bores. In the right picture I2 and VB1 coincide and R2 is very weak.

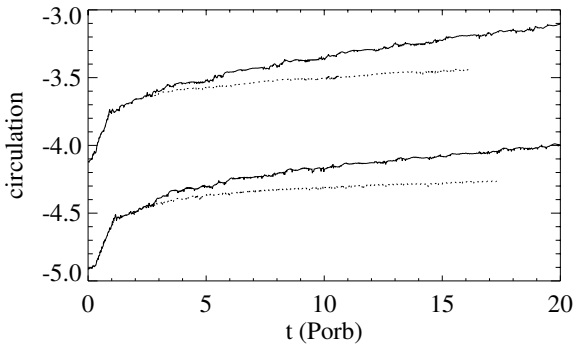

Figure 5.6: The circulation of the vortices as a function of time. Vortex 1 starts at a dimensionless circulation of -4.1 and vortex 2 at -4.9. The dotted lines are from two simulations with a single vortex starting from $r = 17.5$ and $r = 22.5$ respectively, and are given for comparison.

and deserves closer inspection.

In our application, the vortex is periodically shocked (bored) and emits sound waves. The situation is much more dynamic than for a single vortex in an accretion disk. Fig. 5.6 shows the circulation of the two vortices as a function of time. The initial difference in circulation of the vortices is an artifact of the measurement procedure and is due to the different Keplerian vorticity at their starting locations. The edge of the vortex is defined as a contour level of fixed absolute potential vorticity. If one of the vortices is at a smaller radius with a larger background potential vorticity, then a smaller fraction of the vortex lies below the edge level, giving a smaller circulation. Both vortices go through an adjustment phase in which circulation is lost after which a more stable evolution follows. However, in this second phase loss of circulation is still higher than for a single vortex in an accretion disk. Experiments show that this depends sensitively on the (hyper)viscosity and the resolution. The reason for the increased loss is the higher variability in shape (Fig. 5.7) that results in increased vorticity filament shedding and stronger viscous dissipation.

The area of the vortices (Fig. 5.7) is in magnitude similar to that of a single vortex, but it undergoes periodic bursts. The time interval between the bursts (2.3 $P_{\rm orb}$) is in agreement with that given by Keplerian advection: $\Delta t = 2\pi/\Delta\Omega_{\rm kep} = 2.26\ P_{\rm orb}$. The vortex shrinks as the bow wave of the other vortex passes. It expands strongly in the divergent region between bow wave and bore after which it is suddenly compressed by the bore. This, and the perturbations in elongation (Fig. 5.8) and orientation of the vortex, excite nutating motion notable as the small oscillations behind the strong collapse driven by the bore. Fig. 5.7 also shows that there is a small phase difference between both vortices of 8 percent of an orbital period.

Also in case of the elongation λ (Fig. 5.8), the variation is excited by the bore while the subsequent oscillations are from the nutation. As Fig. 5.5 shows, the long axis of the vortex is compressed when the bore passes and this decreases the elongation. The successive nutations decrease fast in amplitude. The difference between the

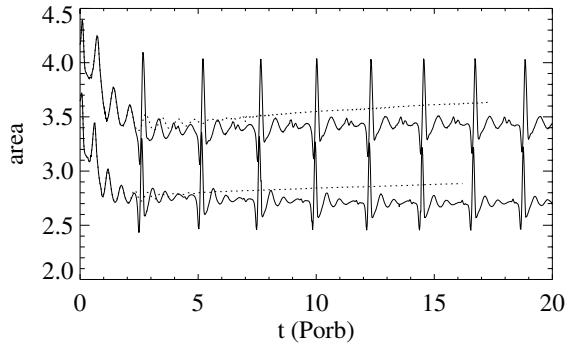

Figure 5.7: The area of each vortex as it interacts with the bore from the other vortex. Vortex 1 is indicated by the lower and vortex 2 by the upper solid line. The dotted lines are for simulations of single vortices as in Fig. 5.6.

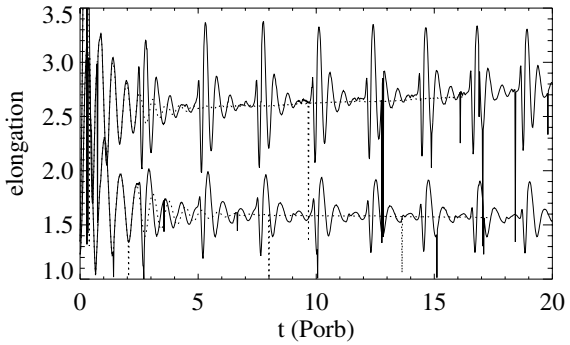

Figure 5.8: The elongation of two vortices that move through each other's bores as a function of time. For clarity, 0.3 is added to the elongation of vortex 1. Sometimes, the vortex recognition algorithm fails to attribute an elongation to a vortex and this gives rise to the spikes observed at, for example, $t = 12.8\ P_{\rm orb}$ for vortex 1.

elongation of both vortices is at least partly the result of the stronger shear in which vortex 1 (at smaller radius) is embedded compared with vortex 2.

The azimuthal drift of the vortices is compared with that of single vortices in Fig. 5.9. The azimuthal drift owing to β-gyres is proportional to $1/(\mathrm{M_a R_s})$ so that vortex 1 is expected to have a larger and vortex 2 a smaller drift because they are at different radii. Since the spread in observed drift velocities of single vortices in accretion disks (Fig. 16b of Nauta *et al*. (2000)) is large, the observed difference in drift speed is not inconsistent with an explanation based on β-gyres. The interaction with the bore is restricted to a short time interval and the net result is of minor importance compared to ordinary β-gyres drift. It seems that the interaction with the bore gradually increases the drift speed of vortex 1 and decreases that of vortex 2.

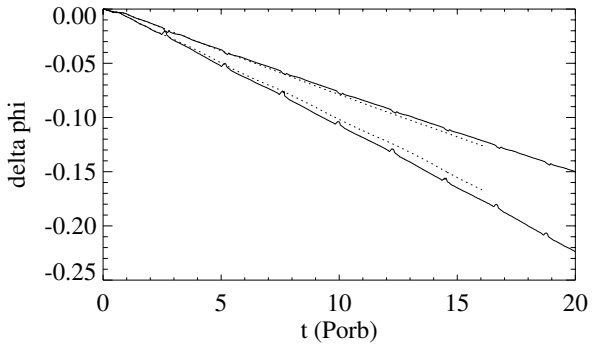

Figure 5.9: The azimuthal drift of the two vortices follows from the slope of the difference between observed ϕ-coordinate and the position determined by Keplerian advection: $v_1 = -0.016c_s, v_2 = -0.014c_s$.

The radial drift of the vortices does show a small net effect which is the direct consequence of the interaction with the bore (Fig. 5.10). Vortex 1 moves to smaller radius and vortex 2 to larger. The effect of the bow wave and bore is to push the vortices away from each other after which they bounce back and the drift continuous. However, close inspection shows that after each interaction vortex 1 is at a slightly smaller radius than the drift in between interactions can explain. This stepwise decrease in radial position accounts for approximately 8 percent of the observed drift rate of vortex 1. Perhaps, breaking of the bore deposits negative angular momentum in the vortex, or the acoustic wave generated by the interaction takes away some of the angular momentum, or alternatively vorticity filamentation is responsible for the loss.

Resonance

A special situation arises if the frequency with which the bore passes is a multiple of the nutation frequency of the vortex. This seems to happen when the same simulation as above is performed on a domain that is only 1.5 radians in azimuth. The

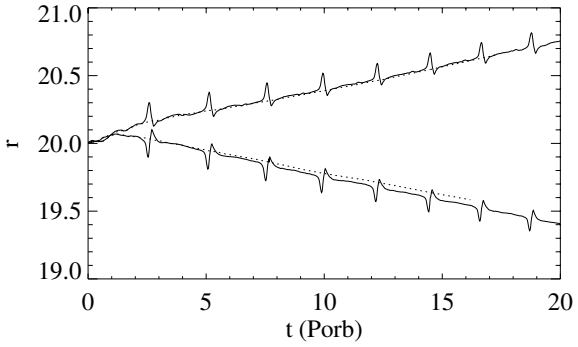

Figure 5.10: The radial position as a function of time. Vortex 1 moves inward and vortex 2 outward. For display reasons 2.5 was added to the position of vortex 1 and subtracted from vortex 2. The dotted lines are again from two simulations with a single vortex starting at $r = 17.5$ and $r = 22.5$ respectively. The stepwise decrease in radial position of vortex 1 is apparent.

smaller domain implies that interactions occur approximately four times as frequent as before and Figs. 5.7 and 5.8 show that in this case half a nutation is completed when the next bore interacts with the vortex.

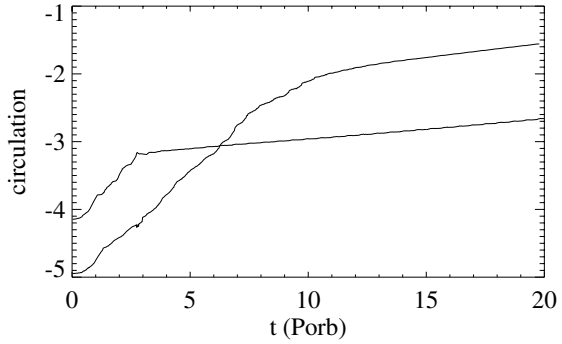

Figure 5.11: The circulation of the vortices on a domain that is only 1.5 radians in azimuth so that the frequency of the vortex-bore interaction is much larger.

Fig. 5.11 shows the circulation of the vortices as a function of time and is to be compared with Fig. 5.6. We see that vortex 1 has an extended adjustment phase but, more importantly, that vortex 2 loses most of its circulation. To verify this result, a simulation with a resolution twice as high and ten times lower hyperviscosity was done (the data shown is actually from this simulation). The elongation and orientation angle (not shown) indicate that vortex 2 is rotating and gets stretched strongly. The azimuthal and radial drifts are not significantly different from those discussed in Sect. 5.4.1.

5.4.2 Small impact parameter

As a typical example of vortices interacting with each other directly, a merger simulation is presented with vortex 1 at $r = 19.75, \phi = 1.0$ and vortex 2 at $r = 20, \phi = 0.5$. The other parameters have the same values as in the previous subsection. Fig. 5.12 shows the orbit of the two vortices. They rotate around each other during which epicyclic orbits are observed (as seen in a rotating coordinate frame initially co-rotating with vortex 2). Motion is slow during the epicycle loop, while it is fast in between.

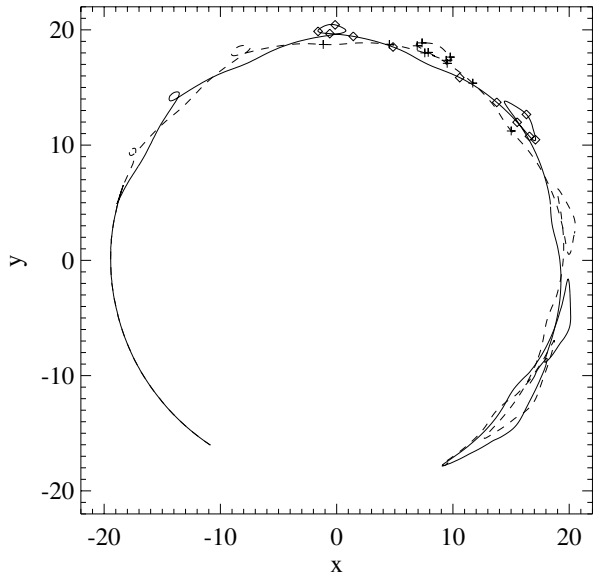

Figure 5.12: The orbit of the two vortices that merge in a coordinate frame rotating at the Keplerian speed at the initial position of vortex 2. Vortex 1 is indicated with the solid line and vortex 2 with the dashed line. They start in the lower right corner and move anti-clockwise. The position of the vortices is indicated at equidistant times from $t = 23.75\ P_{\rm orb}$ to $t = 29.58\ P_{\rm orb}$ by squares and pluses to get a sense of velocity.

Merger might be thought of as a process that creates large scale structures. However, Fig. 5.13 shows the circulation of the vortices as a function of time: when the vortices interact with each other they lose a substantial part of their circulation. The product of the merger is a vortex that is much weaker then the two original vortices. Another notable feature is the long time it takes before merger is accomplished. Previous simulations were only run for 10 or 20 orbital periods. The area of the vortices shows a similar trend in time as the circulation (not shown): between the oscillations due to nutation which is excited with each passage, a stepwise decrease in area can be found. Right before merger, each vortex occupies about 0.7 times the area of the original vortices and when merger is complete the expanse is some 1.2 times the

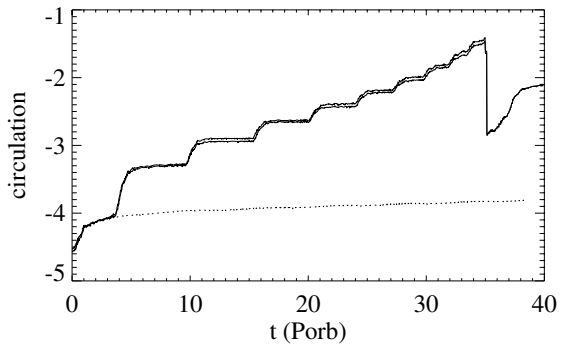

Figure 5.13: The circulation of two merging vortices as a function of time. The dotted line is from a single vortex (at $r = 20$) and is meant for comparison.

size of an initial vortex. This is lower than the rule of thumb determined for incompressible vortex merger without background shear flow (Carnevale *et al.*, 1991) of 1.4 times the original vortex area.

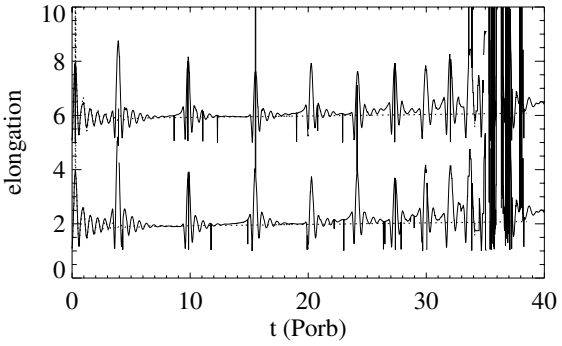

Figure 5.14: The elongation of two merging vortices as a function of time. For clarity the data of vortex 1 was shifted by 4. The spikes are non-physical, see the caption of Fig. 5.2 or 5.8.

Fig. 5.14 shows the elongation as a function of time. Large fluctuations are seen during the interaction which are followed by oscillations due to nutation. Fig. 5.15 shows two snapshots of the interaction at $t = 10\ P_{\rm orb}$. At closest approach the vortices are almost circular but afterwards they get strongly elongated and spiral arms develop in potential vorticity. In this way vorticity is shed and (hyper)viscosity gets an opportunity to dissipate some of the circulation. During the last phase of merging, the vortex recognition algorithm is not able to attribute a reliable elongation to the vortices but, with the merger complete, the vortex is seen to be more elongated because it is weaker than the original vortices. A notable feature is also that the elongation of the vortex at the smallest radius increases slightly before the interaction

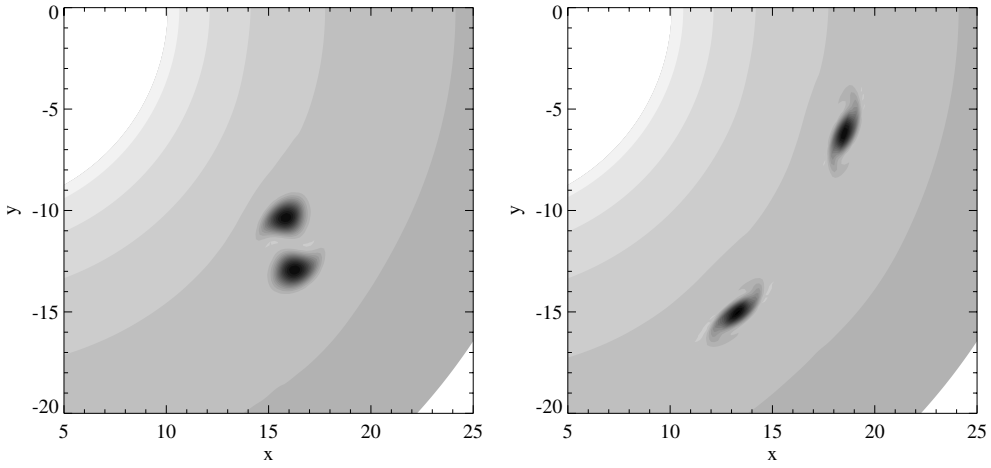

Figure 5.15: Potential vorticity distribution at $t = 9.55\ P_{\rm orb}$ and $t = 10.51\ P_{\rm orb}$ of two vortices that will eventually merge.

while the vortex at the largest radius retains its shape (see Fig. 5.17 for the radial position of the vortices).

These results are rather different from what is known from the literature. Marcus (1990) notes that merger goes fast and is conservative with only minor losses in circulation and area. He claims for example that the loss in area is only 3 percent. However, his results are for 2D-incompressible flow. Our simulations at a lower Mach number (or increased Rossby deformation radius $L_{\rm D} = c_{\rm s}/\Omega$) then before do indeed show that merger goes faster because it takes fewer revolutions of shorter duration and that the loss of circulation per revolution is lower. However, we always observe a substantial decline in circulation instead of a loss of a few percent. Contour dynamics calculations of symmetric vortex merger without background flow but with finite Rossby deformation radius (Waugh, 1992) showed that merger produces less filaments and is more conservative at smaller deformation radius. This need not mean that if both shear and a finite Rossby radius of deformation are present, as in our simulations, losses could not be higher then in both cases separately. Essential in this is also the role of dissipation because thin structures develop that are sensitive to the (hyper)viscosity. To quantify the losses during merger at really high Reynolds number contour dynamics simulations would have to be performed. With the hyperviscosity as we use it, which also gives high Reynolds numbers, we find that merging has a rather "destructive" effect.

The azimuthal drift in Fig. 5.16 mainly consists of a uniform drift not greatly different from that of a single vortex. During the interaction which lasts short (approximately 1 $P_{\rm orb}$), the vortices move around each other after which the drift is steady again. Comparison with a graph of the distance between the vortices (not shown) demonstrates that the typical distance over which the vortices "feel" each other is 6

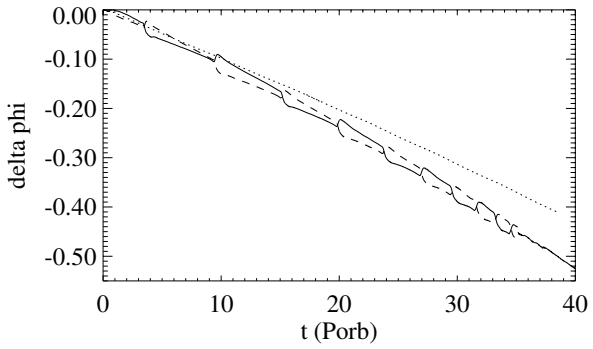

Figure 5.16: The azimuthal drift of two merging vortices as a function of time. The solid line signifies vortex 1, the dashed line vortex 2 and the dotted line the single reference vortex at $r = 20$.

to 8 in dimensionless units. The steady drift in between interactions is different for the two vortices. The vortex with the largest ϕ-coordinate has a drift additional to the usual β-gyres drift. So it helps the differential Keplerian advection in bringing the vortices close to each other for their next interaction. Modification of the β-gyres can't explain this additional drift because measurements at ten different times all show that the vortex with the smallest drift has the strongest β-gyres. Also advection by the velocity field of the other vortex is not a valid explanation because then the additional drift should be a function of the distance between vortices while it is seen to be constant in between interactions. During the simulation the drift speed of both vortices increases and the merged vortex has a larger drift speed than the single vortices. Close inspection of the vorticity shows that the initial vortices are partly shielded (the vortex core is surrounded by opposite sign vorticity) while the merged vortex is not. This changes the circulation that is induced outside of the vortex and thus the β-gyres (see also Fig. 5.20).

The radial position of the vortices is dominated by the rotation around each other (see Fig. 5.17). The radial velocity field responsible for the motion is in geostrophic balance at large distances from the vortices so that angular momentum can be exchanged between the vortices by the pressure field. Superimposed on this rotation is a decrease in radial distance of both vortices which is not much different from that of a single vortex. The average radial position shows that during the interaction the small radial drift is suppressed so that the inward motion of both vortices is slowed down slightly.

5.5 Three vortices

The presence of a third vortex allows even richer behavior than that of only two. The new interaction that is possible is a third vortex that runs off with part of the angular momentum while the other two vortices are interacting. This can accelerate

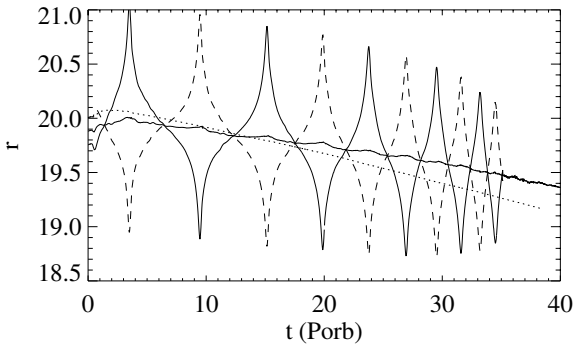

Figure 5.17: The radial position of two merging vortices as a function of time. The solid line indicates vortex 1, the dashed line vortex 2 and the dotted line a single reference vortex at $r = 20$. The middle solid line is the average position of both vortices.

the merging process and perhaps contribute to transport.

Initially, the three vortices are located at the same r-coordinate, $r = 20$, and at $\phi = 0.5, \phi = 1.0$ and $\phi = 1.5$ respectively. All other parameters are as before. The subsequent radial position of the vortices is shown in Fig. 5.18. Vortex 1 and 2 merge with each other at $t \approx 7\ P_{\rm orb}$ while vortex 3 moves to larger radius and keeps hovering around for the rest of the simulation. The increase in radius and thus angular momentum of vortex 3 is accompanied by a loss of angular momentum of vortex 2. As a result it is pushed in the direction of vortex 1 which was already advected to smaller radius and this speeds up the merging process. Within two revolutions the outer parts of the vortices have merged. There are still two vorticity cores present and that is why the vortex tracking algorithm has some trouble with the identification. So at $t = 7.6\ P_{\rm orb}$ it "thinks" there are two vortices but these are just the vorticity

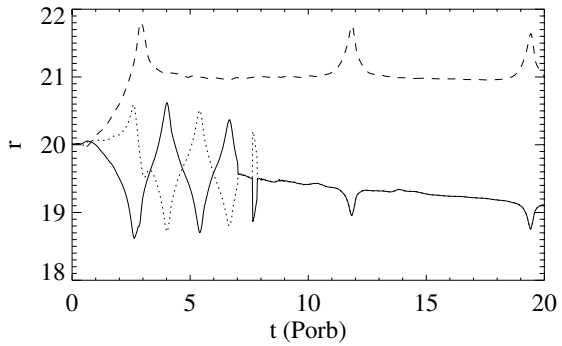

Figure 5.18: The radial position of three interacting vortices as a function of time. Vortex 1 is indicate with the solid, vortex 2 with the dotted and vortex 3 with the dashed line.

cores in the process of merging. Once the merger is complete, there follows an interaction with vortex 3 that has performed a complete revolution around the compact object in the mean time. Because the vortices are separated by a radial distance that is larger than the size of the vortices, the interaction does not lead to a new merger but advection just moves them past each other.

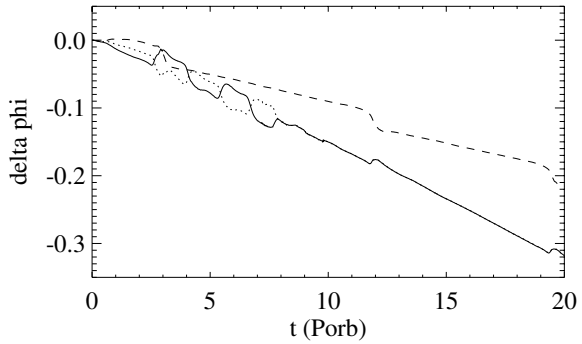

Figure 5.19: The azimuthal drift of three interacting vortices as a function of time. See Fig. 5.18 for the meaning of the different lines.

The interaction of the vortices is also visible in the azimuthal drift as perturbations in the track of vortex 2 and 3 in Fig. 5.19. After this interruption, the subsequent evolution of the azimuthal drift of vortex 1 and 2 is not any different from that of the usual merger. The subsequent interaction of the merged vortex with vortex 3 just shows the mutual advection which is not followed by a merger. The difference between the azimuthal drift of the merged vortex and vortex 3 is considerable. During merging the average azimuthal drift is seen to increase (just as in Fig. 5.16). The physical explanation is clear from Fig. 5.20 which shows the relative vorticity at $t = 19.1\ P_{\rm orb}$ as a grayscale with superimposed a potential vorticity contour. Vortex 3 consists of a negative vorticity core that is surrounded by small-amplitude positive relative vorticity. Such a partly shielded vortex is always the outcome of the initial condition. The positive vorticity is background vorticity that is entrained by the vortex. The merged vortex has a negative vorticity core that is similar to that of vortex 3 (see also Fig. 5.21) but it is surrounded by small-amplitude negative relative vorticity. During the merging process, the surrounding positive vorticity of each vortex is expelled and replaced by negative vorticity. As a result the circulation induced by the vortex in its neighborhood increases so that the β-gyres get larger and intensify which in its turn increases the azimuthal drift speed of the vortex. The sensitivity on the small amplitude vorticity hull seems also an attractive explanation for the scatter in the observed azimuthal drift speeds (Fig. 16 of Nauta *et al*. (2000)). Measurements of the vortices are always done on the vorticity core and not on the low lying vorticity environment. Another phenomenon explained by this observation is that the excursions in radius (Fig. 5.18) and azimuth (Fig. 5.19) of vortex 3 during the interaction are larger than those of the merged vortex. This is also a direct consequence

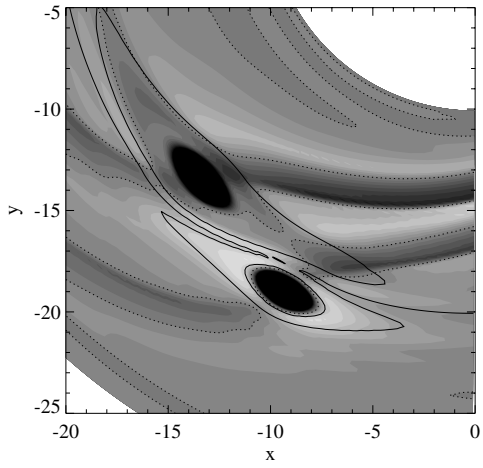

Figure 5.20: The relative vorticity as a grayscale (range: -0.3 to 0.3) of an ordinary and a merged vortex (upper one) at $t = 19.1\ P_{\rm orb}$. The solid contour is a potential vorticity contour and indicates the boundaries of the two vortices. The dotted contour is the zero contour of relative vorticity and the vortex cores are overexposed.

of the shielding.

Since the merger takes less time than when only two vortices are present, it is expected that the merging is less "destructive". Fig. 5.21 shows the circulation as a function of time. Comparison with Fig. 5.13 shows that there is indeed a smaller loss of circulation. The merged vortex has a comparable circulation as the initial vortices after their adjustment phase.

Merging occurs for small enough impact parameter which may very well depend on the Rossby deformation radius. Incompressible simulations in the literature suggest that merging only occurs for impact parameters that are of the size of the vortices (Marcus, 1990), which is in this case of order unity. The simulations we have done do not contradict this.

5.6 Multiple vortices

Finally, a simulation with 10 vortices is presented. We expect to see most of the above mentioned processes. The radial positions of all vortices is shown in Fig. 5.22. This graph also shows the numbering of the vortices. Vortex 0 was placed at $r = 20, \phi = 0.5$ while the other 9 vortices were placed at random positions in r and ϕ within the range $15 < r < 25$. The other parameters of the simulation are as usual except for the hyperviscosity coefficient that was slightly increased (1.4 times larger). To determine if vortices are close together we also need the azimuthal position which is a rather crowded plot (Fig. 5.23). Here the same line styles are used as in Fig. 5.22 and with the numbers it should be easy to determine which vortex is which. What might

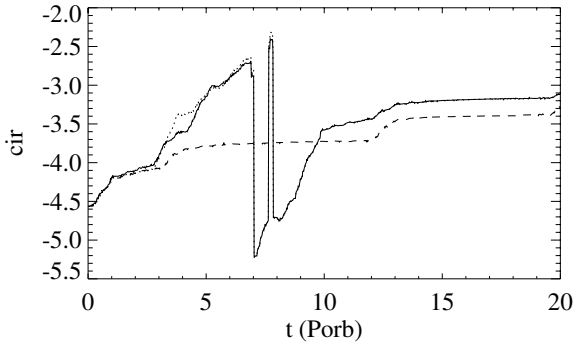

Figure 5.21: The circulation of three interacting vortices as a function of time. See Fig. 5.18 for the meaning of the different lines.

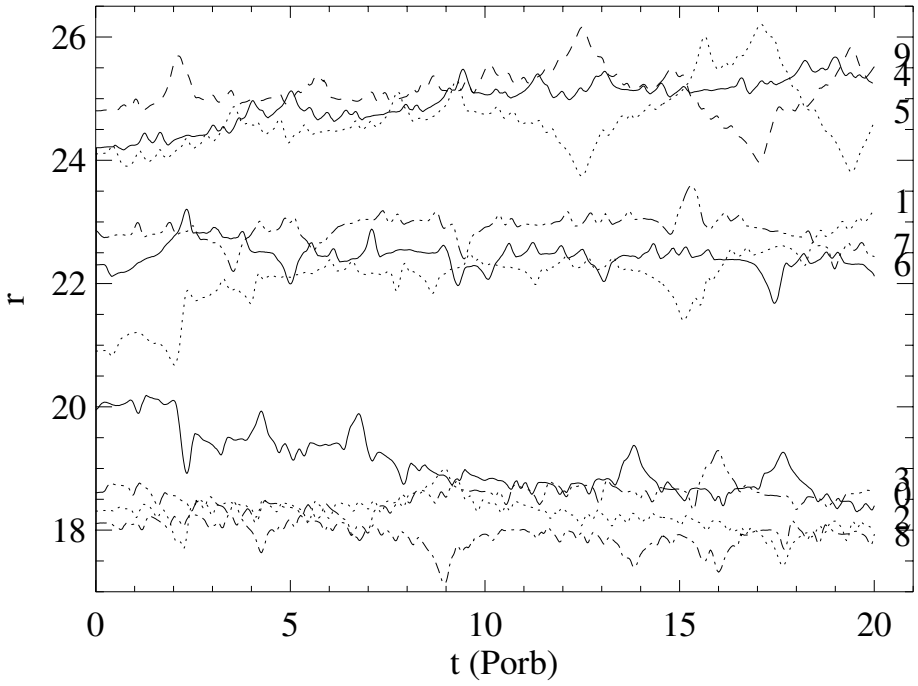

Figure 5.22: The radial position of ten vortices as a function of time.

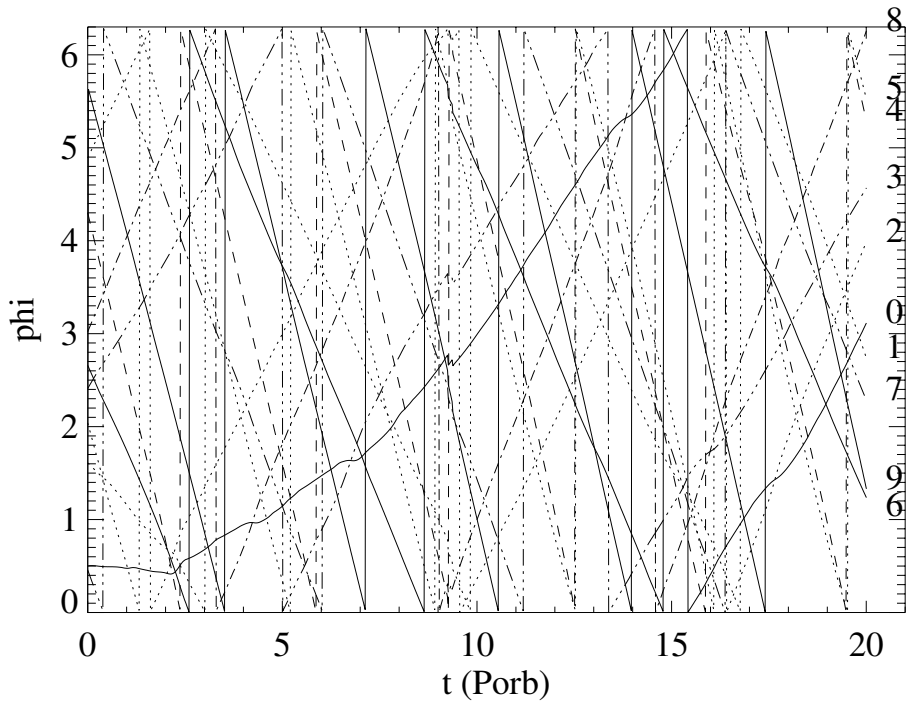

Figure 5.23: The azimuthal position of ten vortices as a function of time. There was a problem with the tracking algorithm at $t \approx 9.3\ P_{\rm orb}$ due to interacting vortices on the periodic boundary.

help is the realization that the slopes are mainly determined by Keplerian advection so they are a measure of the radial position. Fig. 5.24 shows the circulation of all vortices.

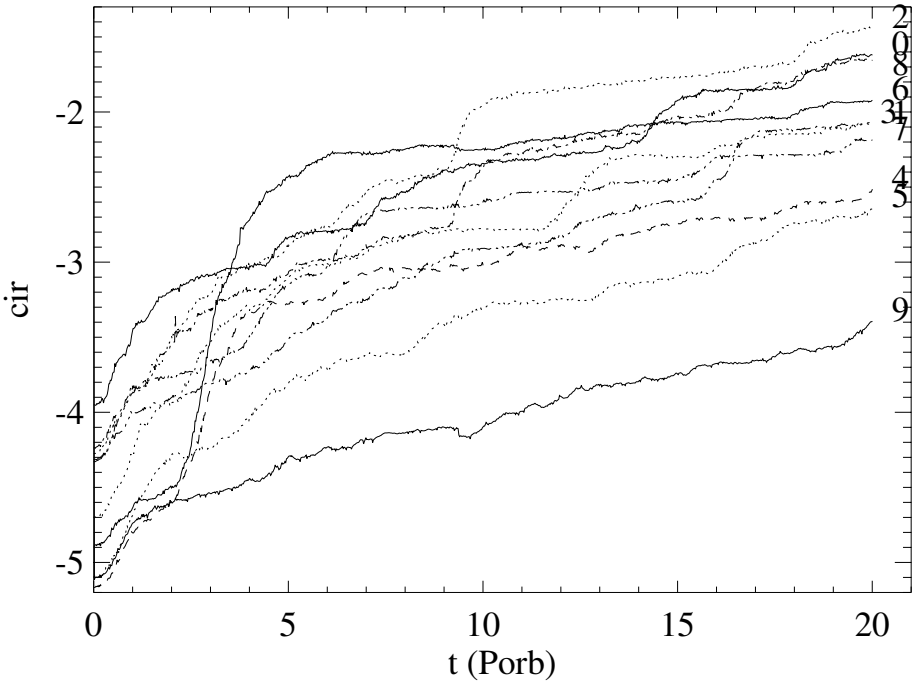

Figure 5.24: The circulation of all ten vortices as a function of time.

Right at the beginning there is already an interesting interaction. At $t \approx 2\ P_{\rm orb}$ we see several vortices that change their radial position: 2, 0, 1, 6 and 4 in order of increasing radius. Their azimuthal position indicates that they are all close together around $\phi = 0.6$. Vortex 0 and 1 are seen to exchange angular momentum (Fig. 5.22) so that vortex 0 losses it and 1 gains it. They move apart so far that they will never meet again. Vortex 6 is in between vortex 1 and 4 and the circulation shows that this is a dangerous position; it loses approximately half of its circulation. Vortex 4 pays also a price in the form of high circulation losses.

Numerous other interactions can be recognized in the data. Large variations in radial position are typical for vortex-vortex interactions (for example vortex 0 and 8 at $t \approx 4.2\ P_{\rm orb}$), while small modulations are typical for vortex-bore interactions (for example vortex 9 and 3 at $t \approx 1.7\ P_{\rm orb}$). A triple vortex interaction occurs at for example $t \approx 7\ P_{\rm orb}$ between vortices 3, 0 and 6. Noteworthy is also the locking of vortex 4 and 5 in a couple that will merge (at $t \approx 29$, not shown). The simulation was continued up to $t = 33\ P_{\rm orb}$ and by that time quite a number of vortices are circulating around each other which is the prologue to merger: 0+3, 1+6 and maybe 2+8.

There are also events missing. The resonance that pealed off one of the vortices in Sect. 5.4.1 does not seem to occur. There are probably too many perturbations at hand.

It is also useful to look at the overall behavior. The circulation, Fig. 5.24, shows for example that the vortices decay relatively fast. On a time scale of hundreds of orbits each vortex would erode away. This is in agreement with the study of individual interactions in the previous sections. As was mentioned this will be sensitive to the effective viscosity that is used.

Radial drift is the most interesting from the point of view of transport. Fig. 5.25 shows the average radius of all ten vortices. Initially it increases, especially during the adjustment phase which is a trend that is also known from single vortex simulations. But after 10 orbits there is a decrease in average radius. This is roughly of the same order of magnitude as the radial drift of single vortices. This indicates that mass transport is proportional to the number of vortices; there is no enhanced transport due to interactions of vortices.

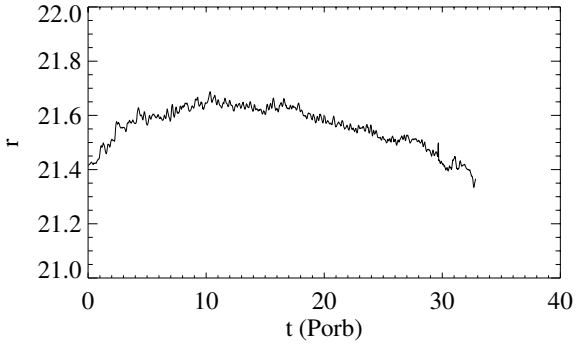

Figure 5.25: The average radius of all ten vortices.

5.7 Conclusion

Previously, a single vortex in an accretion disk was studied (Nauta *et al.*, 2000). Here, this study is extended in several ways. First a single vortex was studied now including the energy equation for an ideal gas instead of using a polytropic relation. The only significant difference found is that bores in polytropic disks do not lead to heating of the disk while shocks with the energy equation do.

Next multiple vortices were studied in polytropic disks. If two vortices are separated in radius by a distance larger than the thickness of the disk, then they interact with the bore excited by the other vortex. If the radial separation is smaller then the vortices interact directly with each other's vorticity distribution. If they are close enough (radial separation smaller than the size of the vortices) then they can merge.

At the small hyperviscosity that we use, vortex-bore interaction leads to some loss of circulation and thus vortex strength. Vortex-vortex interaction leads to a much larger loss of circulation under the same dissipation because strong spiral arms develop in potential vorticity that give filamentation and dissipation a chance to degrade the vortex. So even in the case of fusion, the merged vortex can be weaker than each one of the original vortices. It was found that a third vortex can take away some of the angular momentum of two merging vortices which speeds up the merging process so that losses of circulation are smaller.

The azimuthal drift of the vortices is found not to depend directly on the transient vortex-bore or vortex-vortex interactions. Their influence is more subtle. The negative vortices that come out of the adjustment phase have all entrained fluid with positive background vorticity so they are partly shielded. The interactions can affect the shielding and in that way the circulation that the vortex excites in its neighborhood. This changes the β-gyres and thus the azimuthal drift.

The radial drift is directly influenced by vortex-bore interactions but the result is small. Vortex-vortex interactions seem to slow down the radial drift, but again the result is small.

When ten vortices are released in the disk all of the processes occur at the same time. The result is a fairly rapid loss of circulation. The average radial drift of the vortices stays of the same order of magnitude as that of a single vortex. So the alpha value that can be achieved with 2D-vortices in accretion disks does not grow stronger than linear in the number of vortices (cf. Nauta *et al.*, 2000).

Hoofdstuk 6

Nederlandse Samenvatting

Naast bolvormige kennen we ook schijfvormige structuren in de sterrenkunde. Het bekendste voorbeeld hiervan is waarschijnlijk het ringensysteem om Saturnus. Ook de banen van de planeten aan de hemel, die maar door 13 sterrenbeelden voeren, duiden er op dat de planeten uit een schijf gevormd zijn. Directe waarnemingen van gasschijven zijn van recenter datum. De ruimtevaart stelt ons in staat om hoogenergetische straling waar te nemen die door de aardse atmosfeer wordt tegengehouden. Deze waarnemingen tonen dat er een aantal zeer heldere bronnen van röntgenstraling bestaan die niet in overeenstemming zijn met een stellaire oorsprong. Nadere bestudering toont dat de bronnen gasschijven zijn rondom compacte sterren (dit zijn sterren met een massa die vergelijkbaar is met die van onze zon maar een straal die veel kleiner is dan een zonsstraal zoals een witte dwerg, een neutronenster of een zwart gat). Een schematisch plaatje van zo'n gasschijf is weergegeven in Fig. 1.1. Het systeem bestaat uit twee sterren die om elkaar draaien waarbij de ene ster materie verliest aan de andere. Vanwege de draaiing van het systeem valt materie niet direct op het compact object. Hierbij is het misschien nuttig om aan een klassieke zweefmolen op een kermis te denken. Als hij draait dan staan alle kabels waaraan de stoeltjes hangen onder een hoek met de verticaal. Slechts als de draaiing van de molen afneemt, keren de touwen terug in hun verticale positie en bewegen de stoeltjes naar een kleinere straal. Zo is het ook bij sterren die materie overdragen. Vanwege de draaiing (het impulsmoment) vormt de overstromende materie een ring rondom het compacte object. Slechts als er draaiing weggenomen wordt kan materie naar kleinere straal bewegen. Wrijving is een proces dat hiervoor kan zorgen. Hierdoor verliest een deel van de materie z'n impulsmoment en valt naar kleinere straal, terwijl een ander deel juist impulsmoment wint (want het totale impulsmoment is behouden) en naar grotere straal beweegt en er zo dus een schijf gevormd wordt. De snelheid in de schijf is afhankelijk van de straal en is ongeveer Keplers $v_{\rm kep} \propto 1/\sqrt{r}$, wat betekent dat de aantrekkingskracht van het compacte object gebalanceerd wordt door de middelpuntvliedende kracht. De schijf wordt aan de buitenkant gevoed door gas dat van de begeleidende ster afkomstig is. Dit spiraliseert naar binnen en wordt gedeponeerd op het oppervlak van de compacte ster. Daarom heet zo'n schijf ook wel groeischijf of accretieschijf.

Tijdens het accretieproces beweegt de materie van de buitenrand van de schijf naar de binnenrand. Hierbij komt zwaartekrachtsenergie vrij. Dit wordt gedeeltelijk omgezet in bewegingsenergie (vergelijkbaar met Newtons appel die van de boom valt) maar ook gedeeltelijk uitgezonden als de straling die we waarnemen. Uit bijvoorbeeld de waargenomen hoeveelheid licht maar ook uit veel andere metingen is berekend dat de hoeveelheid materie die invalt groot is vergeleken met wat verwacht mag worden op grond van standaard wrijvingsprocessen in een gas. Dit betekent dat er een mechanisme moet zijn dat een effectief grotere wrijving geeft dan moleculaire beweging van de gasdeeltjes.

Op zich is een dergelijk fenomeen ook wel bekend van vloeistoffen in de natuur of in laboratoria en wordt het veroorzaakt door turbulentie. Dit is het verschijnsel dat stroming vaak opbreekt in wervels die dan weer opbreken in steeds kleinere werveltjes, zie bijvoorbeeld de rook die uit een schoorsteen komt. Deze werveltjes mengen de vloeistof veel effectiever dan moleculaire bewegingen en geven daarom aanleiding tot groter transport. Voor het opbreken van de stroming in een verzameling werveltjes is meestal een aanwijsbare reden: de stroming wordt instabiel. In het geval van een accretieschijf is alleen een instabiliteit gevonden als er magneetveld aanwezig is; zonder dat lijkt het dat stroming glad zou moeten zijn. Aangezien magneetveld overal voorkomt in de ruimte, is de algemene opvatting dat hiermee de verklaring voor de efficiënte accretie wel gevonden is. Toch blijft het idee van een accretieschijf zonder magneetveld aantrekkelijk. Enerzijds omdat het moeilijk is om te bewijzen dat een schijf zonder magneetveld geen accretie vertoont (turbulentie is een proces dat nog altijd slecht begrepen wordt) anderzijds omdat er situaties voor te stellen zijn waarbij het magneetveld zwak gekoppeld is aan het gas. Dit komt bijvoorbeeld voor in protoplanetaire schijven die zo koud zijn dat maar een kleine fractie van de materie geioniseerd is.

Tot nog toe is de meeste aandacht uitgegaan naar turbulentie waarbij de energie aan steeds kleinere structuren wordt overgedragen. De reden hiervoor is een proces dat strekking van wervelbuizen heet. Turbulentie bestaat uit wervelingen waarbij men kan denken aan vloeistof die ronddraait in buisjes die kriskras door elkaar liggen, ongeveer zoals een bord spaghetti. Het ene wervelbuisje induceert een snelheidsveld in het andere wat leidt tot vervorming. Over het algemeen zal dit leiden tot uitrekking van die wervelbuis. Als de wervelbuis langer wordt zal die ook dunner worden, en als die dunner wordt gaat hij sneller draaien (zie bijvoorbeeld een pirouette van een ballerina die haar armen intrekt). De kleinere doorsnede en het sneller draaien betekenen dat er energie aan kleinere structuren wordt overgedragen en dit heet de gewone energiecascade. Dit proces treedt niet op als de wervelbuizen zo geordend zijn dat ze allemaal evenwijdig aan elkaar lopen want dan rekken ze elkaar niet uit. De dynamica speelt zich nu af in een twee-dimensionaal (2D) vlak en deze vorm van turbulentie heet wel 2D-turbulentie en is bekend van het weer. De laag van de atmosfeer waarin het weer zich afspeelt is ongeveer 15 kilometer dik terwijl typische hoge- en lagedruk gebieden (wervels) honderden kilometers groot zijn. Dit betekent dat de vloeistofbeweging zich bij benadering in een horizontaal vlak afspeelt. Dit wordt nog versterkt doordat de aarde ronddraait om haar as (het belang hiervan wordt aangegeven met het Rossbygetal van de stroming, hoe kleiner

hoe meer invloed rotatie heeft) en doordat de atmosfeer gelaagd is in de verticale richting en de "zwaarste" laag meestal het dichtst bij het oppervlak is. Vanwege het ontbreken van wervelbuisstrekking wordt energie nu niet aan kleinschalige structuren overgedragen maar het blijkt dat juist uit kleinschalige structuren grootschalige gevormd worden: de inverse energiecascade. Met dit proces wordt het begrijpelijk waarom wervels in de aardse atmosfeer, maar ook bijvoorbeeld op Jupiter, zo lang kunnen bestaan en niet makkelijk opbreken in kleinere eenheden. Het is deze vorm van turbulentie die ik heb bestudeerd in een accretieschijf.

Een eerste benodigde om wervels en 2D-turbulentie in een accretieschijf te bestuderen is een goed numeriek programma dat in staat is om de 2D-vloeistofvergelijkingen op te lossen. Deze bestaan uit de continuiteïtsvergelijking die beschrijft hoe de dichtheid van een vloeistofpakketje verandert gegeven een dichtheids- en snelheidsveld, en uit de impulsvergelijking die beschrijft hoe het snelheidsveld van dat pakketje verandert onder invloed van de krachten die er op werken. Eventueel kunnen deze vergelijkingen aangevuld worden met een energievergelijking die beschrijft hoe de energie van dat pakketje verandert, maar ik heb in de meeste berekeningen een aanname gebruikt die druk en dichtheid aan elkaar relateert (polytrooprelatie). Het resultaat is een set vergelijkingen die erg veel lijkt op de ondiep-water vergelijkingen die gebruikt worden om de dynamica van dunne vloeistoflagen te beschrijven (deze laatste vormen bijvoorbeeld de kern van de numerieke weervoorspelling). Het verschil zit in de samendrukbaarheid van het gas. Gedurende de laatste 30 jaar is er een zeer uitgebreid scala aan numerieke technieken ontwikkeld om dit soort vergelijkingen op te lossen. Wat opviel bij de bestudering van de relevante astro- en geofysische literatuur was dat in de astrofysica de meeste aandacht uitgaat naar het goed representeren van discontinuïteiten (schokken) in de stroming, terwijl in de geofysica technieken ontwikkeld zijn om enstrofie te behouden. Enstrofie is een maat voor de rotatie van de vloeistof en is behouden als er geen dissipatie is. Het speelt een belangrijke rol bij de verklaring voor de inverse energiecascade. Het algoritme dat gebaseerd is op dit principe wordt onder andere gebruikt in klimaatstudies en om de stroming op Jupiter te simuleren. Ik heb de keuze gemaakt om ditzelfde algoritme te gebruiken voor mijn onderzoek en het is beschreven in Hoofdstuk 2. Hierin beschrijf ik ook de kleine aanpassing die nodig is voor accretieschijven en vergelijk ik het met een code (VAC) die wel goed overweg kan met discontinuïteiten. Het enstrofiebehoudende algoritme geeft extra oscillaties bij discontinuïteiten maar het berekent de dynamica van wervels nauwkeuriger en sneller dan VAC bij dezelfde resolutie.

In Hoofdstuk 3 wordt de numerieke code toegepast om 2D-turbulentie te onderzoeken. Traditioneel wordt 2D-turbulentie bestudeerd met behulp van incompressibele berekeningen zonder achtergrondstroming. Dit wijkt sterk af van de condities die gelden in een accretieschijf. Bij benadering draait een dunne schijf Keplers rond, dus dit is de achtergrondstroming waarop eventuele turbulentie gesuperponeerd is. Daar komt nog bij dat de afschuiving van deze scheringsstroming sterk supersoon is. De consequentie is dat compressibele effecten belangrijk zullen zijn als de wervels groter worden dan de dikte van de schijf. Eerst wordt het effect van samendrukbaarheid en rotatie onderzocht. Dit introduceert een intrinsieke lengteschaal in het

probleem, de Rossbydeformatiestraal, die van dezelfde orde van grootte is als de dikte van de schijf. Dit roept de vraag op of wervels kunnen uitgroeien boven deze lengteschaal. In mijn simulaties lijkt dit inderdaad het geval te zijn alhoewel zulke grote wervels minder snel samensmelten en er minder robuust uit zien. Vervolgens is 2D-turbulentie bestudeerd in de aanwezigheid van een uniform scherende achtergrondstroming. Het opvallenste effect hiervan is dat wervels die tegen de schering in draaien alleen kunnen bestaan als ze veel sterker zijn dan de schering. Is dit niet het geval dan worden ze uiteengetrokken. Wervels die meedraaien met de schering zijn beter in staat om uitrekking tegen te gaan. Is zo'n wervel echter zwak vergeleken met de schering dan wordt de uitrekking zo sterk dat hij niet meer herkenbaar is als wervel. Een ander effect van de schering is dat enige afschuiving fusie van wervels bespoedigt omdat het wervels in elkaars buurt brengt. Bij grotere schering echter wordt het samensmelten afgeremd omdat excursies van wervels loodrecht op de scheringsstroming kleiner worden waardoor er minder ontmoetingen zijn. Tenslotte introduceert ook schering (samen met compressibiliteit) een intrinsieke lengteschaal in het probleem en ook deze is vergelijkbaar met de dikte van de schijf. Het bleek niet mogelijk om wervels groter te maken dan deze intrinsieke lengteschaal. De consequenties voor een accretieschijf zijn dat alleen wervels die sterk genoeg zijn (met een Rossbygetal van de orde 1 of groter) en die kleiner zijn dan de dikte van de schijf verwacht mogen worden. Vergelijken we dit met de voorwaarden waaronder een twee-dimensionale beschrijving gerechtvaardigd is, dan vinden we een ongerijmdheid. Het is dan ook maar de vraag of ideeën over twee-dimensionale turbulentie wel van toepassing zijn op een accretieschijf.

Wervels die sterk genoeg zijn en die kleiner zijn dan de dikte van de accretieschijf zouden in staat moeten zijn om lange tijd in een accretieschijf te blijven bestaan. Het gedrag van één zo'n wervel is bestudeerd in Hoofdstuk 4. Een cirkelvormige verstoring in het snelheidsveld is gesuperponeerd op een segment van een Keplers roterende schijf en ontwikkelt zich na een aanpassingsfase tot een wervel die maar langzaam verandert in de tijd. De krachtenbalans van deze wervel is opgesteld en we vinden dat middelpuntvliedende en Corioliskrachten elkaar grotendeels compenseren. De drukkracht completeert de balans en speelt in de verschillende richtingen een andere rol. In de radiële richting is de wervel een hoge- en in de azimuthale richting een lagedrukgebied. Dit betekent dat het drukprofiel zadelvormig is voor een wervel met een Rossbygetal van de orde één. De vorm van de wervel is elliptisch en wordt goed benaderd door een geïdealiseerd analytisch model: de Kidawervel. Als de dissipatie klein is dan vertoont de ellips schommelingen. Ook die worden redelijk beschreven door het Kidamodel. Deze schommelingen leiden tot chaotische advectie (dit is het verschijnsel dat een gelokaliseerde wolk van deeltjes die passief meebewegen met de stroming over een groot oppervlak verspreid worden) in de buurt van de buitenrand van de wervel. De wervel wekt geluidsgolven op en die organiseren zich buiten de wervel als een soort boeggolf en een soort schok. De wervel drijft ook langzaam in de azimutale en radiële richtingen. De azimutale drift is een orde van grootte sneller dan de radiële drift en wordt veroorzaakt door secundaire wervels (β-gyres) die het gevolg zijn van de stroming om de wervel heen. Soortgelijke verschijnselen spelen een rol bij de beweging van wervels op aarde zoals

bijvoorbeeld orkanen. De verklaring voor de kleine radiële drift is niet zo duidelijk. Het is mogelijk dat de geluidsgolven die opgewekt worden impulsmoment meenemen en dat als gevolg daarvan de wervel z'n radiële positie aanpast. Vaak beweegt de wervel naar de centrale ster en draagt zo bij aan accretie. De hoeveelheid materie die op deze manier getransporteerd kan worden is echter maar klein.

In hoofdstuk 5 worden de voorgaande berekeningen uitgebreid. Eerst wordt een enkele wervel bestudeerd, nu met gebruikmaking van de energievergelijking. Dit levert eigenlijk geen nieuwe inzichten op. Vervolgens worden wervelinteracties onderzocht waarbij de polytrooprelatie gebruikt wordt. Als de radiële afstand tussen de wervels groot is, dan is de interactie beperkt tot schok-wervel interactie en dit herhaalt zich bij elke omloop om het compacte object. Het schokfront wordt vervormd door de wervel en een geluidsgolf wordt opgewekt. Na de interactie herstelt het schokfront zich weer. Ook de veranderingen in de wervel zijn maar beperkt. Tijdens elke interactie wordt de wervel vervormd, maar dit herstelt zich telkens weer. Hiermee gepaard gaat een klein verlies in sterkte van de wervel. De azimutale drift wordt niet direct beinvloed door de schok-wervel interactie. De radiële drift wel maar het effect is kleiner dan de gewone drift van een enkele wervel. Als de wervels dicht bij elkaar komen dan kunnen ze samensmelten. Voordat dit gebeurt draaien ze eerst een aantal malen om elkaar heen gedurende welke de wervels sterk vervormd worden. Hiermee gepaard gaat een aanzienlijk verlies in sterkte van de wervels. Het is zelfs mogelijk dat de gefuseerde wervel zwakker is dan elk van de oorspronkelijke wervels. Fusie heeft niet veel invloed op de drift van de wervels, mogelijk wordt de radiële drift een beetje afgeremd. Ik laat zien dat fusie bespoedigd kan worden door een derde wervel die een deel van het impulsmoment meeneemt. Als 10 wervels losgelaten worden dan vinden we een gemiddelde radiële driftsnelheid die niet wezelijk anders is dan voor een enkele wervel wat impliceert dat wervelinteracties de accretie snelheid niet kunnen doen toenemen. De hoeveelheid accretie is ongeveer evenredig met het aantal wervels.

Bibliography

Abramowicz, M. A., Lanza, A., Spiegel, E. A., and Szuszkiewicz, E. "Vortices on accretion disks," *Nature* **356**, 41 (1992).

Adams, F. C. and Watkins, R. "Vortices in circumstellar disks," *Astrophys. J.* **451**, 314–327 (1995).

Aly, J. J. and Kuijpers, J. "Flaring interactions between accretion disk and neutron star magnetosphere," *Astron. Astrophys.* **227**, 473–482 (1990).

Arakawa, A. and Lamb, V. R. "A potential enstrophy and energy conserving scheme for the shallow water equations," *Mon. Wea. Rev.* **109**, 18–36 (1981).

Arnol'd, V. I. "On an apriori estimate in the theory of hydrodynamical stability," *Am. Math. Soc. Transl. Ser. 2* **79**, 267–269 (1969).

Babiano, A., Basdevant, C., Legras, B., and Sadourny, R. "Vorticity and passive-scalar dynamics in two-dimensional turbulence," *J. Fluid Mech.* **183**, 379–397 (1987).

Balbus, S. A. and Hawley, J. F. "A powerful local shear instability in weakly magnitized disks. I linear analysis," *Astrophys. J.* **376**(2), 214–222 (1991).

Balbus, S. A. and Hawley, J. F. "Instability, turbulence, and enhanced transport in accretion disks," *Rev. Mod. Phys.* **70**(1), 1–53 (1998).

Balbus, S. A., Hawley, J. F., and Stone, J. M. "Nonlinear stability, hydrodynamical turbulence, and transport in disks," *Astrophys. J.* **467**(1), 76–86 (1996).

Bennett, A. F. and Haidvogel, D. B. "Low-resolution numerical simulation of decaying two-dimensional turbulence," *J. Atmos. Sci.* **40**, 738–748 (1983).

Benzi, R., Paladin, G., Patarnello, S., Santangelo, P., and Vulpiani, A. "Intermittency and coherent structures in two-dimensional turbulence," *J. Phys. A: Math. Gen.* **19**, 3771–3784 (1986).

Benzi, R., Patarnello, S., and Santangelo, P. "On the statistical properties of two-dimensional decaying turbulence," *Europhys. Lett.* **3**(7), 811–818 (1987).

Binney, J. and Tremaine, S. *Galactic Dynamics*, Princeton series in astrophysics, Princeton U. P., Princeton, New Jersey (1987).

Bracco, A., Chavanis, P. H., Provenzale, A., and Spiegel, E. A. "Particle aggregation in a turbulent Keplerian flow," *Phys. Fluids* **11**(8), 2280–2287 (1999).

Bracco, A., Provenzale, A., Spiegel, E. A., and Yecko, P. "Spotted disks," in: *Proceedings of the Conference on Quasars and Accretion Disks.* (Ed. Abramowicz, A.) Cambridge Univ. Press (1998).

Brachet, M. E., Meneguzzi, M., Politano, H., and Sulem, P. L. "The dynamics of freely decaying two-dimensional turbulence," *J. Fluid Mech.* **194**, 333–349 (1988).

Brandenburg, A., Nordlund, Å., Stein, R. F., and Torkelsson, U. "Dynamo generated turbulence and large scale magnetic fields in a Keplerian shear flow," *Astrophys. J.* **446**, 741–754 (1995).

Burm, H. and Kuperus, M. "Accretion disk coronae and the contribution to angular-momentum transport in the disk," *Astron. Astrophys.* **192**, 165–169 (1988).

Carnevale, G. F., McWilliams, J. C., Pomeau, Y., Weiss, J. B., and Young, W. R. "Evolution of vortex statistics in two-dimensional turbulence," *Phys. Rev. Lett.* **66**(21), 2735–2737 (1991).

Chandler, C. J. and Richer, J. S. "Observations of circumstellar discs and jets," in: (Sellwood and Goodman, 1999) (1999).

Cho, J. Y.-K. and Polvani, L. M. "The emergence of jets and vortices in freely evolving, shallow-water turbulence on a sphere," *Phys. Fluids* **8**(6), 1531–1552 (1996a).

Cho, J. Y.-K. and Polvani, L. M. "The morphogenesis of bands and zonal winds in the atmospheres on the giant outer planets," *Science* **273**, 335–337 (1996b).

Cushman-Roisin, B., Chassignet, E. P., and Tang, B. "Westward motion of mesoscale eddies," *J. Phys. Ocean.* **20**, 758–768 (1990).

Cushman-Roisin, B. and Tang, B. "Geostrophic turbulence and emergence of eddies beyond the radius of deformation," *J. Phys. Ocean.* **20**, 97–113 (1990).

Dowling, T. E. "Dynamics of Jovian atmospheres," *Annu. Rev. Fluid Mech.* **27**, 293–334 (1995).

Dowling, T. E. and Ingersoll, A. P. "Jupiter's great red spot as a shallow water system," *J. Atmos. Sci.* **46**(21), 3256–3278 (1989).

Dritschel, D. G. "Vortex properties of two-dimensional turbulence," *Phys. Fluids, A* **5**(4), 984–997 (1993).

Dubrulle, B. and Valdettaro, L. "Consequences of rotation in energetics of accretion disks," *Astron. Astrophys.* **263**, 387–400 (1992).

Dubrulle, B. and Zahn, J.-P. "Nonlinear instability of viscous plane couette flow part 1. Analytic approach to a necessary condition," *J. Fluid Mech.* **231**, 561–573 (1991).

Ellzey, J. L., Henneke, M. R., Picone, J. M., and Oran, E. S. "The interaction of a shock with a vortex: Shock distortion and the production of acoustic waves," *Phys. Fluids* **7**(1), 172–184 (1995).

Farge, M. and Sadourny, R. "Wave-vortex dynamics in rotating shallow water," *J. Fluid Mech.* **206**, 433–462 (FS) (1989).

Frank, J., King, A., and Raine, D. *Accretion Power in Astrophysics*, Cambridge Astrophysics Series, vol. 21, second edn. Cambridge University Press, Cambridge, UK (1992).

Fridman, A. M. and Khoruzhii, O. V. "Vortices in astrophysical discs," in: (Sellwood and Goodman, 1999) (1999).

Geertsema, G. T. and Achterberg, A. "Turbulence in differentially rotating thin disks," *Astron. Astrophys.* **255**, 427 (1992).

Godon, P. "Numerical modeling of tidal effects in polytropic accretion disks," *Astrophys. J.* **480**, 329–343 (1997).

Godon, P. and Livio, M. "Vortices in protoplanetary disks," *Astrophys. J.* (Submitted; astro-ph/9901384) (1999).

Goldreich, P., Goodman, J., and Narayan, R. "The stability of accretion tori - I. long-wavelength modes of slender tori," *Mon. Not. R. Astron. Soc.* **221**, 339–364 (1986).

Harten, A. "High resolution schemes for hyperbolic conservation laws," *J. Comp. Phys.* **49**, 357–393 (1983).

Hawley, J. F. and Balbus, S. A. "A powerful local shear instability in weakly magnitized disks. II nonlinear evolution," *Astrophys. J.* **376**(2), 223–233 (1991).

Haynes, P. H. "On the instability of sheared disturbances," *J. Fluid Mech.* **175**, 463–478 (1987).

Horne, K. "Images of accretion discs. I-the eclipse mapping method," *Mon. Not. R. Astron. Soc.* **213**, 129–141 (1985).

Hoskins, B. J., McIntyre, M. E., and Robertson, A. W. "On the use and significance of isentropic potential vorticity maps," *Q. J. R. Meteorol. Soc.* **111**(470), 877–946 (1985).

Kida, S. "Motion of an elliptic vortex in a uniform shear flow," *Journal of the Physical Society of Japan* **50**(10), 3517–3520 (1981).

Kraichnan, R. H. and Montgomery, D. "Two-dimensional turbulence," *Rep. Prog. Phys.* **43**, 547–617 (1980).

Kuijpers, J. "Flares in accretion disks," in: *Proc. CESRA Workshop Caputh, Coronal Magnetic Energy Releases.* (Eds. Benz, A. O. and Krüger, A.) (Lecture Notes in Physics, vol. **444**) Springer Verlag, Berlin, pp. 135–158 (1995).

Larichev, V. D. and McWilliams, J. C. "Weakly decaying turbulence in an equivalent-barotropic fluid," *Phys. Fluids, A* **3**(5), 938–950 (1991).

Larson, R. B. "Non-linear acoustic waves in discs," *Mon. Not. R. Astron. Soc.* **243**, 588–592 (1990).

LeBeau, Jr., R. P. and Dowling, T. E. "EPIC simulations of time-dependent, three-dimensional vortices with application to Neptune's Great Dark Spot," *Icarus* **132**(2), 239–265 (1998).

Legras, B. and Dritschel, D. "Vortex stripping and the generation of high vorticity gradients in two-dimensional flows," *Applied Scientific Research* **51**, 445–455 (1993).

Lighthill, J. *Waves in Fluids*, Cambridge University Press, Cambridge (1978).

Lin, D. N. C. and Papaloizou, J. C. B. "Theory of accretion disks II: Application to observed systems," *Annu. Rev. Astron. Astrophys.* **34**, 703–747 (1996).

Lin, D. N. C., Papaloizou, J. C. B., and Savonije, G. J. "Wave propagation in gaseous accretion disks," *Astrophys. J.* **364**, 326–334 (1990).

Lovelace, R. V. E., Li, H., Colgate, S. A., and Nelson, A. F. "Rossby wave instability of Keplerian accretion disks," *Astrophys. J.* **513**, 805–810 (1999).

Marcus, P. S. "Numerical simulation of Jupiter's Great Red Spot," *Nature* **331**, 693–695 (1988).

Marcus, P. S. "Vortex dynamics in a shearing flow," *J. Fluid Mech.* **215**, 393–430 (1990).

Marcus, P. S. "Jupiter's Great Red Spot and other vortices," *Annu. Rev. Astron. Astrophys.* **31**, 523–573 (1993).

Marsh, T. R. and Horne, K. "Images of accretion discs. II-doppler tomography," *Mon. Not. R. Astron. Soc.* **235**, 269–286 (1988).

Martinsen, E. A. and Engedahl, H. "Implementation and testing of a lateral boundary scheme as an open boundary condition in a barotropic ocean model," *Coastal Eng.* **11**, 603–627 (1987).

Matthaeus, W. H., Stribling, W. T., Martinez, D., Oughton, S., and Montgomery, D. "Decaying, two-dimensional, Navier-Stokes turbulence at very long times," *Physica D* **51**, 531–538 (1991).

McWilliams, J. C. "The emergence of isolated coherent vortices in turbulent flow," *J. Fluid Mech.* **146**, 21–43 (1984).

McWilliams, J. C. "The vortices of two-dimensional turbulence," *J. Fluid Mech.* **219**, 361–385 (1990).

Meacham, S. P., Flierl, G. R., and Send, U. "Vortices in shear," *Dynam. Atmos. Oceans* **14**, 333–386 (1990).

Meleshko, V. V. and van Heijst, G. J. F. "On Chaplygin's investigations of two-dimensional vortex structures in an inviscid fluid," *J. Fluid Mech.* **272**, 157–182 (1994).

Miyoshi, M., Moran, J., Hernnstein, J., Greenhill, L., Nakai, N., Diamond, P., and Inoue, M. "Evidence for a black hole from high rotation velocities in a sub-parsec region of NGC 4258," *Nature* **373**, 127–129 (1995).

Möller, J. D. and Montgomery, M. T. "Vortex Rossby waves and hurricane intensification in a barotropic model," *J. Atmos. Sci.* **56**, 1674–1687 (1999).

Montgomery, M. T. and Kallenbach, R. J. "A theory for vortex Rossby-waves and its application to spiral bands and intensity changes in hurricanes," *Q. J. R. Meteorol. Soc.* **123**, 435–465 (1997).

Moore, D. W. and Saffman, P. G. "Structure of a line vortex in an imposed strain," in: *Aircraft Wake Turbulence and its Detection.* (Eds. Olsen, J., Gorlburg, A., and Rogers, M.) Plenum, New York, pp. 339–354 (1971).

Narayan, R., Goldreich, P., and Goodman, J. "Physics of modes in a differentially rotating system - analysis of the shearing sheet," *Mon. Not. R. Astron. Soc.* **228**, 1–41 (1987).

Naulin, V. and Spatschek, K. H. "Nonlinear drift-wave structures and their influence on particle transport," *Phys. Rev. E* **55**(5), 5883–5893 (1997).

Nauta, M. D. "Two-dimensional turbulence and accretion disks," *Geophys. Astrophys. Fluid Dyn.* (Submitted) (2000) (= Chapter 3).

Nauta, M. D., Kuijpers, J., and Zimmerman, J. T. F. "A single vortex in a two-dimensional polytropic accretion disk," *Astron. Astrophys.* (Submitted) (2000) (= Chapter 4).

Nauta, M. D. and Tóth, G. "A high Reynolds number algorithm for polytropic accretion disk studies," *Astron. Astrophys.* **336**, 791–801 (1998) (= Chapter 2).

Ong, R. S. and Roderick, N. "On the Kelvin-Helmholtz instability of the earth's magnetopause," *Planet. Space Sci.* **20**, 1–10 (1972).

Papaloizou, J. C. B. and Lin, D. N. C. "Theory of accretion disks I: Angular momentum transport processes," *Annu. Rev. Astron. Astrophys.* **33**, 505–540 (1995).

Pedlosky, J. *Geophysical Fluid Dynamics*, second edn. Springer-Verlag, Berlin (1987).

Pierrehumert, R. T. "Chaotic mixing of tracer and vorticity by modulated traveling rossby waves," *Geophys. Astrophys. Fluid Dyn.* **58**, 285–319 (1991).

Polvani, L. M., McWilliams, J. C., Spall, M. A., and Ford, R. "The coherent structures of shallow-water turbulence: Deformation-radius effects, cyclone/anticyclone asymmetry and gravity-wave generation," *Chaos* **4**(2), 177–186 (1994).

Polvani, L. M. and Wisdom, J. "Chaotic Lagrangian trajectories around an elliptical vortex patch embedded in a constant and uniform background shear flow," *Phys. Fluids, A* **2**(2), 123–126 (1990).

Polvani, L. M., Wisdom, J., DeJong, E., and Ingersoll, A. P. "Simple dynamical models of Neptune's Great Dark Spot," *Science* **249**, 1393–1398 (1990).

Press, W. H., Teukolsky, S. A., Vetterling, W. T., and Flannery, B. P. *Numerical Recipes*, Cambridge University Press (1992).

Pringle, J. E. "Accretion discs in astrophysics," *Annu. Rev. Astron. Astrophys.* **19**, 137–162 (1981).

Rayleigh, L. "On the stability, or instability, of certain fluid motions," *Proc. London Math. Soc.* **111**, 57–70 (1880).

Rhines, P. B. "Waves and turbulence on a beta plane," *J. Fluid Mech.* **69**, 417–443 (1975).

Różyczka, M. and Spruit, H. C. "Numerical simulations of shock-driven accretion," *Astrophys. J.* **417**, 677–686 (1993).

Rutten, R. G. M., van Paradijs, J., and Tinbergen, J. "Reconstruction of the accretion disk in six cataclysmic variable stars," *Astron. Astrophys.* **260**, 213–226 (1992).

Ryu, D. and Goodman, J. "Convective instability in differentially rotating disks," *Astrophys. J.* **388**, 438–450 (1992).

Santangelo, P., Benzi, R., and Legras, B. "The generation of vortices in high-resolution, two-dimensional decaying turbulence and the influence of initial conditions on the breaking of selfsimilarity," *Phys. Fluids, A* **1**(6), 1027–1034 (1989).

Savonije, G. J., Papaloizou, J. C. B., and Lin, D. N. C. "On tidally induced shocks in accretion discs in close binary systems," *Mon. Not. R. Astron. Soc.* **268**, 13–28 (1994).

Sawada, K., Matsuda, T., and Hachisu, I. "Spiral shocks on a Roche lobe overflow in a semi-detached binary system," *Mon. Not. R. Astron. Soc.* **219**, 75–88 (1986).

Sawada, K., Matsuda, T., Inoue, M., and Hachisu, I. "Is the standard accretion disk model invulnerable?," *Mon. Not. R. Astron. Soc.* **224**, 307–322 (1987).

Schramkowski, G. P. "Dynamics of slender flux tubes in accretion disks. II. shear and buoyancy of a single tube," *Astron. Astrophys.* **308**, 1013–1032 (1996).

Schramkowski, G. P. and Torkelsson, U. J. "Magnetohydrodynamic instabilities and turbulence in accretion disks," *Astron. Astrophys. Rev.* **7**, 55–96 (1996).

Sellwood, J. A. and Goodman, J. (Eds.) *Astrophysical Discs*. (Astronomical Society of the Pacific Conference Series, vol. **160**) (1999).

Shakura, N. I. and Sunyaev, R. A. "Black holes in binary systems. Observational appearance," *Astron. Astrophys.* **24**, 337–355 (1973).

Shapiro, L. J. and Montgomery, M. T. "A three-dimensional balance theory for rapidly rotating vortices," *J. Atmos. Sci.* **50**, 3322–3335 (1993).

Shapiro, L. J. and Ooyama, K. V. "Barotropic vortex evolution on a beta plane," *J. Atmos. Sci.* **47**(2), 170–187 (1990).

Smith, R. K. and Ulrich, W. "Vortex motion in relation to the absolute vorticity gradient of the vortex environment," *Q. J. R. Meteorol. Soc.* **119**, 207–215 (1993).

Spruit, H. C. "Stationary shocks in accretion disks," *Astron. Astrophys.* **184**, 173–184 (1987).

Srivastava, R. S. *Interaction of Shock Waves*, Fluid mechanics and its applications, vol. 22, Kluwer, Dordrecht (1994).

Steeghs, D., Harlaftis, E. T., and Horne, K. "Spiral structure in the accretion disc of the binary IP Pegasi," *Mon. Not. R. Astron. Soc.* **290**, L28–L32 (1997).

Stehle, R. and Spruit, H. C. "Hydrodynamics of accretion discs of variable thickness," *Mon. Not. R. Astron. Soc.* **304**(3), 674–686 (1999).

Stone, J. M. and Balbus, S. A. "Angular momentum transport in accretion disks via convection," *Astrophys. J.* **464**, 364– (1996).

Takano, K. and Wurtele, M. G. "A fourth order energy and potential enstrophy conserving difference scheme," Final Report `AFGL-TR-82-0205`, Dept. of Atmos. Sci., University of California, Los Angeles, UCLA, 405 Hilgrad Avenue, L.A. Califonia 90024 (1982).

Tanga, P., Babiano, A., Dubrulle, B., and Provenzale, A. "Forming planetesimals in vortices," *Icarus* **121**, 158–170 (1996).

Toh, S., Ohkitani, K., and Yamada, M. "Enstrophy and momentum fluxes in two-dimensional shear flow turbulence," *Physica D* **51**, 569–578 (1991).

Tóth, G. "Versatile advection code," in: *High-Performance Computing and Networking.* (Eds. Hertzberger, B. and Sloot, P.) (Lecture Notes in Computer Science, vol. **1225**) Springer Verlag, Berlin, p. 253 (1997).

Tóth, G. and Odstrčil, D. "Comparison of some flux corrected transport and total variation diminishing numerical schemes for hydrodynamic and magnetohydrodynamic problems," *J. Comp. Phys.* **128**, 82–100 (1996).

Trieling, R. R., Beckers, M., and van Heijst, G. J. F. "Dynamics of monopolar vortices in strain flow.," *J. Fluid Mech.* **345**, 165–201 (1997).

van Heijst, G. J. F. and Flór, J. B. "Dipole formation and collisions in a stratified fluid," *Nature* **340**(6230), 212–215 (1989).

Verbunt, F. "Observations of accretion discs in X-ray binaries," in: (Sellwood and Goodman, 1999) (1999).

von Weizsäcker, L. F. "Über die Entstehung des Planetensystems," *Zeitschrift für Astrophysik* **22**, 319–355 (1944).

Waugh, D. W. "The efficiency of symmetric vortex merger," *Phys. Fluids, A* **4**(8), 1745–1758 (1992).

Williams, G. P. "Planetary circulations: 1. barotropic representation of Jovian and terrestrial turbulence," *J. Atmos. Sci.* **35**, 1399–1426 (1978).

Williams, G. P. and Wilson, R. J. "The stability and genesis of rossby vortices," *J. Atmos. Sci.* **45**(2), 207–241 (1988).

Yecko, P. A. *Vortical Processes in Astrophysical Disks*, Ph.D. thesis, Columbia University (1995).

Zahn, J.-P. "On the nature of disk viscosity," in: *Structure and Emission Properties of Accretion Disks.* (Eds. Bertout, C., Collin-Souffrin, S., Lasota, J. P., and Tran Thanh Van, J.) Editions Frontières, Gif sur Yvette, pp. 87–97 (1990).

Zucrow, M. J. and Hoffman, J. B. *Gas Dynamics*, Ch. 7-4(e), vol. I, Wiley, New York (1976).

Dankwoord

Aan vele mensen ben ik dank verschuldigd om zeer uiteenlopende redenen. Soms was het slechts de honorering van mijn verzoek om eigen werk op te sturen, in andere gevallen leverden zij een substantiële bijdrage aan het uiteindelijke produkt. Hieronder wil ik een aantal personen in het bijzonder noemen.
Uiteraard komen mijn promotoren op de eerste plaats.
Jan Kuijpers educatieve inspanningen zijn eindelijk gehonoreerd met de uitverkiezing tot docent van het jaar. Het enthousiasme waarmee hij de zaak brengt werkt inspirerend, wat niet wil zeggen dat ik niet hartgrondig met hem van mening kan verschillen.
Sjef Zimmerman is meer naar mijn geaardheid. Wel was hij een bron van zorgen. Niet zozeer hemzelf maar meer zijn gezondheid. Toch was hij altijd beschikbaar voor commentaar, iets wat ik erg gewaardeerd heb. Gelukkig gaat het nu weer beter.
Probably the person that influenced me most is Gábor Tóth. Without his input I would have quit this research and this thesis would never have been written. His structured and visionary way of programming formed the reference for my own work although it took effort to keep me on the right track.
Ook mijn andere kamergenoten over de jaren, Nick Schutgens en Turlough Downes, komt lof toe, al was het maar voor de manier waarop ze het met me hebben uitgehouden.
Eduard Neven deelde niet alleen zijn fysische inzicht met me maar bood ook een blik op de "politieke spelletjes" die zich op ons vakgebied afspelen. Aan hem heb ik mijn voordracht op de EGS te danken.
Bram Achterberg en Max Kuperus, dank ik voor de discussies over een paar knelpunten die op het laatst optraden.
Als jaargenoot is Jeroen van Gent een extra gewaardeerde collega. Hoog tijd om weer eens terug te komen van ver met wat dia's, alhoewel dat nog wel een klein jaartje op zich zal laten wachten.
Kostas Tziotziou is a special case. Although he is included in the list of people who gave support on physical and technical problems, he was also keen on some complete nonsense which was a very welcome distraction from work.
Dan is er een groep mensen die ik lastig kon vallen met fysisch en technisch georiënteerde vragen. Allereerst natuurlijk Ed van der Zalm en Sake Hogeveen voor alles wat direct met computers te maken heeft en Marion Wijburg en Gé Geijtenbeek voor de administratieve kant. Op het gebied van IDL heeft Nick Hoekzema me het

een en ander bijgebracht. Ook Rob Rutten en Bert van den Oord waren, van tijd tot tijd, goed als vraagbaak. Wat verder weg waren Jan Rem, Egbert Westerhof en de vortex dynamica groep van Gert-Jan van Heijst. Als laatste vangnet op numeriek gebied en dus met de lastigste vragen kon ik altijd terecht bij Cees Vreugdenhil.
Finally I would like to thank two other Michaels, one in the UK (McIntyre) and the other in the US (Montgomery) for showing an interest in my work. We met rather accidentally but I think I profited a lot from these "incidents".
Afgezien van werk mocht ik ook de nodige steun ontvangen uit andere kring. Zelfs ik leeft niet op gedachten alleen. Voor de opname van smakelijke calorieën en al wat niet meer, ben ik vooral Heleen, Doede, Maartje en Johan erkentelijk. Ook Sandra en Ellen zorgde voor de nodige verstrooiing, bijvoorbeeld met hooi dat van het land moest. Meeste eer komt echter mijn ouders toe die me altijd vrij hebben gelaten welke keuze ik ook maakte en waar ik altijd een beroep op kon en kan doen.

Curriculum Vitae

Op 19 maart 1970 kwam ik ter wereld in Woudenberg. Mijn middelbare school, het Johan van Oldenbarneveld gymnasium te Amersfoort, rondde ik in 1988 af. Daarna begon ik aan de studie sterrenkunde aan de Universiteit Utrecht. Voor mijn afstudeerscriptie kwam ik bij Jan Kuijpers terecht en schreef ik "Een spheromak model voor bolbliksem". Tijdens het laatste jaar van mijn studie, met alle verplichte vakken voldaan, was er tijd voor wat extra's uit de natuur- en wiskunde en een stage van twee maanden in Noord-Ierland aan Armagh Observatory onder leiding van wijlen Brendan Byrne. Hier deed ik ervaring op met data reductie van sterspectra. Eind augustus 1993 behaalde ik het doctoraal theoretische sterrenkunde (c.l.) om twee dagen later als AIO aan mijn promotieonderzoek te beginnen op het gebied van wervels en accretieschijven bij Jan Kuijpers en Sjef Zimmerman. Het belangrijkste deel van dat werk ziet u terug in dit proefschrift.